Development and evaluation of aluminium-based thin films as potential alternatives to cadmium coatings

A dissertation submitted in partial fulfilment of the requirements for the degree of

Doctor of Philosophy

By

Sarah Banfield

Department of Materials Science and Engineering

The University of Sheffield, UK

February 2018

DECLARATION

I declare that the work presented in this thesis is my own, generated from my own original research. Where I have mentioned the work of others in support of my findings, this has been clearly stated with detailed references provided. To the best of my knowledge, this thesis (or any section of it) has never been submitted for any other degree or qualification at any other university or research institute.

ACKNOWLEDGEMENTS

I would like first of all to sincerely thank my supervisors, Dr. Adrian Leyland and Prof. Allan Matthews for their invaluable support and guidance throughout the duration of this work.

I would also like to express my gratitude to the Wallwork board for giving me the opportunity to do a PhD while remaining a Wallwork employee, for financial support by paying my tuition fees and for giving me the time I needed in the last few months to write up. My heartfelt thanks go to Dr. Jonathan Housden for his continuous support, constructive feedback and particularly for his kind words of encouragement which sustained me in difficult times. I am also grateful to all my colleagues in the technical department for their assistance with the use of various analytical equipments.

My gratitude also goes to all the industrial project partners, particularly Airbus UK and NMB-Minebea UK for supplying relevant test samples and providing guidance regarding the property requirements of a potential cadmium substitution coating. Innovate UK which partly funded this research work under the Technology Programme project number BA160E is greatly acknowledged.

Special thanks to Dr. Fahima Indeir for her assistance with the AC/DC/AC corrosion technique, her advice and guidance on understanding the EIS and pH data and for always being so helpful, encouraging and supportive. I would also like to thank Xiao Tao for his assistance with XRD analysis.

Lastly, I would like to thank my husband, Ellis, for his continued love and support throughout the duration of this work and my son, Arthur, for always bringing a smile to my face. Many thanks also to Plato and Darwin for providing much needed distraction and stress-relief!

ABSTRACT

Electroplated cadmium coatings have been extensively used for many years in the military, marine and aerospace industries to provide corrosion protection to steel substrates. Cadmium coatings act as a barrier layer, protecting the substrate from corrosion attack. They continue to offer protection even when damaged. Cadmium deposits also offer sacrificial protection by preferentially corroding and galvanic protection to coated components in contact with other metals such as aluminium. However the hazardous nature of cadmium which is harmful to both humans and the environment, is a major issue. Started over 30 years ago, research into finding more environmentally-friendly alternatives continues as no substitute coating has yet been developed which could replace cadmium over the full range of applications.

In this study, metallic AlCr(N) coatings containing 4 – 16 at% Cr and two different nitrogen contents (11-12 at% and 18 at%), were deposited by magnetron sputtering on stainless steel substrates - following initial coating deposition trials by both magnetron sputtering and electron-beam PVD. The coatings were then analysed to evaluate their mechanical, tribological and structural properties before being corrosion-tested using a novel AC/DC/AC cyclic test equipped with a pH monitoring system. The results indicate significant improvement in the mechanical (hardness range: 2 – 3.9 GPa) and tribological properties of the coatings with increasing alloying element content. In terms of corrosion performance, AlCr(N) with the lowest Cr content (i.e. 4 at%) displayed the best corrosion resistance properties owing to the formation of a thick and stable passive film within the pores as well as on the coating surface, providing excellent barrier corrosion protection. These promising results could be used to design graded Al-rich coatings in which individual layers are tailored to meet specific property requirements depending on the intended application, thereby enabling the replacement of cadmium on a range of steels and other engineering materials.

TABLE OF CONTENTS

LIST OF FIGURES

LIST OF TABLES

Chapter 1

Introduction and background

1.1 Introduction and aims

Cadmium coatings are used in a wide variety of applications, primarily to provide corrosion protection to steel substrates. The dense deposits produced typically by bath electroplating, possess excellent barrier and sacrificial corrosion properties and provide galvanic protection to coated parts in contact with aluminium [1]. These properties, amongst others, have led to the widespread use of cadmium coatings in many industries (e.g. military and aerospace). However the hazardous nature of cadmium, which is harmful to both humans and the environment, has driven research into developing safer alternatives. The majority of commercially used alternatives are zinc- and aluminium-based coatings produced by various types of deposition processes including electroplating, Ion Vapour Deposition (IVD), thermal spray or slurry. However none of the existing solutions possess all the desirable properties exhibited by cadmium and therefore can only be used in some applications but not others. There still remains a strong need to develop a suitable alternative to cadmium due to ever increasing legislative pressures. In recent years, research has focused mainly on the development of dense, corrosion-resistant aluminium-rich coatings using a variety of deposition processes including electroplating from ionic liquids, cold spray, CVD or PVD techniques. Work so far on PVD-deposited aluminium coatings is based largely on deposition techniques such as resistive evaporation (i.e. the commercially-available ivadising process which tends to produce porous deposits) and magnetron sputtering, which enables the

deposition of relatively dense (but often very thin) coatings. Also being investigated is the effect of alloying elements such as Cr, Ti, Mg, Mn and Mo on the corrosion properties of Al-based PVD coatings. The addition of such substitutional metallic elements in various proportions will affect the electrochemical potential of aluminium which can be adjusted to be close to that of the substrate material, enabling the coating to provide long-term and stable sacrificial protection to the underlying metal. In this study, metallic AlCr(N) coatings with varying (substitutional) chromium and (interstitial) nitrogen content were deposited on 15/5 PH and 17/4 PH steel substrates by magnetron sputtering.

A range of accelerated corrosion testing techniques are available for evaluating the corrosion performance of coatings. These include the widely used Salt Spray Test (SST) which was invented as the beginning of the 20th century [2] and Electrochemical Impedance Spectroscopy (EIS), a powerful tool for evaluating electrochemical corrosion mechanisms, which emerged and became popular in the 1970s, due to advances in computer programming and instrumented control [3, 4]. Although both techniques have been extensively used over the subsequent years, each presents some drawbacks. They are still quite time-consuming to implement and may not provide accurate information regarding the corrosion processes taking place, particularly in the case of the SST where the test environment is rarely representative of the actual working conditions [2]. In contrast the AC/DC/AC cyclic test which combines frequency-dependent AC impedance measurement (also called EIS) and DC cathodic polarisation, is an accelerated corrosion testing technique first used in the late 1990s to provide accurate evaluation of the corrosion performance of organic coatings within a relatively short time duration (i.e. less than 24 hours) [5]. The test is performed by alternating cycles of cathodic polarisation to induce damage and EIS measurements to assess the conditions of the coated system afterwards. The recent addition of a pH probe to the electrochemical cell [6] enables the solution pH to be monitored throughout testing,

providing useful information regarding the rate at which corrosion takes place for inorganic film/substrate systems. The use of such a modified AC/DC/AC test to assess the performance of electrically–conductive coating/substrate systems was only recently investigated by Indeir [6] who proved the validity of the technique for providing an accurate assessment of the corrosion behaviour of metal substrates and electrically-conductive metallic coatings.

The aim of this Thesis was to evaluate the corrosion performance of metallic aluminium-rich coatings using the improved AC/DC/AC corrosion testing technique. Testing of monolayer AlCr(N) coatings with varying alloying element content was carried out to assess their structural, mechanical, tribological and corrosion resistance properties with a view to building novel graded multilayer Al-rich coatings in which individual layers are tailored to meet specific property requirements, enabling the replacement of cadmium over a wide range of practical applications on steels and other engineering metals.

In order to meet the project aim, it was necessary to address the following objectives:

- Investigate the deposition of thick metallic Al-rich coatings using two different PVD techniques (Electron Beam PVD (EBPVD) and magnetron-sputtering) in order to determine which of the two would enable the coatings to be easily deposited on a production scale.
- Develop thick Al-rich coatings varying the Cr and N content and fully characterise them.
- Assess the effect of varying the Cr and N content on the corrosion and tribological performance of the coatings.
- Evaluate the ability of the AC/DC/AC cyclic corrosion test in discriminating between AlCr(N) coatings of different compositions

1.2 Thesis outline

This thesis is organised into six main chapters, described as follows:

- Chapter 1 provides some background information on cadmium coatings and explains the pressing need to find environmentally-friendly alternatives to cadmium.
- Chapter 2 gives an overview of the commercially available cadmium substitution coatings currently in use and the potential replacement coatings being developed.
- Chapter 3 describes in detail the main mechanisms of corrosion and reviews the range of accelerated corrosion testing techniques used to assess the corrosion performance of metals and coatings. It also introduces the recently modified and improved AC/DC/AC cyclic test used in this work to provide rapid and accurate evaluation of the corrosion properties of aluminium-rich deposits.
- Chapter 4 gives an in-depth description of the two PVD processes trialled in this work, as well as providing a review of the analytical and testing techniques used to evaluate the structural, mechanical, tribological and corrosion properties of the coatings.
- Chapter 5 reports on the results and discussion following the characterisation and corrosion testing of selected AlCr(N) coatings. Results of the structural, mechanical tribological and compositional analyses of the coatings are presented together with the data obtained from the AC/DC/AC corrosion test which include Open Circuit Potential (OCP) plots recorded during each relaxation period, EIS measurements taken after each DC/OCP cycle and graphs showing the evolution in solution pH with time.
- Chapter 6 summarises the main research findings and provides recommendations for future work.

1.3 Background

1.3.1 Cadmium and cadmium coatings

Cadmium was first discovered in Germany in 1817 as a by-product of the refining process of zinc. It is a soft metal with a bluish-white appearance. Cadmium possesses a wide variety of unique properties which led to its use in many industrial applications since the late 19th century. Cadmium-sulphide based pigments, for example have been used since 1850 in paintings and the first nickel-cadmium batteries were developed at the beginning of the 20th century. However, one of the early and most significant uses of cadmium was as a corrosion-resistant coating on steel components. Cadmium's popularity grew over the years due essentially to the fact that it exhibits a unique combination of desirable properties such as good corrosion-resistance, lubricity, electrical conductivity and solderability.

Cadmium coatings can be applied by mechanical plating, vacuum and ion deposition or electroplating – with electroplating accounting for over 90% of all cadmium coatings deposited [7].

1.3.2 The electroplating process

Electroplating is a chemical deposition process (typically performed in an aqueous bath environment) in which a coating is produced on an electrically-conducting surface by using an electrical potential to attract and reduce metallic ions, dissolved in the aqueous bath, at the surface of the material to be plated (Figure 1.1).

Two main components are involved in the plating process: the part to be plated (which generally forms the cathode of the circuit) and the anode – which is generally an electrode

made of the plating material. Both components are connected to a DC power supply and immersed in a solution containing salts of the metal to be deposited as well as various other ions that aid the flow of current. The metal salts dissociate in the aqueous electrolyte to form positively charged metal cations (M^+) and negatively charged anions (A^-). The DC current supplied to the anode causes it to oxidise, dissolving metal ions into the solution. The positively charged metal ions are attracted to the negatively biased cathode. As they reach the cathode, the metal ions are reduced into the neutral state of the plating material and deposited on the cathode surface [8].

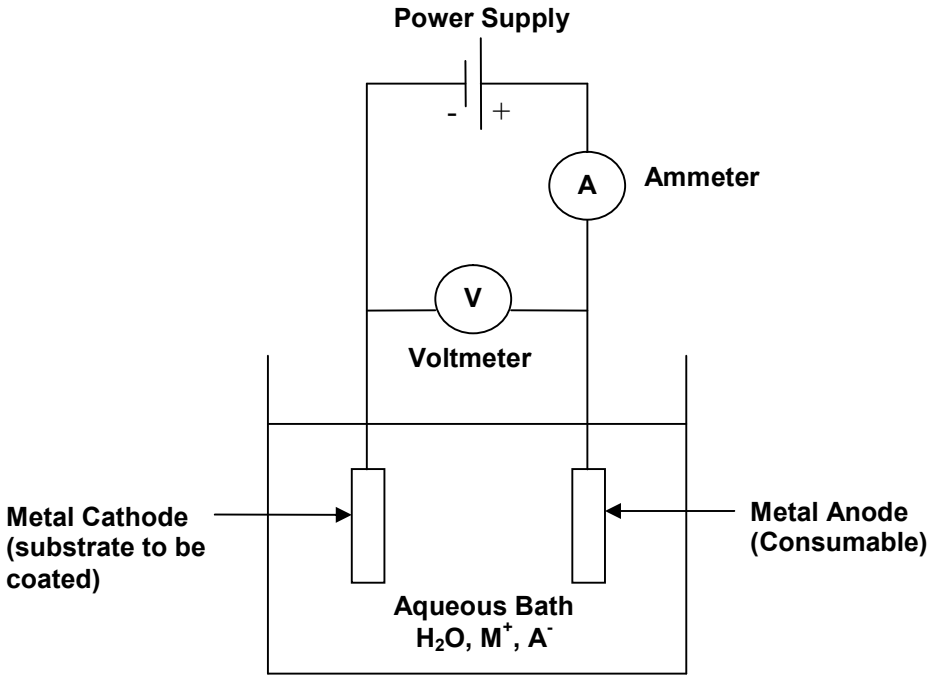

Figure 1.1: Schematic of the electroplating process

The electrodeposition of cadmium onto a metal substrate involves the reduction of Cd^{2+} ions at the electrolyte/substrate interface, followed by nucleation and growth to produce a coating.

The polycrystalline deposit formed consists of atoms arranged in a distorted hexagonal close-packed (hcp) structure [9-11]. Extensive research has been carried out over the years to deposit electroplated cadmium coatings with optimum properties. The use of various types of electrolyte for cadmium deposition has been widely investigated [10, 11]. Cadmium is conventionally plated in alkaline cyanide baths which, although highly toxic, are easy to control and produce a bright, uniform coating [12]. Other electrolytes such as acidic fluoroborate baths have also been used for cadmium plating; but, in recent years, more environmentally friendly alternatives such as sulphate and chloride baths have been developed [9, 10, 12].

Example of electrolytes used in cadmium plating:

- Alkaline cyanide baths are produced by dissolving cadmium oxide (CdO) in an aqueous solution of sodium cyanide (NaCN) [12]. The ratio of NaCN to Cd determines the operating characteristic of the bath. Alkaline cyanide baths can be used for rack plating of large components with complex shapes, as well as barrel plating large numbers of small parts. The ratio of NaCN to Cd used depends on the type of plating (rack or barrel) that will be carried out. Generally a low NaCN to Cd ratio is required for barrel plating whereas for rack plating where a high throwing power is needed the ratio is higher. Alkaline cyanide baths enable the deposition of fine-grained, bright cadmium coating.

- Acidic fluoroborate baths have mainly been employed in barrel plating processes but are unfortunately not suitable for rack plating due to their poor throwing power. Cadmium is highly soluble in fluoroboric acid compared to sodium cyanide which means that a higher dissolved cadmium content can be used in these baths. This in turn improves cathode efficiency and increases the rate of plating - as well as

lowering the chances of hydrogen embrittlement. However the use of acid fluoroborate baths has been limited not only because they are costly but also due to their toxicity (just as toxic as cyanide baths).

- Acidic sulphate baths are the most widely used plating solutions after cyanide baths. The bath is prepared by a process involving the dissolution of cadmium oxide in sulphuric acid. It can be used to deposit cadmium by both rack and barrel plating techniques and offers many advantages including good throwing power and adequate plating speed. However acidic sulphate baths generate heat during plating and must be continually cooled [12].

- Neutral chloride baths are prepared by mixing cadmium chloride with ammonium and potassium chloride. The pH of the solution is maintained between 7.0 and 7.8 using dilute hydrochloric acid or ammonium hydroxide as required. For electroplating using this type of electrolyte, mechanical agitation is required throughout the process to maintain the stability of the bath (which is critical) by thoroughly mixing the stabilising agent. In addition, sufficient amounts of stabilisers must be used in order to prevent the formation of insoluble cadmium hydroxide. Neutral chloride baths can be used for both rack and barrel plating as they possess excellent throwing power and produce a bright cadmium coating with exceptional corrosion resistance.

Various additives such as brighteners, grain refiners and stabilisers are added to the plating baths in order to improve the efficiency of deposition and the properties of the deposit formed [10, 12, 13]. Dolati et al [9] for example, reported that adding organic compounds such as Thiourea, 3-Picolin and Benzyl alcohol to an acidic sulphate mixture promotes the formation of brighter cadmium deposits exhibiting a finer grain structure.

Depending on the application, the typical thickness of cadmium coatings ranges between 5 and 25 μm [14, 15]. More often than not a chromate conversion coating is applied onto plated cadmium, to further improve its corrosion resistance.

1.3.3 Coating properties and applications

Cadmium possesses a wide range of unique properties which makes it suitable for use in many applications. It offers excellent corrosion resistance and provides sacrificial protection to steel substrates [16]. For sacrificial protection, the corrosion potential of the coating must be lower (i.e. more electronegative) than that of the substrate. Cadmium has a corrosion potential of -0.75V, which is lower than that of all steels (mild steel for example has a corrosion potential of -0.67V) [17]. Furthermore, the coating continues to provide protection from corrosion even when slightly damaged. Cadmium also protects coated components from galvanic corrosion when they come into contact with other materials such as aluminium [1]. In terms of mechanical properties, cadmium is soft, lubricious (with a measured coefficient of friction of 0.27 against a steel counterface) and ductile. As a soft metal with a measured hardness value ranging between 60 and 160 HV [10, 18], cadmium exhibits poor wear resistance. Its ductility, on the other hand, is an advantage as it allows pre-coated components to be mechanically formed (e.g. swaged) and assembled after coating. Other beneficial cadmium properties include good electrical conductivity and solderability.

This wide variety of properties makes electroplated cadmium an ideal candidate in many applications. It is used predominantly in the aerospace, marine and military sectors. In the aerospace industry, cadmium is applied onto steel landing gear components to provide protection against corrosion. Cadmium is also suitable for use on fasteners such as washers,

bolts and screws due to the low volume of corrosion products generated, reducing the risk of component seizure. Its high lubricity also provides good control of torque-tension for threaded fasteners [16]. In addition, cadmium coating can be applied onto sliding electrical connectors where low electrical resistance is required.

1.3.4 The need to replace cadmium

Although cadmium possesses many useful properties, its use as a coating material has become increasingly restricted over the years due to its high toxicity. Cadmium is a heavy metal toxin harmful to humans and the environment. In contaminated areas, this hazardous metal builds up in soils and sediments and once absorbed by plants will be carried along the food chain until it eventually arrives in the human body [19]. Whether ingested or inhaled, cadmium tends to accumulate in body tissues, mainly the kidneys, but also vital organs such as lungs and liver. High cadmium levels can cause severe health problems like bone demineralisation and kidney failure which can be fatal in some cases. Prolonged inhalation of cadmium can have a detrimental effect on lung function and increase the risk of lung cancer. In order to monitor and restrict the use of such dangerous chemicals, environmental legislations such as REACH ((Registration, Evaluation, Authorisation and restriction of CHemicals) have been set up. The main aim of REACH is to eliminate the use of hazardous chemicals and ensure that safe alternatives are utilised [20], unless compelling reasons to continue are given. Health and environmental issues, as well as increasing legislative pressure, therefore continue to drive research into finding safer alternatives to cadmium.

Chapter 2

Literature review

Findings from the literature can be divided into two main sections:

- Cadmium substitution coatings in commercial use
- Potential alternative coatings currently under development

2.1 Commercially available cadmium substitution coatings

The strong drive to replace electroplated cadmium has led to the emergence of a wide variety of safer and more environmentally-friendly alternatives. Listed below are commercially available cadmium substitution coatings used to date, complete with a brief description of each coating and the pros and cons associated with each process/coating.

- ***Electroplating of Zn-Ni and Sn-Zn alloys***

  Zn-Ni and Sn-Zn metal-alloy coatings have been used in the aerospace industry for many years as substitutes for electroplated cadmium in selected applications [16, 21]. The processing techniques are cleaner as no cyanide is used during plating. However the application of a chromate conversion coating is required afterwards to improve the corrosion properties of the alloy. Chromating often necessitates the use of a hexavalent chromium (Cr^{6+}) aqueous electrolyte, the use of which is also being

restricted due to its toxicity. Another drawback is the susceptibility of parts coated with these alloy deposits to fail by hydrogen embrittlement. To reduce this risk, a hydrogen embrittlement relief bake is generally required after coating - particularly in aircraft applications.

- ***Electrodeposition of pure aluminium***

  Due to the high electronegativity of aluminium (with a standard potential of -1.66 V which is above that for hydrolysis of water, at a potential of -1.23 V) electroplating of aluminium has to be carried out in a non-aqueous electrolyte and traditionally uses a mixture of organic aluminium salts in a toluene bath. The process usually takes place in a sealed environment, often in the presence of an inert gas, to prevent oxygen in the air from reacting with the electrolyte and altering some of its characteristics (i.e. reduction or loss of electrical conductivity) which in turn will have a detrimental effect on the properties of the coating produced [10]. The electrodeposition of aluminium is generally carried out over an electroplated nickel strike coat to improve coating adhesion [16, 21, 22]. Although the resultant aluminium coatings are dense and exhibit excellent corrosion properties, the process is expensive and difficult to control (e.g. the electrolyte is flammable and also potentially toxic if released into the environment).

- ***Ion Vapour Deposition of Aluminium (IVD-Al)***

  IVD-Al has been used for over 40 years as a replacement for cadmium plating. The process takes place under vacuum. Pure aluminium is evaporated and ionised in a low-pressure argon glow discharge. The ionised species are accelerated towards a negatively biased substrate holder where they condense to form the coating [23-26].

The aluminium coating produced is however columnar in structure and very porous (since the diode argon plasma employed is rather weak and low intensity). It therefore requires densification either by shot peening or bead blasting [16] which adds to the processing cost. Furthermore, chromating post-treatment of coatings is still a necessity (to moderate the corrosion behaviour of highly electronegative pure aluminium) in this otherwise clean process. Although the IVD technique completely eliminates the risk of failure by hydrogen embrittlement, its poor throwing power makes it inadequate for use on internal diameters with a length-to-diameter ratio greater than 1 [24]. A sputtering technique was recently developed to overcome this problem [27]. That process involves passing a high electrical current through a rod placed in the centre of the surface to be coated. The rod is negatively biased with respect to the substrate. As the current passes through the rod, a magnetic field is created which enhances the plasma and causes the rod to be uniformly sputtered and subsequently deposited on the inner diameter of the substrate. Aluminium coatings obtained by this sputter deposition process are less porous than IVD-Al and therefore do not require shot blasting after coating.

- ***Thermal spraying of Al and Al-alloys***

Al, Al-Zn and Al-Mg coatings have been deposited by thermal spray techniques (either flame or arc) on aircraft landing gear as an alternative to cadmium plating [16]. Thermal spraying techniques are simple, high deposition rate processes which are generally carried out in air, in inert gases and / or vacuum plasma environments. The coating produced is thick (80 -150 μm), but exhibits poor surface finish, as-deposited; consequently, on landing gear, the surface requires a post-coat polishing stage. This technique can only be used for a limited range of aerospace applications. Although

suitable for large size components, the process is not suited to small, complex-shaped items, such as connectors and fasteners.

- ***Slurry coatings***

Aluminium-based coatings deposited by slurry techniques have been successfully used in the aerospace industry as a replacement for cadmium plating. Slurry coatings are usually produced by first of all applying a slurry (an aqueous mixture containing fine particles) onto the parts to be coated either by immersion, spraying or brushing. The slurry is then cured at relatively high temperatures to form a hard deposit. For aluminium-based coatings, the slurry (which generally consists of aluminium powder particles dispersed in a mixture of phosphates and dichromates) is applied onto components and subsequently baked at temperatures in the range of 190 to 370^{o}C [16]. The deposit produced is then gently grit-blasted - usually with fine aluminium oxide particles or small glass beads, in order to expose the aluminium particles [21]. The coating possesses good electrical conductivity and provides excellent corrosion protection (both barrier and sacrificial) to the underlying metal substrate. The slurry process is very simple and particularly useful for applying a uniform coating on complex shapes. Proprietary SermeTel® coatings are a good commercial example of this type of aluminium based slurry coating, used widely on landing gear components and turbine engines. However one of the main drawbacks associated with this technique is the high curing temperature which makes it unsuitable for some high strength steels and for many aluminium alloys.

- ***Metal-filled polymer coatings***

  Metal-filled polymer coatings have for many years been successfully deposited onto fasteners for the automotive industry but have yet to be used widely on aerospace fasteners [16, 21]. The deposition process is simple and cost effective. A polymer filled with metal flakes of zinc or aluminium is deposited on steel substrates by spraying or dip-spinning. The components are then cured to produce the coating. A lubricious top coat is subsequently applied to provide adequate torque-tension. Metal-filled polymer coatings offer good corrosion resistance and appropriate lubricity. However the observed variability in coating thickness and resin viscosity constitute the main limitations of this technique.

Over the years, a wide range of cadmium plating alternatives have been developed and successfully implemented in the aerospace, automotive and military industries. However none of the commercially available alternatives to date meet all the requirements to replace cadmium plating over the full range of applications; they are partial solutions, that can be used in some applications but not others. In recent years, research in this field has centred on improving the properties of the existing cadmium substitution coatings as well as developing new alternatives.

2.2 Potential cadmium substitution coatings currently under development

Potential cadmium substitution coatings must fulfil many requirements, one of which is to provide sacrificial protection to steel substrates. For sacrificial protection, the chosen coating material must exhibit a more electronegative corrosion potential than the substrate in the application environment. One useful guide for the selection of protective coating materials

for outdoor environments is given in Figure 2.1 below, which shows the corrosion electropotentials in 3 wt% aqueous sodium chloride solution of a wide range of different materials.

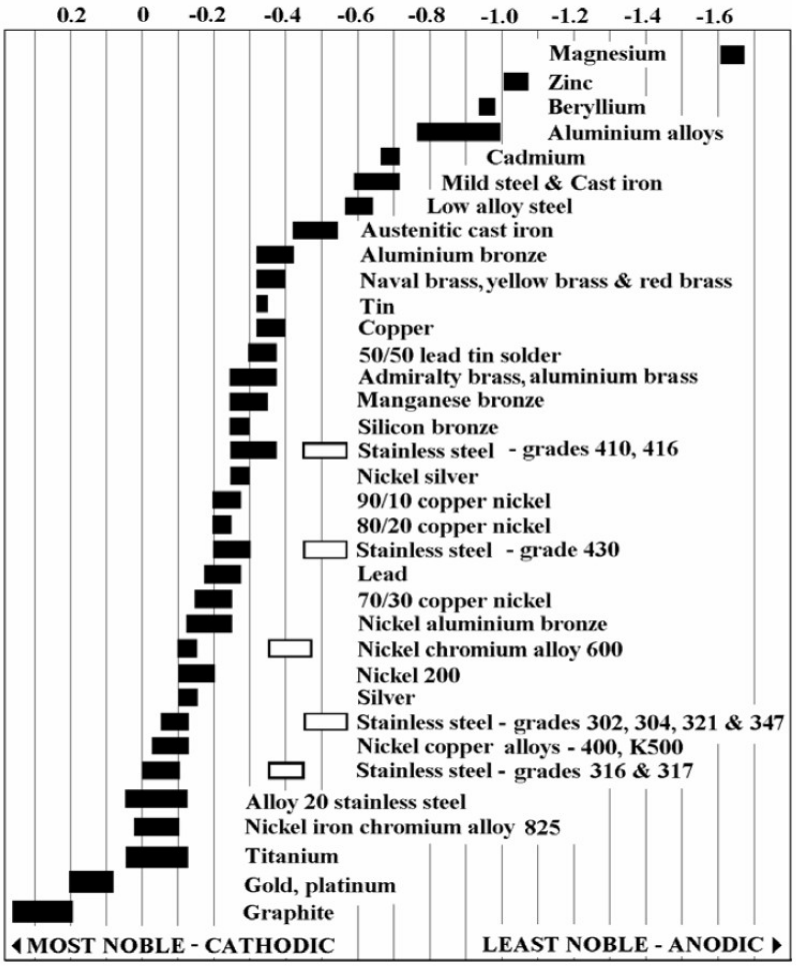

Figure 2.1: Corrosion electropotential scale in 3 wt% aqueous NaCl [28].

In 3 wt% aqueous NaCl environment, magnesium, zinc, beryllium and aluminium alloys appear to be the only metals and metal alloys able to offer galvanic protection to all types of steel substrates. Although very important, sacrificial properties are not the only criteria when looking for alternatives to cadmium. Other corrosion properties (such as barrier protection or

pitting resistance) as well as mechanical and tribological characteristics also need to be taken into account.

Extensive research is being carried out to try to develop alternative coatings to electroplated cadmium which possess some or all of the properties currently unique to cadmium, but without being toxic and hazardous to the environment. Many of the cadmium replacement alternatives being investigated are zinc- and/or aluminium-based coatings, deposited using a variety of processes.

2.2.1 Zn-Ni and Sn-Zn coatings

Although electroplated Zn-Ni and Sn-Zn alloy coatings have been in commercial use for many years, research is still taking place with a view to further improve the corrosion properties of those coatings and reduce the susceptibility of the coated substrates to hydrogen embrittlement. Previous studies investigating electroplated Zn-Ni deposits [29] have shown that the nickel content in those coatings should be kept between 8 and 15 wt% (~ 9-16 at%) so as to retain the sacrificial properties of the coating while providing adequate barrier protection. Although used commercially already, subsequent research has been directed towards altering the structure and composition of Zn-Ni alloys in order to further improve their corrosion properties. Pagotto Jr. [30] and Levesque [31], for example looked into developing more corrosion-resistant Zn-Ni coatings by modifying the electrodeposition process. Pagotto used a pulsed electrodeposition technique to apply pulsed cathodic currents (as opposed to conventional continuous currents) during Zn-Ni deposition while Levesque carried out the plating process under an applied magnetic field. In both cases, the coating structure consists of much finer grains than normally achieved with conventional Zn-Ni

coatings. Although no corrosion tests were carried out on deposits electroplated under the superimposed magnetic field, in the case of the pulsed process the results suggest that pulsed Zn-Ni deposits exhibit better sacrificial corrosion protection compared to conventional Zn-Ni of the same composition. Both methods still require further investigation to establish whether or not these modified electroplating processes can produce commercial deposits with improved corrosion properties. Recent work on electroplated Zn-Ni coatings has centred on studying the effect of process parameters such as current density on the structure and properties of the coatings produced. For example Maciej et al. [32] have reported that the higher the current density used during the plating process, the finer the microstructure. Sriraman [33] on the other hand, claims the opposite effect to be true. This could be due to the fact that different plating baths were used in each case, an acidic bath for the former and an alkaline bath for the latter. Another study also revealed that the effect of the current density on the nickel content of the coating is negligible when the plating process is carried out in an alkaline bath as oppose to an acid bath [34]. Although Zn-Ni deposited from an acid mixture was commonly used for many years, alkaline Zn-Ni is now favoured as the requirements for bath maintenance are much less challenging [35] and (as discussed later in this section) the propensity for hydrogen embrittlement can be reduced. On the subject of assessing which process parameters influence the coating structure, Mosavat et al. [34] have revealed that, at the nanometric scale, increasing the current density in an alkaline environment will increase the size of the colonies (clusters of grains) formed. This study, which also compared the properties and performance of microcrystalline versus nanocrystalline Zn-Ni coatings of similar composition, concluded that nanocrystalline Zn-Ni (average grain size: 13 – 55 nm) offers better corrosion protection by forming a much more stable oxide film. However these results were obtained from laboratory tests only and there

was no mention of whether or not post-deposition processes such as relief bakes or chromate treatments were still necessary.

In recent years, research has focused on the development of multilayer Zn-Ni coatings in which the coating properties can be optimised by varying the through-thickness nickel content. Popov et al [36] successfully deposited Compositionally Modulated Multilayer (CMM) Zn-Ni coatings on carbon steel substrates. The multilayer coating was produced by varying the cathodic potential to achieve a zinc rich coating near the substrate and a nickel rich coating at the surface. Zn-Ni deposits with nickel content ranging from 15 to 34 wt% (16 to 37 at%) were produced using this technique. The results of the study concluded that CMM Zn-Ni deposits with up to 20 wt% (22 at%) Ni exhibit better coating properties (i.e. adhesion, hardness and corrosion resistance) than conventional Zn-Ni coatings containing 8-15 wt% (~ 9-16 at%) Ni. However there was no mention of whether or not a conversion coating is required after plating of CMM Zn-Ni coatings. Bahrololoom [37] also investigated CMM coatings by using two separate plating baths to deposit alternate layers (up to 8) of Zn and Ni with a Zn layer as the top coat, to a total thickness of 9 μm. He reported that finer deposits are produced as the number of Zn/Ni layers is increased. Like Popov, Bahrololoom claims that CMM Zn/Ni coatings possess much improved corrosion properties in terms of barrier protection although in this case all the results were compared to single layer Zn. In both studies, the sacrificial properties of the CMM coatings were not investigated. More recently, work on CMM Zn-Ni coatings looked into comparing the performance of monolithic Zn-Ni deposits to that of multilayer Zn-Ni coatings consisting of 2, 4 and 50 alternate layers of Zn-12 wt% Ni (13 at% Ni) and Zn-14 wt% Ni (15 at% Ni) [32]. Despite the noticeably small difference in Ni content between each alternate Zn-Ni layer, the study claims that CMM Zn-Ni with 50 layers exhibited the best corrosion performance of all, showing no signs of red

rust after 672 hours of exposure to a salt bath which indicates that an increase in the number of layers in a multilayer system has a beneficial effect on the corrosion properties of the coating. Hedge et al [38] confirmed these findings by depositing and analysing CMM Zn-Ni coatings with 20, 60, 120, 300 & 600 alternate layers of Zn-Ni. They concluded that Zn-Ni with 600 layers exhibited the best corrosion performance compared to all the other CMM coatings and performed 50 times better than monolithic Zn-Ni. They also claimed (although no evidence was presented) that CMM Zn-Ni with 600 layers is the optimal configuration because, above 600 layers, the CMM coating behaves more like a monolithic coating.

Like Zn-Ni, Sn-Zn alloy coatings are also used commercially as a substitute for cadmium. The coatings, which usually contain 20 to 30 wt% Zn (31 to 44 at% Zn) have been shown to provide excellent corrosion protection to steels. However, variations in coating composition due to inconsistency in the bath chemistry have been reported as an issue [35]. In one study, the coating was found to contain less than 1 wt% Zn (1.8 at% Zn) instead of the targeted 20 wt% (31 at% Zn) [39] which will have a highly detrimental effect on its corrosion behaviour. Dubent et al. [40] recently claimed to have overcome this problem and can now offer a reproducible process. Their results also showed that the coating produced performs better than Zn-Ni and Cd in terms of providing corrosion protection to steel substrates in a salt spray environment.

Research looking into optimising the properties and performance of Zn-Ni and Sn-Zn alloy coatings by varying specific process parameters shows some encouraging results. However one outstanding problem is the need to apply a chromate conversion treatment after coating (which traditionally uses a toxic hexavalent chromium (Cr^{6+}) aqueous electrolyte), in order to further improve the corrosion resistance of those coatings. More recently, the less harmful trivalent chromium (Cr^{3+}) electrolyte is growing in popularity as the preferred choice for

chromate conversion coatings [11]. Another remaining issue which is associated with the electroplating process taking place in an aqueous environment is the increased risk of hydrogen embrittlement which can lead to the catastrophic failure of the coated components.

Hydrogen embrittlement

Hydrogen embrittlement (HE) has been a concern for many years as it can cause irreversible damage to the plated components in service. Throughout the electrodeposition process (but particularly in the initial stage) atomic hydrogen is formed at the surface of the steel substrate by the reaction of hydrated hydrogen ions with electrons. The reduction step is presented as follows:

$$H_3O^+ + e^- \rightarrow H_{ads} + H_2O \quad (2.1)$$

A large portion of adsorbed hydrogen subsequently reacts in one of two ways to form hydrogen molecules which then evolve to atmosphere. Hydrogen molecules are generated either by Tafel recombination or by electrochemical desorption as described below:

Tafel recombination: $2H_{ads} \rightarrow H_2$ (2.2)

Electrochemical desorption: $H_{ads} + H_3O^+ + e^- \rightarrow H_2 + H_2O$ (2.3)

However some adsorbed hydrogen atoms diffuse inside the metal substrate, where they generally accumulate in voids and at interfaces between non-metallic particles and the metal matrix [41]. This absorbed hydrogen can significantly alter the mechanical properties of the

substrate, resulting in a loss of ductility and mechanical strength which eventually leads to hydrogen embrittlement [42, 43]. To reduce the risk of hydrogen embrittlement, the coated components are traditionally baked at 200^{o}C for up to 24hrs [44] to disperse and/or remove the absorbed hydrogen.

Hydrogen adsorption during electroplating has been extensively investigated with many studies relying on a range of techniques to accurately measure the amount of hydrogen adsorbed by the substrate material. The most commonly used technique is the Devanathan-Stachurski double cell [45] which consists of two electrolytic cells containing a solution of NaOH and separated by a working electrode made of a thin membrane (around 1 mm thick) of the material to be investigated (generally a type of high strength steel). Hydrogen is generated by cathodic polarisation from one of the cells. The hydrogen atoms are then adsorbed at the metal surface and penetrate the membrane. As the hydrogen diffusing through the thin metallic membrane enters the second cell, it is oxidised and the oxidation current which is recorded is directly proportional to the amount of hydrogen diffusing through the substrate as shown in the equation below [46]:

$$J_{\infty} = \frac{DCo}{L} \tag{2.4}$$

Where J_{∞} is the oxidation current, D the hydrogen diffusion coefficient, Co the constant hydrogen concentration at the side of the membrane absorbing hydrogen and L is the membrane thickness.

Slow strain rate testing (SSRT) is often carried out in conjunction with the Devanathan-Stachurski hydrogen permeation technique in order to assess the extent of embrittlement. The test, which is performed in accordance with the ISO standard 7539-7:2005, involves elongating tensile specimens at a constant rate in a given environment [46]. For hydrogen embrittlement testing, the samples are usually made of a type of high strength steel, coated or uncoated, with the test generally taking place in air. In some cases, hydrogen charging of the test samples is carried out in an aqueous solution of NaOH prior to SSRT [47]. Failure by hydrogen embrittlement is initiated when a brittle crack is generated in the material as the applied stress and hydrogen concentration reach critical values. The crack then propagates inside the sample with failure occurring once the local stress exceeds the ultimate tensile strength (UTS) of the material [46]. A closer look of the fracture surface post-testing reveals the depth of the embrittled region, which is a good indicator of the extent to which hydrogen permeation has occurred inside the material.

Extensive research has been carried out in order to fully understand the processes that eventually lead to hydrogen embrittlement in high strength steels. The findings have revealed that the higher the strength of the steel, the greater its susceptibility to failure by hydrogen embrittlement [48]. It has also been suggested that factors such as grain size and secondary phases can affect the steel's propensity to HE by influencing the amount of hydrogen that eventually gets trapped inside the material [49].

Research looking at hydrogen uptake during coating deposition has revealed that a significant amount of atomic hydrogen is absorbed at the start of the electroplating process, indicated by the high hydrogen permeation current recorded [50, 51]. The permeation current decreases progressively with thickening of the coating which shows that, although the coating does not inhibit hydrogen absorption, it does provide some barrier effect. However, both Mirkova [50]

and Casanova [51] have measured permeation currents long after completing the electrodeposition process, which suggests that hydrogen permeation continues as the hydrogen trapped in the coating diffuses into the substrate, concluding that the zinc coating acts as a reservoir for hydrogen.

Recent studies have looked at ways of preventing hydrogen from diffusing into steel during the plating process; improving the barrier properties of the electrodeposited coating appears to show promising results. Fors example, Paatsch [52] claims that electroplating a thin Ni layer (1 – 2 μm) before Zn or Zn-Ni electrodeposition significantly reduces the amount of hydrogen absorbed by the substrate as the Ni layer acts as a barrier to hydrogen diffusion. This is because the diffusion coefficient of hydrogen through nickel is very low, around 8 x 10^{-10} cm^2s^{-1} at 25°C, compared to the value recorded for steel (2 x 10^{-7} cm^2s^{-1}) [53]. His GDOES results confirmed that the amount of hydrogen detected in both coating and substrate was negligible when a thin Ni interlayer was applied before either Zn or Zn-Ni deposition. Subsequent research carried out by Robinson and Gigandet [42, 43] also corroborates those findings, further highlighting the importance of the Ni layer at the substrate/Zn-Ni interface. Their studies also revealed that in the early stage of Zn-Ni electrodeposition, a thin Ni-rich layer forms at the substrate surface which is advantageous in preventing hydrogen from diffusing into the substrate, instead becoming trapped in the Ni-rich layer. However, components still require baking after conventional Zn-Ni electrodeposition, which suggests that the very thin Ni layer (probably less than 1 μm thick in this case) does not completely prevent hydrogen absorption by the substrate.

Recently, a Low Hydrogen Embrittlement (LHE) alkaline Zn 13–17 wt% (~ 14-19 at%) Ni treatment was commercially developed [54]. The plating bath is free of additives (mainly brighteners), giving LHE Zn-Ni coatings a dull appearance. It is claimed that LHE Zn-Ni is

dense enough to satisfy the corrosion requirements yet porous enough to enable hydrogen to easily escape during the relief bake. According to Gaydos [55], LHE Zn-Ni coatings passed the hydrogen embrittlement and re-embrittlement tests and provided adequate corrosion performance. However Ross et al [56] recently reported that LHE Zn-Ni failed their hydrogen embrittlement tests. LHE alkaline Zn-Ni clearly requires further optimisation to prove its effectiveness at lowering the risk of hydrogen embrittlement when compared to conventional Zn-Ni coatings.

Other research in this field has looked at adding a third element to Zn-Ni in order to reduce or prevent hydrogen permeation into the substrate. Popov et al [57] reported that adding a small amount of cadmium to Zn-Ni not only improves the corrosion properties of the coating (as the Ni content can be raised without losing the coating's sacrificial properties) but also significantly reduces hydrogen absorption and permeation into the substrate. However as the industry is trying to eliminate cadmium use, this coating will probably never be considered as a suitable substitute to cadmium plating. Later work by Popov et al investigated the addition of safer elements such as copper [58] and phosphorus [57, 59] to Zn-Ni with the aim to reduce hydrogen entry into the substrate. Initial results look promising but further investigation is necessary to get a better understanding of the performance of those coatings.

Although electroplated Zn-Ni coatings have been commercially used for many years as replacements for cadmium, extensive research is still taking place with the aim to further improve their corrosion properties as well as reducing the steel substrates' susceptibility to hydrogen embrittlement.

Hydrogen re-embrittlement

Hydrogen adsorption can also occur in service when the sacrificial coating applied to offer protection against corrosion, begins to corrode, causing sections of the steel substrate to become exposed, hence providing a cathodic site for the reduction process to take place and generate atomic hydrogen at the surface of the steel [46, 60]. If enough hydrogen becomes adsorbed by the steel substrate hydrogen re-embrittlement (HRE) could take place, leading to the catastrophic failure of coated components. According to Robinson et al [46], the more active the coating, the higher the concentration of hydrogen generated at the steel surface. This is partly why chromating is widely used in order to slow down the dissolution of sacrificial coatings, hence preventing large quantities of hydrogen from evolving. The structure of the coating also plays an important role in determining the extent to which hydrogen generation and adsorption will occur as a dense coating will provide better barrier protection of the steel substrate (by delaying or preventing the arrival of corrosive media at the substrate surface) compared to a porous one. As with hydrogen embrittlement, slow strain rate tests can also be used to assess the susceptibility of coated components to HRE. In this case however, in order to try and replicate the in-service environment in which HRE is likely to occur, a section of the tensile specimen is scribed to remove the coating, exposing the bare steel. The whole specimen is subsequently immersed in 3.5 wt% NaCl before and during the test. After testing, the fracture surfaces are observed in detail to determine the extent of HRE.

As mentioned above, one of the factors that significantly increase the steel substrate's susceptibility to hydrogen embrittlement is the type of process used to deposit the coating. Electroplating in an aqueous media is known to significantly increase that risk, whereas the use of other deposition techniques such as PVD processes reduce it. In the case of hydrogen

re-embrittlement however, the properties of the deposited coating, namely its electrochemical potential and barrier corrosion characteristics, influence the likelihood of HRE occurring and the extent to which it would occur [42].

2.2.2 Aluminium-based coatings

The bulk of the research into finding a successful alternative coating to cadmium has mainly centred on investigating aluminium-based coatings. This involved not only adding different elements (i.e. Mg, Mo, Mn), in various proportions to Al and studying their effect on the properties of the coatings produced but also experimenting with a wide range of deposition techniques in order to produce those coatings.

Electrodeposition of Al and Al alloys

Unlike Zn alloy plating, the electrodeposition of Al and Al alloy coatings is a non-aqueous process which must take place in a sealed environment as the characteristics of the electrolyte can be altered if exposed to air which in turn will have a detrimental effect on the properties of the coating produced. In the case of Al-Mn coatings for example, two different electrolytes can be used during the deposition process: a toluene bath containing Al and Mn chlorides [61] or a molten salt bath also rich in Al and Mn chlorides [62]. The toluene bath operates at temperatures as low as 60^{o}C to produce Al-rich deposits containing 20 – 35 wt% (14-21 at%) Mn. The low processing temperature is advantageous for coating high strength steels and aluminium substrates, although the hazardous nature of the bath (volatility and flammability of the toluene solvent and high reactivity of Al chlorides in contact with water) is an issue. The electrodeposition of Al-Mn by molten salt bath is the preferred option. The bath temperature in this case operates between 157 to 190^{o}C [62, 63] which, although too high for

use on structural aluminium components, is low enough for plating most steels used in aerospace applications [15, 20]. Using this technique, Jankowski [63] deposited Al-Mn alloy coatings containing 14 and 25 wt% (7 and 14 at%) manganese. Corrosion tests (i.e. B117 5% salt spray and SO_2 salt spray) carried out on those coatings revealed that Al-14 wt% (7 at%) Mn provides sacrificial protection to the steel substrates while Al-25 wt% (14 at%) Mn offers better barrier protection. In the same study, Jankowski also investigated the susceptibility of Al-Mn alloy coatings to hydrogen embrittlement. The test results indicate that failure by hydrogen embrittlement could occur in Al-Mn plated deposits but the risk of failure by this mechanism can be greatly reduced by baking the plated components for 24 hours at 191^{o}C [63]. As there is no hydrogen in the plating bath, embrittlement is only likely to occur if the chloride salts are not completely removed from the components as they could react with water vapour in the air to form corrosive HCl which can subsequently lead to hydrogen embrittlement. Recent attempts to scale up molten salt bath electrodeposition of Al-Mn to a production process failed as hydrogen and aluminium chloride fumes generated during electroplating, had a detrimental effect on the bath chemistry leading to inconsistent bath composition as well as causing excessive crust formation in the plating tank and ventilation equipment [62]. Further work is required in order to develop a plating bath suitable for the electrodeposition of Al-Mn coatings, which reduces or preferably eliminates fuming. Moreover, like all other electroplated alternatives, Al-Mn coatings also require chromating after plating, which remains a legislative issue as the process often requires the use of toxic Cr^{6+} in solution.

Also under development is the electrodeposition of aluminium and aluminium alloys from ionic liquids. Ionic liquids are salts with an unusual chemical structure which enables them to remain in the liquid state at low temperatures. The electrodeposition process usually takes

places at temperatures in the range of 60 to 100^{o}C and, unlike conventional electroplating of Al, the environment does not need to be so tightly sealed as the chemistry of the bath mixture remains unaffected at low levels of moisture (up to 0.1 wt.% of water) [64]. Ionic liquids possess many desirable properties such as low vapour pressures, low viscosity, high electrical conductivity and the ability to remain liquid over a wide range of temperatures. These properties have enabled the electroplating of metals such as aluminium which cannot be otherwise plated from simple aqueous solutions. Work by Caporali et al [65] looked into the corrosion behaviour of such aluminium coatings. Results so far indicate that the coating provides sacrificial and barrier protection to the steel substrates and that coating failure is likely to occur due to pitting corrosion. Further research is being carried out in an attempt to gain a better understanding of ionic liquids and how they influence the characteristics of the coatings produced. Different types of ionic liquids [66, 67] are presently being investigated in order to understand their effect on the properties of the coatings produced. Moreover, process parameters such as the current density used during electroplating are also being considered. For example, Bakkar et al. [66], having deposited nanocrystalline Al by electroplating from ionic liquids, reported that the higher the current density the finer the microstructure of the coating and the better its corrosion resistance properties. Recently, Al alloys such as Al-Cu have been deposited by this process. Suneesh et al. [67] who compared the corrosion behaviour of Al and Al - 8at% Cu concluded that the alloy exhibited much better corrosion resistance properties. Looking at the available literature, it is clear that very thick coatings can be deposited from ionic liquids [67, 68]. Indeed, it has been reported that deposition rates as high as 1 μm per minute can be achieved [64] which will make this a desirable process for implementation at the production scale. While electroplating from ionic liquids presents many benefits, further work is required in order to gain an in-depth understanding of the key mechanisms taking place during the deposition process so as to produce better coatings and

overcome any issues that may arise, associated with up scaling the process into production [35, 68]. One remaining drawback is the need for a chromate treatment after coating to further enhance the corrosion properties [68].

Al-based slurry coatings

Al-based slurry coatings have been used for many years as a replacement to cadmium, particularly in the aerospace industry on large components such as landing gear and also on materials which can withstand the relatively high curing temperatures involved [35]. The deposits produced are dense and uniform, even on complex shapes. Moreover, unlike cadmium, no chromate conversion treatment is required, post-deposition. However, one of the main drawbacks associated with this technique is the high curing temperature which makes it unsuitable for some high strength steels and many aluminium alloys. In a recent report, Agüero et al [69] claimed to have successfully developed a slurry process with a moderate curing temperature (though the specific temperature used was not stated) which enabled the deposition of an Al-based coating on a high strength low alloy steel (i.e. AISI 4340). The coating is said to possess excellent corrosion resistance properties, offering barrier and sacrificial protection to the substrate in salt fog corrosion tests as well as providing galvanic protection when placed in contact with Al alloy 2024-T3. These findings were confirmed by another study [70] which carried out electrochemical tests on an Al-based slurry coating. Although in this case the galvanic coupling was against bare steel, the coating still showed good galvanic compatibility. If the curing temperature can be reduced without compromising performance, it will enable coating deposition over a wider range of substrates and allow Al-based slurry coatings to be considered as replacement to cadmium over the full range of applications.

Cold spraying of aluminium and aluminium alloys

In recent years, the interest in cold spray technology has risen due to the advantages that the process offers over conventional thermal spray techniques. Cold spray is a solid-state process used to deposit dense and well-adhered coatings by accelerating small powder particles (1-50 μm) in a supersonic jet of compressed gas against a substrate [71, 72]. Unlike thermal spraying, the gas temperature in this case is lower than the melting point of the material to be deposited. Consequently, all the detrimental effects of a high temperature process (i.e. oxidation, evaporation, residual stresses) are greatly reduced or completely eliminated. The coating formed is fully dense with relatively low oxygen content. However, despite all its advantages, cold spray is still a line-of-sight technique and therefore applying a uniform coating onto complex shapes is an issue. Moreover the process is limited to large size components and polishing is required after coating due to the poor surface finish. Aluminium coatings deposited by cold spray are currently being considered as replacement to cadmium plating as well as for local repair of IVD Al-coated components such as landing gear [71].

CVD of aluminium

Pure aluminium deposited by Atmospheric Pressure CVD (APCVD) is also being investigated as a potential alternative to cadmium plating. Organometallic precursors, such as tri-isobutyl-aluminium (TIBAL) or tri-ethyl-aluminium (TEA) are often used to deposit aluminium coatings over a range of temperatures. Berman et al [73] claimed that APCVD Al can be deposited at temperatures as low as 230^{o}C although test results presented so far are those of aluminium coatings produced at 275 – 300^{o}C. A recent study also reported that APCVD Al coatings were deposited at temperatures in the range of 273^{o}C to 316^{o}C [74].

The technique offers many advantages such as high deposition rate (around 0.5 - 1 μm per min) and excellent throwing power [74], which enables good coating uniformity even on

complex shapes. However the relatively high process temperature is a major limitation as it could restrict the use of this process on temperature-sensitive materials such as high-strength steels and aluminium alloys. The Al deposits produced by APCVD are dense, smooth and exhibit good coating-substrate adhesion [75]. In terms of corrosion properties, Berman et al [69] reported that APCVD Al coatings offer sacrificial protection to steel substrates and perform as well as type I, class I cadmium plating in neutral salt fog tests. However the aluminium deposits produced require a relief bake after coating to reduce the risk of hydrogen embrittlement. Suh et al [74] confirmed that a post deposition bake-out at 190^{o}C for 23 hours is required in order to remove the absorbed hydrogen. Furthermore, the application of a chromate conversion coating is necessary to improve the corrosion properties of APCVD Al. In this work [73], chromating was carried out using Cr^{3+} instead of the more hazardous Cr^{6+}.

Aluminium coatings deposited by Metal-Organic CVD (MOCVD Al) are also being considered as potential candidates for replacing cadmium. In this process, the precursors which are liquid at room temperature are evaporated and subsequently introduced to the substrates in the gas phase. MOCVD Al coatings are widely used to coat semiconductors although more tests are required to assess their suitability for aerospace applications [76]. Preliminary results indicate that the MOCVD process offers excellent conformal coverage producing a uniform coating on complex parts. Other advantages include the ability to coat internal diameters with negligible risk of failure by hydrogen embrittlement [16]. Although the initial corrosion test results look promising, the usage of MOCVD Al coatings in the aerospace industry might be limited by the process temperature. The temperature must be high enough to break down the metal-organic molecules during coating deposition and low enough for MOCVD Al to be suitable for application on high-strength steels and aluminium alloys. Coating trials are being carried out at temperatures ranging from 260^{o}C to 320^{o}C [16].

Potential alternatives deposited by PVD processing

Research into finding new PVD-based alternatives to cadmium plating has mainly centred on the deposition of fully dense aluminium alloy coatings with better tribological and corrosion properties than IVD Al. Although very little has been done on the deposition of other metals such as zinc alloys by PVD, Bowden et al [77] investigated Zn-Ni alloy coatings deposited by closed-field unbalanced magnetron sputtering. The study concluded that PVD Zn-(10 - 15 at%)Ni deposits possess better barrier corrosion resistance than their electroplated counterpart. However, unlike electroplated Zn-Ni coatings, they offer very little sacrificial protection to the steel substrate as their corrosion potential is close to that of steel (Ecorr = -615mV for PVD Zn-(12 at%)Ni and Ecorr = -603mV for steel). Graded PVD Zn-Ni with up to 12 at% Ni (which was also investigated in this work) behaved similarly to pure zinc, exhibiting poor corrosion behaviour in neutral salt fog tests. The results of this work therefore indicate that electroplated Zn-Ni (despite its remaining drawbacks) is still a better cadmium alternative coating than PVD Zn-Ni.

As mentioned above, the limitations of IVD aluminium have encouraged extensive research to be carried out in this field in order to improve the properties of aluminium deposits. This was done by adding various alloying elements to aluminium as well as experimenting with different deposition processes to achieve the desired properties. PVD processes such as Ion Beam Assisted Deposition (IBAD) and magnetron sputtering were used to deposit fully dense aluminium alloy coatings. For example Enders et al [78] investigated in great detail the corrosion behaviour of Al-Mg coatings deposited by Ion Beam Assisted Deposition (IBAD). Results of potentiodynamic current-potential measurements indicated that the higher the magnesium content, the greater is the shift of the depassivation potential towards more negative values. They concluded that unlike pure aluminium deposits, Al-Mg coatings offer

better protection of the steel substrate against uniform and pitting corrosion. No outdoor exposure tests were performed in this study. In addition, the electrochemical results obtained from testing the alloy coatings could not be directly compared to those measured on cadmium-coated components, possibly because the thickness of Al-Mg coatings was between 0.25 and 4 μm (i.e. very thin, compared to 10-14 μm for electroplated cadmium samples). This research is obviously still in its early stages and further work is needed to optimise various IBAD process parameters (i.e. ion-to-atom arrival ratio, angle of ion incidence) as well as determining the correct Al-Mg composition to achieve optimum coating properties.

Al-Mg alloy coatings were also deposited by magnetron sputtering [79]. Looking at the stoichiometry of the coatings produced by this technique, Shedden et al [80] reported that below 35 at% Mg, the Al-rich coating has an fcc structure with a low solubility limit for argon. Above 35 at% Mg however, the coating adopts an hcp structure with a higher affinity for trapping Ar. The study concluded that an increase in substrate negative bias voltage (above -50V) will increase the number of Ar ions trapped in the hcp structure, resulting in amorphisation of the coating. Bates et al [81], who also deposited Al-Mg alloy coatings using this PVD technique, were more interested in the corrosion behaviour of the coating. Their neutral salt fog test results indicated that the time to red rust (i.e. when corrosion of the steel substrate starts to occur) increases with an increase in Mg content showing a peak in corrosion performance at 20 wt% Mg (22 at% Mg). These preliminary results on the deposition of Al-Mg coatings by PVD look promising; however, further work is required in analysing the coatings' tribological properties and corrosion behaviour (by carrying out outdoor exposure tests in various environments), in order to thoroughly assess their suitability as a replacement for cadmium.

Another aluminium-based coating that has been considered is Al-Mo alloy deposited by closed field unbalanced magnetron sputtering [82]. The coating structure and properties were investigated over a wide range of compositions. From SEM analysis of coated samples, it is clear that Al-rich coatings containing 30 wt% Mo (11 at% Mo) exhibit a dense, fine-grained structure. However as the molybdenum content is increased, the coating becomes more columnar in structure. In terms of friction properties, Abu-Zeid [82] and Bielawski [17] have both shown that the coefficient of friction, measured against a steel counterface, decreases with increasing molybdenum content, with the lowest coefficient of friction (~ 0.19) achieved at Al-95 wt% (84 at%) Mo. Electrochemical corrosion tests indicate that alloying aluminium with molybdenum improves the barrier corrosion properties of the coating. However, Al-Mo coatings can only offer sacrificial protection below 14 wt% (4 at%) Mo. Based on this information, Bielawski deposited a 12μm thick multilayer Al-Mo coating composed of 3 layers: a pure Al layer close to the substrate, a middle layer of Al-14 wt% (4 at%) Mo and a top layer of Al-95 wt% (84 at%) Mo. Initial test results showed good coating/substrate adhesion but further analysis investigating the corrosion properties of the multilayer coating is required.

In a more recent study, Creus et al. [83] evaluated a range of binary Al-based systems in terms of their mechanical and corrosion properties. Their results showed that, in the majority of cases, increasing the alloy content improves the coating's mechanical properties and its resistance to pitting corrosion. However, the same increase also causes a shift in the corrosion potential towards more positive values which eventually leads to a loss of sacrificial protection. The study suggested that multilayer coatings, in which one layer provides adequate mechanical and barrier corrosion properties and the other the required sacrificial protection, might be a way to overcome this issue. Follow-on work by the same team [84]

indeed confirmed the benefits of this type of multilayer system. It was also reported that, as well as taking into account the nature of the alloying element, the number of interfaces was an important parameter to consider when building a multilayer coating, as it was revealed that increasing the number of interfaces increases the corrosion resistance. The two main PVD techniques used for the deposition of these coatings were electron beam (EB) PVD and magnetron sputtering. While EBPVD is a more versatile, high deposition rate process, magnetron sputtering tends to produce denser coatings. Studies comparing coatings deposited by the two techniques revealed that the resulting difference in coating morphology translates into slightly different corrosion behaviour. For example, it was reported that due to their structural differences Cr deposited by EBPVD had an open circuit potential (OCP) slightly more electronegative than Cr produced by magnetron sputtering [83]. A smaller corrosion current density was also recorded for EBPVD-deposited Cr. As expected, these differences in coating morphology also influence coating mechanical and structural properties [85, 86]. For example, Perez et al. [85] showed that Al – 25 at% Ti deposited by magnetron sputtering is harder than its EBPVD counterpart (7 GPa compared to 4 GPa).

In recent years, research interest has shifted towards the deposition of amorphous coatings which exhibit low porosity and excellent wear and corrosion resistance properties. Coating amorphisation occurs when one or more alloying elements are added to a host lattice, resulting in destabilisation of the lattice crystalline structure when the local atomic strains generated during the alloying process reach a critical point [87]. Work by researchers such as Inoue [88] (on bulk amorphous alloys) and Leyland et al. [89, 90] (on amorphous PVD coatings) has shown that mixing elements of different atomic size and preferred crystallographic structure favours the formation of amorphous coatings with improved mechanical and electrochemical properties. Metallic amorphous coatings have previously

been investigated for their mechanical, tribological and corrosion properties. They have been of interest for many years as it is believed that they provide better corrosion resistance properties due to their chemical homogeneity and absence of structural defects [83]. Recent work by Creus et al. [86] supports this theory as it showed that adding a small amount of manganese (Mn) to Al improves the corrosion resistance of the coating but this is further enhanced as the Mn content is increased and the coating structure undergoes a phase change from crystalline to amorphous. As well as improved electrochemical properties, amorphous coatings also exhibit better mechanical properties. Sanchette et al [91-93] for example, evaluated the coating characteristics of amorphous aluminium-based alloys deposited by magnetron sputtering and electron beam plasma-assisted PVD. They reported that a single phase amorphous sputtered Al-Cr coating can be produced by alloying Al with 18-22 at% Cr [92] resulting in a dense, hard and corrosion resistant deposit. Sanchette also found that adding nitrogen to the binary mixture significantly improves its corrosion properties by increasing the breakdown potential (giving better resistance to pitting corrosion) as well as decreasing the open circuit potential (providing cathodic protection of the steel substrate). However later work by Creus et al [94, 95] showed that incorporating nitrogen in Al-Cr reduces the Al content and causes the potential to shift towards more positive values - resulting in reduced sacrificial protection of steel substrates. Amorphous Al-Ti(N) alloy coatings were also investigated [92]. Amorphisation in this case occurs at 35-45 at% Ti with the coating exhibiting high hardness combined with excellent corrosion resistance properties. A similar study [85] also revealed that, depending on the PVD technique used, coating amorphisation occurs at different alloying element contents. While for magnetron sputtered AlTi, amorphisation takes place in the range of 25 to 60 at% Ti, for EBPVD-deposited AlTi, this range is narrowed down to between 24 and 32 at% Ti.

The work presented in this Thesis investigates the deposition of Al-based coatings both by magnetron and electron-beam PVD techniques. Alloying elements such as Cr and N were added in various proportions to Al and their effect on the properties and performance of the Al-rich coatings produced were evaluated. Gaining an in-depth understanding of the characteristics of each monolithic coating was essential in order to build graded multilayer Al-based coatings which can successfully replace cadmium over the full spectrum of applications.

Chapter 3

Fundamentals of corrosion and corrosion testing techniques

Corrosion is defined as the degradation of metals by chemical interaction with their environment. It can also be described as the process which enables metals to return to their more stable, original state. Metals are thermodynamically stable in their naturally-occurring state (as metal compounds in ores) but the refining process to extract them requires a large amount of energy. Most metals therefore have a tendency to want to lose that stored energy through corrosion and revert to metal compounds similar to their original state.

Though a natural phenomenon, corrosion can cause minor or severe damage to metallic components in service, resulting in some instances in their catastrophic failure.

3.1 The corrosion process

Corrosion is an electrochemical process consisting of oxidation and reduction reactions occurring simultaneously in different places at the metal/electrolyte interface. In order to maintain balance of charges between electrodes, the total rate of oxidation must always equal that of reduction.

Four components are necessary for corrosion to take place: an anode, a cathode, a conduction path between the two electrodes and an electrolyte (which must also be electrically

conductive) [96, 97]. As shown in Figure 3.1, electrons are generated at anodic sites during oxidation and migrate through the metal towards cathodic sites where they are consumed during reduction reactions. Metal loss always occurs at the anode(s), with the positively-charged metal ions released moving through the electrolyte (shown below as positive current) in the opposite direction to the electrons' flow.

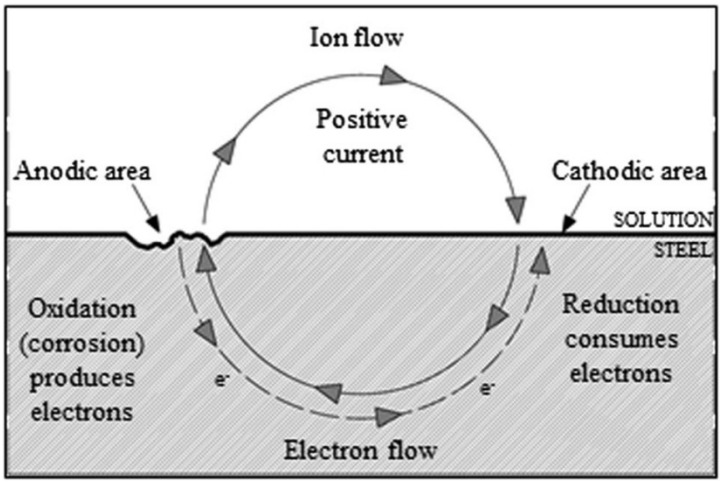

Figure 3.1: Schematic of the corrosion of steel in a saline solution [97]

Below, the corrosion process of a commonly used metal such as iron in an acidic solution, will be described as an example. At the anode, the oxidation reaction causes iron dissolution and electron generation as described in the following half cell reaction:

$$Fe \rightarrow Fe^{2+} + 2e^{-} \tag{3.1}$$

The two electrons generated are subsequently consumed at the cathode as shown by the cathodic reduction reaction:

$$2H^{+} + 2e^{-} \rightarrow H_2 \tag{3.2}$$

Therefore the overall reaction is:

$$Fe + 2H^+ \rightarrow Fe^{2+} + H_2 \quad (3.3)$$

Other cathodic reactions can occur, depending on the acidity or alkalinity of the environment. For example in a weak acid, the following oxygen reduction reaction is favoured:

$$O_2 + 4H^+ + 4e^- \rightarrow 2H_2O \quad (3.4)$$

However if iron is immersed in a neutral or alkaline solution, then oxygen will be reduced in the subsequent cathodic reaction to form hydroxide ions:

$$O_2 + 2H_2O + 4e^- \rightarrow 4OH^- \quad (3.5)$$

3.1.1 Electrode potential

The electron transfer process occurring during corrosion generates a potential difference between the electrode(s) and the solution. Although this potential cannot be directly quantified, it can be measured relative to a standard electrode of known potential. A range of reference electrodes are available for measuring the potential. These include amongst others the Standard Hydrogen Electrode (SHE), the Saturated Calomel Electrode (SCE), the copper/copper sulfate electrode and the silver/silver chloride electrode. The SHE, which potential is arbitrarily fixed at 0V under standard conditions, has historically been used to

determine the electrode potential of various half cell reactions. The electrode potential of selected metals measured against the SHE is provided in the table below.

Table 3.1: Standard electrode potentials of selected metals [96]

Reduction reaction	E^0 (V vs. SHE)	
$Au^{3+} + 3e^- \longrightarrow Au$	+1.498	Noble
$Ag^+ + e^- \longrightarrow Ag$	+0.800	↑
$Cu^{2+} + 2e^- \longrightarrow Cu$	+0.342	
$2H^+ + 2e^- \longrightarrow H_2$	0.000	
$Sn^{2+} + 2e^- \longrightarrow Sn$	-0.138	
$Mo^{3+} + 3e^- \longrightarrow Mo$	-0.2	
$Ni^{2+} + 2e^- \longrightarrow Ni$	-0.257	
$Cd^{2+} + 2e^- \longrightarrow Cd$	-0.403	
$Fe^{2+} + 2e^- \longrightarrow Fe$	-0.447	
$Cr^{3+} + 3e^- \longrightarrow Cr$	-0.744	
$Zn^{2+} + 2e^- \longrightarrow Zn$	-0.762	
$Mn^{2+} + 2e^- \longrightarrow Mn$	-1.185	
$Ti^{3+} + 3e^- \longrightarrow Ti$	-1.37	
$Al^{3+} + 3e^- \longrightarrow Al$	-1.662	↓
$Mg^{2+} + 2e^- \longrightarrow Mg$	-2.372	Active

3.1.2 Thermodynamics of corrosion

The tendency of a metal to corrode can be assessed thermodynamically by calculating the change in Gibbs free energy (ΔG) which gives an indication of whether or not a corrosion

reaction is likely to occur spontaneously. According to Faraday's law, ΔG is directly related to the electrode potential E, as given by the following equation:

$$\Delta G = -nFE \tag{3.6}$$

Where n is the number of electrons transferred during the corrosion reaction and F is Faraday's constant (96,485 C/mol).

ΔG must be negative for a reaction to proceed spontaneously. This also implies that the electrode potential E must always be positive for a spontaneous corrosion reaction to occur.

The electrode potential (also called the total cell potential) is the potential difference between the two half cell reactions taking place during the corrosion process. E can thus be written as follows:

$$E = E_c - E_a \tag{3.7}$$

Where E_c is the cathodic potential and E_a the anodic potential.

Therefore for corrosion to occur spontaneously, $E_c - E_a > 0$ so $E_c > E_a$ [98].

When all the reactants and products are in their standard states then Faraday's law can be written as follows:

$$\Delta G^\circ = -nFE^\circ \tag{3.8}$$

Where ΔG^0 is the free energy change under standard conditions (i.e. 1 mol/l for ions in solution, 1atm pressure for pure gases) and E^0 is the standard electrode potential (Table 3.1).

Under non-standard conditions (which is generally the case for most corrosion reactions), the Nernst equation, which takes into account other factors such as the concentration of ions, can be used to calculate the electrode potential:

$$E = E° - \left(\frac{RT}{nF}\right) lnQ \tag{3.9}$$

Where R is the universal gas constant (8.314 J/Kmol), T is the absolute temperature (in degrees Kelvin) and Q is the reaction quotient (ratio of product M^{n+} to reactant M).

This equation can be simplified by substituting numerical values for the constants (R & F), assuming that T = 298°K (25°C) and converting natural logarithms ln to base 10 giving:

$$E = E° - \left(\frac{0.059}{n}\right) log_{10} Q \tag{3.10}$$

It is clear from this simplified equation that the electrode potential is closely related to the metal ion concentration in the electrolyte.

3.1.3 E-pH (Pourbaix) diagrams

Thermodynamic laws demonstrate that corrosion of a metal immersed in an aqueous solution is driven by two main parameters: the electrode potential and the acidity or alkalinity of the solution (also called solution pH) [99]. Potential-pH diagrams (or Pourbaix diagrams) are constructed from thermodynamic data under equilibrium conditions and used to represent the

stability of a metal and its oxidised species at a given potential and pH. Three zones of stability are usually identified on a graph: corrosion (the metal is actively corroding), immunity (no corrosion is taking place) and passivation (corrosion is prevented by the formation of an oxide film on the metal surface) [98]. Pourbaix diagrams therefore provide a map describing the behaviour of a pure metal in an aqueous environment as a function of its potential and the solution pH. They are widely used in many sectors, from corrosion research to geochemistry, water treatment and hydrometallurgy [100].

Figure 3.2 below shows the E-pH diagram of iron immersed in water. E is the standard electrode potential measured against the SHE.

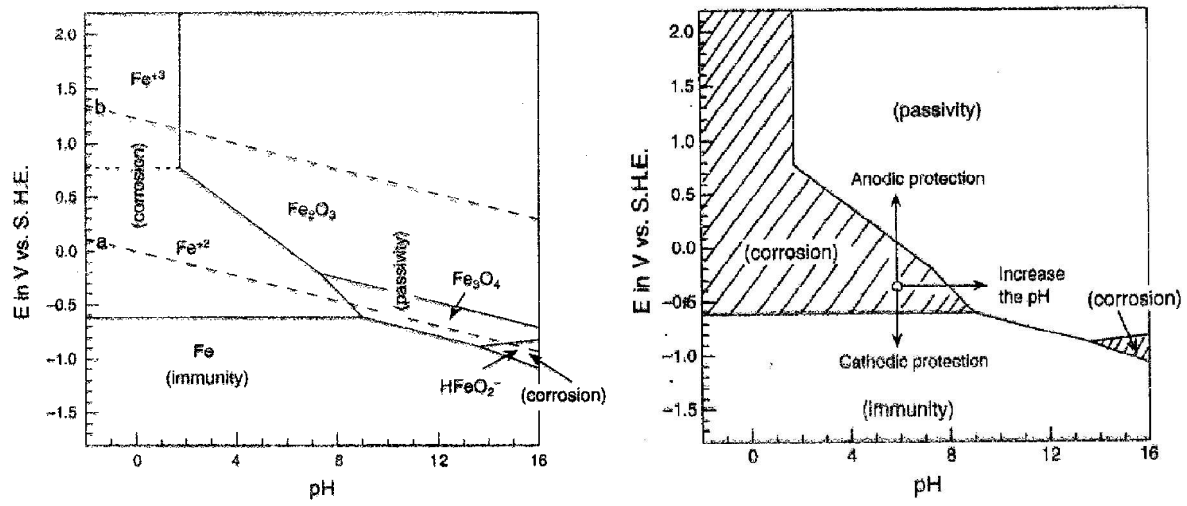

a) b)

Figure 3.2: a) E-pH diagram for iron in water at 25°C showing which elements are stable in the different zones of stability. b) A simplified version of a) highlighting the corrosion zones [96]

From the graph it is clear that iron is thermodynamically stable (i.e. zone of immunity) when its electrode potential tends towards more negative values and this is true over a wide range

of pH. The zones of corrosion highlighted indicate that iron undergoes corrosion in both acidic and alkaline environments, with Fe^{2+} and Fe^{3+} forming at lower pH values and $HFeO_2^-$ at higher pH values. In the passivity regions, oxide films such as Fe_2O_3 and Fe_3O_4 are more stable, protecting the metallic iron underneath from further corrosion.

The dotted lines a and b represent the hydrogen and oxygen lines respectively. Below a, hydrogen is produced from the reduction of either hydrogen ions in acidic solutions or water in alkaline solutions. Above b, oxygen is liberated through the dissociation of water [96]. Oxygen is therefore stable above b, while hydrogen is stable below a. Water is thermodynamically stable between the two lines.

While Pourbaix (E-pH) diagrams provide useful information regarding the stability of a metal and its corrosive species in an aqueous environment, they present some limitations due to their inability to give any indication of the rate of corrosion. This will be discussed in the next section.

3.1.4 Corrosion kinetics

3.1.4.1 Electrochemical polarisation

While thermodynamic laws predict whether or not a corrosion reaction will proceed, the kinetics tell us the rate at which such reaction is likely to occur. During an electrochemical reaction, the flow of current between electrodes causes the potential of each electrode to shift from its equilibrium value. This deviation from equilibrium is called polarisation. A potential shift in the positive direction away from the equilibrium potential is referred to as anodic polarisation while a shift in the negative direction is called cathodic polarisation. The scale of the deviation is known as the overpotential or overvoltage η, given by:

$$\eta = E - E_0 \tag{3.11}$$

Where E is the electrode potential resulting from the flow of current and E_0 is the electrode potential when the net current flow is zero (also called the equilibrium potential, the open-circuit potential or the corrosion potential E_{corr}) [96].

There are three main types of polarisation, defined as activation, concentration and ohmic. An electrochemical reaction takes place through a series of consecutive steps with the slowest step controlling the rate of the reaction. This rate determining step can lead to activation polarisation by limiting the number of electron transfer reactions taking place. Taking as an example the hydrogen evolution reaction which commonly occurs at the surface of metals immersed in an acid, the reaction can be described in two steps:

1. Reduction of hydrogen ions: $2H^+ + 2e^- \rightarrow 2H_{ads}$ (3.12)

2. Combination of hydrogen atoms to form molecules: $2H_{ads} \rightarrow H_2$ (3.13)

If the reduction reaction proceeds at a much slower rate than the rate at which electrons are generated on the metal surface then this would lead to a build up of negative charge, resulting in activation polarisation. The electrode potential in this case would be electronegative with respect to the equilibrium potential (cathodic polarisation). If on the other hand, the hydrogen ions in solution are slow to reach the metal surface (i.e. drop in concentration of the reactant, H^+) and enable the reduction step to take place, then this would again lead to a build-up of electrons on the electrode surface, resulting in this case in concentration polarisation [96].

Ohmic (or resistance) polarisation occurs when the resistivity of the electrolyte is high enough to hinder the current flow between the anode and the cathode, causing a potential drop (IR) across the solution and hence a difference in potential between the two electrodes. The effect of ohmic polarisation is only noticeable when the electrodes are some considerable distance apart [101].

3.1.4.2 Corrosion rate measurement from corrosion current

There are many available techniques for determining the corrosion rate of a material. These include amongst others the weight loss method, the chemical analysis of solution, thickness measurements and electrochemical techniques [96]. Electrochemical methods are very popular as they offer a quick and accurate way of calculating the corrosion rate.

During corrosion, the flow of current between the anode and cathode can be used to provide a measure of the corrosion rate. According to Faraday's law, the mass loss m, is directly related to the corrosion current I, as given by the equation:

$$m = \frac{Ita}{nF} \tag{3.14}$$

Where t is the time, a the atomic weight, n the number of electrons involved in the reaction and F is Faraday's constant.

The corrosion rate r can be derived from the above equation as follows:

$$r = \frac{m}{At} = \frac{ia}{nF} \tag{3.15}$$

Where A is the surface area and i is the corrosion current density (also known as i_{corr}).

Unlike E_{corr}, i_{corr} cannot be directly measured at equilibrium. Instead, it can be obtained by forcing the potential either in the anodic or cathodic direction relative to E_{corr} (potentiodynamic experiments) and extrapolating the linear sections of the resulting Tafel plot as shown in the figure below:

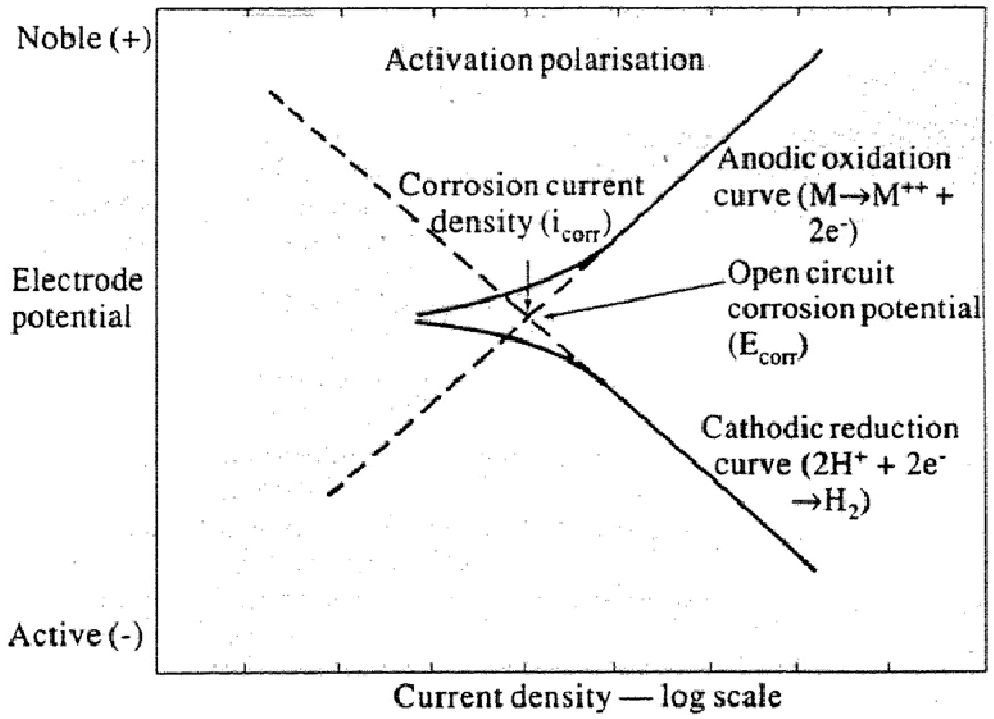

Figure 3.3: Example of a Tafel plot [102]

3.1.5 Corrosion mechanisms of aluminium

3.1.5.1 Uniform corrosion

Aluminium is extensively used in applications where corrosion is an issue due to its ability to form a stable oxide film in air, providing corrosion protection particularly in neutral solutions [103]. As reported in chapter 2, many cadmium alternative coatings currently in use or being developed are aluminium-based. Moreover, the coatings investigated in this project are also aluminium-rich so it was essential to take a look at the corrosion mechanism of aluminium. Corrosion of aluminium in aqueous solutions involves partial oxidation and reduction reactions taking place simultaneously on its surface, resulting in the dissolution of the native oxide layer. The type of reaction occurring is strongly dependent on the nature of the environment [104]. According to Moon et al [105], direct metal dissolution characterised by the generation and ejection of aluminium ions occurs more readily in acidic solutions, whereas in alkaline media metal dissolution takes place indirectly via the successive formation and dissolution of the oxide film. In acidic solutions, the corrosion process therefore proceeds as follows:

At the cathode, hydrogen is produced via the following reduction reaction:

$$H^+ + e^- \rightarrow \frac{1}{2} H_2 \tag{3.16}$$

At the anode Al oxidises, releasing Al^{3+} in solution:

$$Al \rightarrow Al^{3+} + 3e^- \tag{3.17}$$

Therefore the overall reaction can be summarised as follows:

$$Al + 3H^+ \rightarrow Al^{3+} + \frac{3}{2}H_2 \quad (3.18)$$

In alkaline solutions, two partial cathodic reactions are possible, resulting in the formation of hydroxide ions either from the reduction of oxygen:

$$\frac{3}{4}O_2 + \frac{3}{2}H_2O + 3e^- \rightarrow 3OH^- \quad (3.19)$$

and / or from the reduction of water:

$$3H_2O + 3e^- \rightarrow \frac{3}{2}H_2 + 3OH^- \quad (3.20)$$

However it has been confirmed that, of the two reactions, water reduction is the main cathodic reaction occurring during corrosion of aluminium in an alkaline environment [105].

As mentioned above, direct metal dissolution at anodic sites is not possible in alkaline solutions mainly due to the fact that aluminium ions are not thermodynamically stable in this high pH environment [106]. Instead, film formation and dissolution occurs consecutively throughout the process. Film formation results from the migration of hydroxide ions through the oxide film at anodic sites, causing aluminium hydroxide to form electrochemically via the following equation:

$$Al + 3OH^- \rightarrow Al(OH)_3 + 3e^- \quad (3.21)$$

Subsequent chemical dissolution of the aluminium hydroxide film takes place as a result of hydroxide ions attack at the film / electrolyte interface, causing the formation of aluminate ions:

$$Al(OH)_3 + OH^- \rightarrow Al(OH)_4^- \quad (3.22)$$

The partial reaction at the anode which combines (3.21) and (3.22) can therefore be presented as follows:

$$Al + 4OH^- \rightarrow Al(OH)_4^- + 3e^- \quad (3.23)$$

The overall corrosion reaction in alkaline solutions can be summarised in the following equation:

Combining (3.20) and (3.23): $Al + 3H_2O + OH^- \rightarrow Al(OH)_4^- + \frac{3}{2}H_2$ (3.24)

Therefore corrosion of aluminium in alkaline solutions leads to metal dissolution (generating aluminate ions) and hydrogen evolution.

Hebert et al. [107] have demonstrated in a recent study that Al metal dissolution in an alkaline environment can also occur via the formation aluminium hydride (AlH_3) from the reaction of aluminium with cathodically generated hydrogen, as shown in the following equation:

$$Al + 3H \rightarrow AlH_3 \quad (3.25)$$

Aluminium hydrides subsequently react with hydroxide ions at the anode, resulting in metal dissolution as follows:

$$AlH_3 + 7OH^- \rightarrow Al(OH)_4^- + 3H_2O + 6e^- \quad (3.26)$$

Al metal dissolution in alkaline media therefore occurs indirectly via the formation of either aluminium hydroxides or aluminium hydrides which are subsequently attacked by hydroxide ions at the film/electrolyte interface to generate aluminate ions.

If the Al metal surface is covered by a thick protective oxide layer (Al_2O_3) then, in the presence of an alkaline solution, dissolution of the oxide film would occur according to the following equation:

$$Al_2O_3 + 2OH^- + 3H_2O \rightarrow 2Al(OH)_4^- \quad (3.27)$$

Oxide film dissolution however takes place at a much slower rate than that of metallic Al [103].

3.1.5.2 Pitting corrosion

Pitting corrosion is a localised form of corrosion attack which occurs as a result of the breakdown of a protective passive film. It is a dangerous form of corrosion for three main reasons [96]:

1) With the pits confined to small fixed areas, catastrophic failure caused by localised perforation and damage of the component can rapidly occur while the rest of the part remains intact.

2) Under an applied stress, pits can act as initiation sites for stress corrosion cracking.

3) The pits may be difficult to detect if they become filled with corrosion products.

Aluminium is prone to pitting corrosion, which generally occurs in the presence of chloride ions (Cl^-) and results in the local breakdown of the passive film. Pits are usually initiated at sites where defects and non-metallic inclusions are present or where the protective film has been mechanically damaged. Although the mechanisms underlying the initiation of pitting corrosion are not fully understood, it is generally accepted that pitting takes place in three stages [96, 108]: Cl^- ions adsorption at the oxide film surface is followed by Cl^- ions penetration into the film and finally localised film dissolution, which is initiated at the metal/oxide interface (Figure 3.4).

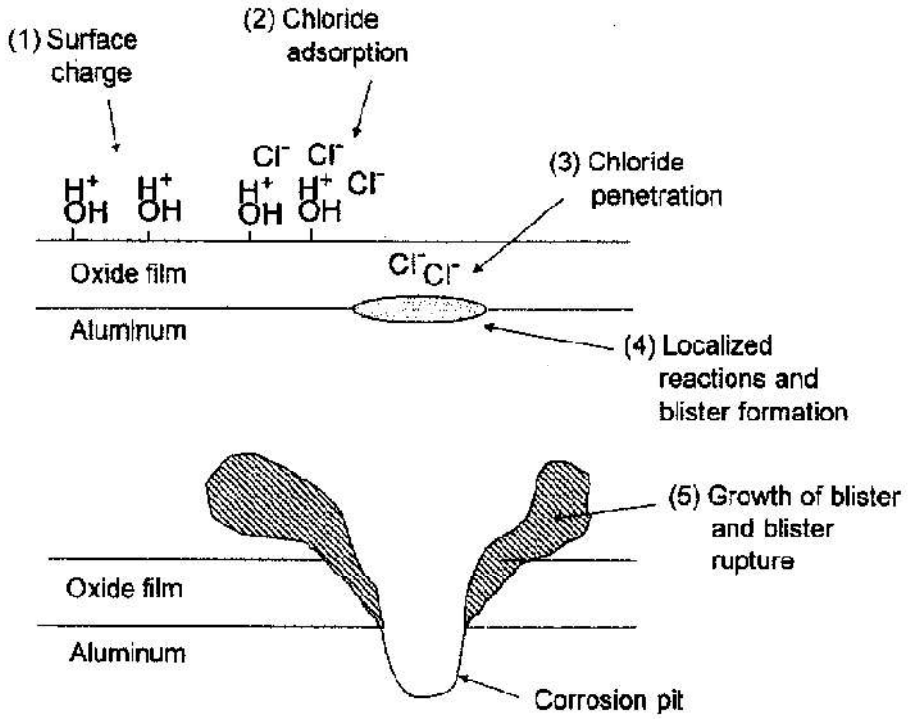

Figure 3.4: Initiation and propagation of pits during pitting of aluminium [96]

In an aqueous environment, the outer layer of an oxide film is positively charged as a result of interactions between hydroxyl groups present at the surface with protons in solution, forming an oxyhydroxide material [96, 108] according to the following equation:

$$AlOH + H^+ \rightarrow AlOH_2^+ \tag{3.28}$$

This positively charged surface will attract the negatively charged chloride ions resulting in Cl^- ions adsorption. Once the chloride anions penetrate into the oxide film, they migrate to the metal/oxide film interface triggering a series of localised reactions which can lead to the formation of pits and the acidification of the local environment [96]. These reactions initiated by Cl^- ion attack of the passive film, are described as follows [109]:

$$Al_2O_3 + 6Cl^- + 6H^+ \rightarrow 2AlCl_3 + 3H_2O \tag{3.29}$$

$$Al(OH)_3 + Cl^- \rightarrow Al(OH)_2Cl + OH^- \tag{3.30}$$

$$Al(OH)_2Cl + Cl^- \rightarrow Al(OH)Cl_2 + OH^- \tag{3.31}$$

$$Al(OH)Cl_2 + Cl^- \rightarrow AlCl_3 + OH^- \tag{3.32}$$

$$AlCl_3 + Cl^- \rightarrow AlCl_4^- \tag{3.33}$$

Below the pitting potential, pit growth lasts for a limited period of time before repassivation takes place [110, 111]. However above this critical potential, pit growth proceeds in a stable manner and involves the reduction reactions of oxygen and hydrogen at cathodic sites surrounding the pits (as described in equations 3.16 and 3.19), combined with oxidation of aluminium at anodic sites (equation 3.17) within the pits [111]. The mechanism of pitting corrosion is illustrated in Figure 3.5.

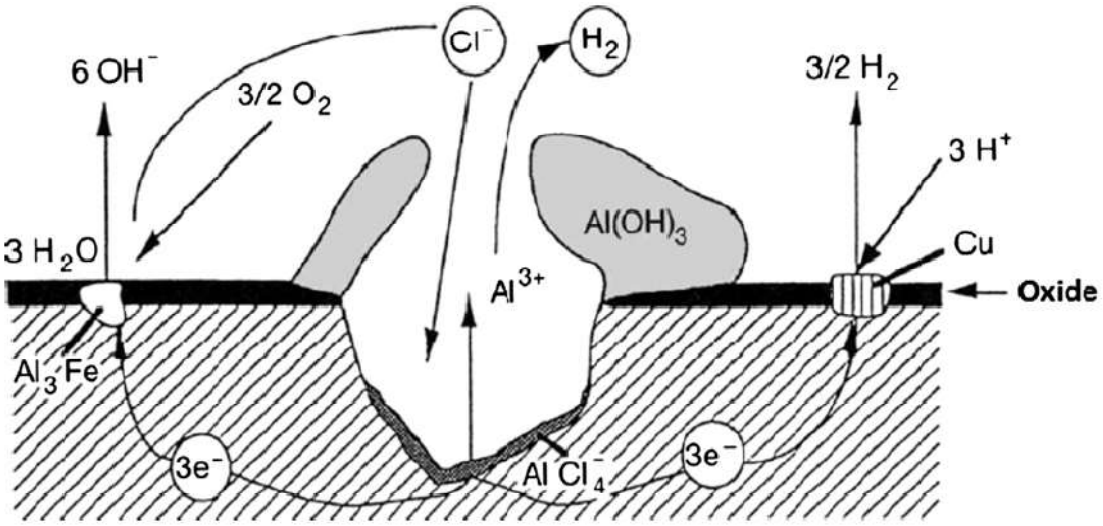

Figure 3.5: Pitting corrosion mechanism of an aluminium alloy (2014-T6 Al-alloy hence the presence of Cu and Al_3Fe) [111]

The Al ions (Al^{3+}) generated at the bottom of the pit undergo hydrolysis as they migrate towards the pit opening, resulting in the formation of $Al(OH)_3$ and H^+ ions, as described by the following equation [110, 112]:

$$Al^{3+} + 3H_2O \rightarrow Al(OH)_3 + 3H^+ \quad (3.34)$$

H^+ ions generated inside the pits have the effect of decreasing the solution pH which, depending on the level of acidification, can promote further pit growth [112].

3.2 Corrosion testing techniques

Accelerated corrosion tests were developed at the beginning of the 20th century [113] due to the need to accurately predict, over a shorter testing period, the corrosion performance of components in service. A large range of accelerated laboratory tests are now available with the salt spray test and electrochemical tests being the most extensively used.

3.2.1 The salt spray test (SST)

As one of the first accelerated laboratory tests, the salt spray (fog) test was developed with the aim to assess the corrosion resistance of materials exposed to a marine environment. It has gained popularity over the years, particularly in industry where it is used not only to evaluate the corrosion performance of various metals and coatings but also as a quality control tool [114]. To this day, the salt spray test remains one of the most widely used corrosion tests for two main reasons: it is simple to perform and the results are easy to understand [2].

Carried out in accordance with ASTM B117 [115], the test consists of mixing an aqueous solution containing 5 wt% NaCl (pH: 6.5 - 7.2) with some hot humid air to create a spray of salt water which is subsequently accelerated onto exposed samples in an enclosed cabinet (Figure 3.6). The test chamber is heated to 35^{o}C and the samples are continuously sprayed in a high humidity environment (at least 95% relative humidity [114]). As can be seen from Figure 3.6 below, the flat, rectangular test specimens typically 100 x 150 mm in dimensions, are usually hanged at 15 - 30 degrees from the vertical.

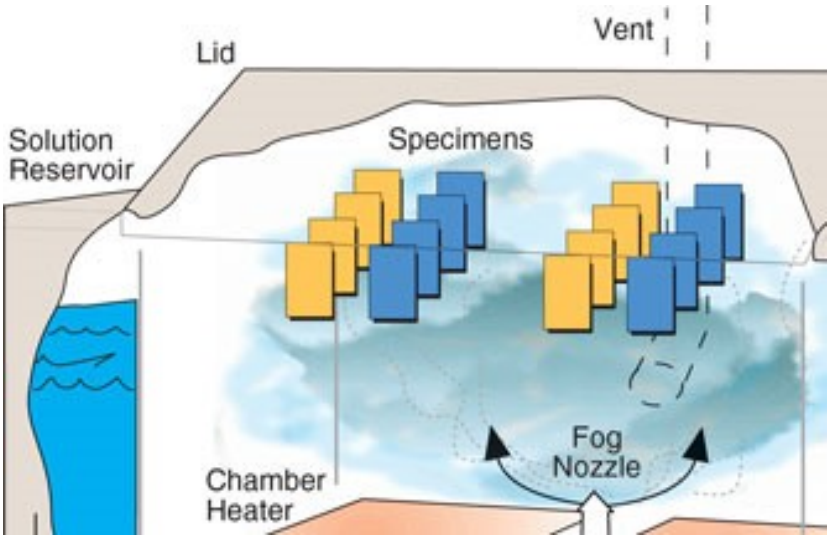

Figure 3.6: Schematic of a salt spray test chamber [116]

The test duration varies widely from 24 to 5000 hrs. SST parameters such as solution type, temperature and humidity levels can be modified so as to make the test environment more relevant to specific service conditions. For example, the copper accelerated acetic acid salt spray (or CASS) test was developed to assess the corrosion performance of coatings and anodised films exposed to more severe service environment [113, 114]. In this test, copper chloride is added to the sodium chloride solution and the minimum chamber temperature is 49^{o}C [114]. Other types of tests include the acidified synthetic seawater (fog) test and the sulfur dioxide test [113, 114]. Experiments can also be performed cyclically by exposing samples to wet and dry conditions at regular intervals [114].

Despite its popularity, the SST presents many drawbacks, the main one being the lack of correlation between SST results and in-service performance [2]. This is due to two reasons:

1) The high NaCl content used during testing to accelerate corrosion is not representative of the levels found in real service environment [2, 117]
2) The samples remain wet throughout the test as they are constantly exposed to the salt spray, which does not mimic real life conditions and may prevent some metals from forming a protective oxide film [117]. Cyclic tests have been developed to try and minimise this issue [118].

Another drawback lies in the fact that the results are not quantifiable but can only be presented in qualitative form. However, electrochemical corrosion tests (which will be discussed in the next section) offer more accurate prediction of the corrosion performance of materials and coatings, with the added advantage that the test results can be expressed quantitatively.

3.2.2 Electrochemical Impedance Spectroscopy (EIS)

3.2.2.1 Basics of EIS

EIS (also known as AC impedance spectroscopy) is a powerful, non-destructive technique used for investigating metal/solution interfaces, oxide films and surface treatments, as well as for evaluating the corrosion resistance of coatings [4, 96, 119]. EIS has become more popular over the years due to major advances in computer programs and instrumentation for the collection and measurement of impedance data [4]. The test consists of applying a small amplitude AC signal (typically 5 - 20 mV) to an electrochemical system and measuring its subsequent response over a large range of frequencies (usually 0.01 - 100,000 Hz) [96]. The electrode subjected to this AC perturbation will relax into a new steady state. The time taken for this to occur is known as the time constant or relaxation time τ (in seconds) [4, 96, 119] expressed as follows:

$$\tau = RC \tag{3.35}$$

Where R is the resistance and C, the capacitance of the system under investigation.

According to Ohm's law, the applied potential is directly related to the measured current as given by the following equation:

$$V = IR \tag{3.36}$$

Where V is the voltage, I, the current and R, the resistance.

Impedance, which is the equivalent of resistance in an AC circuit, is defined as the resistance to the flow of an alternating current and expressed as:

$$E = IZ \tag{3.37}$$

Where E is the potential, I the current and Z the impedance. Z is dependent on the frequency of the applied signal.

EIS presents many advantages, making it a very useful tool for studying the corrosion behaviour of coatings. One of the benefits of this technique lies in the ability to apply a small amplitude signal which has little or no effect on the properties being measured. Moreover, compared to other electrochemical techniques, EIS provides more detailed information of the system under study and can even differentiate between several electrochemical reactions occurring at the electrode surface [4]. Another advantage is that EIS data can be presented in quantitative form. In order to get an accurate picture of the processes taking place in a particular electrochemical system, it is essential to carefully interpret the EIS data collected.

3.2.2.2 Interpretation of EIS data

EIS data are usually presented in the form of Nyquist and Bode plots. The impedance can be expressed as a complex number given by:

$$Z = Z' - j.Z" \tag{3.38}$$

Where Z' is the real part of the impedance, Z'' the imaginary part and j is a complex number ($j = \sqrt{-1}$).

The Nyquist plot (also known as a Cole-Cole plot or Complex Plane plot) is a plot of the imaginary part of the impedance against its real part at a given frequency [120, 121]. Nyquist

plots however have one main disadvantage, in the fact that they do not show the frequency at which the data is recorded. This is not an issue with Bode plots, where the frequency is represented on the x-axis with the absolute value of impedance and phase shift on the y-axes. Examples of Nyquist and Bode plots are illustrated in Figure 3.7 below.

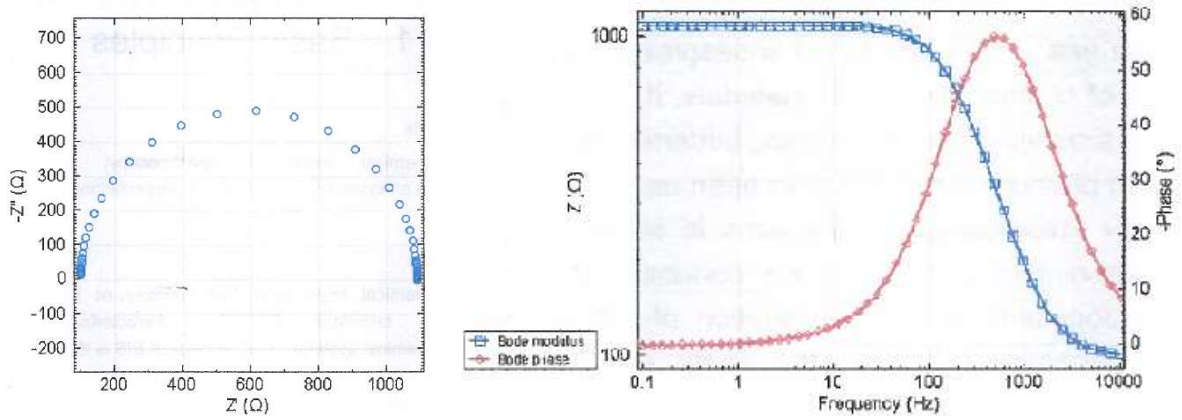

a) b)

Figure 3.7: Examples of a) a Nyquist plot and b) a Bode plot [121]

EIS data can also be interpreted using equivalent circuit models. Since it is known that the behaviour of electrochemical systems can be represented by simple electrical circuits [120], equivalent circuits generally consist of a network of passive electrical elements (e.g. resistors, capacitors, inductors) that are arranged in series and parallel [119, 122]. The elements in the model should be carefully selected so as to accurately represent the physical and electrochemical characteristics of the system under investigation [119, 120]. A typical equivalent circuit model for a coated metal substrate is illustrated in Figure 3.8 below.

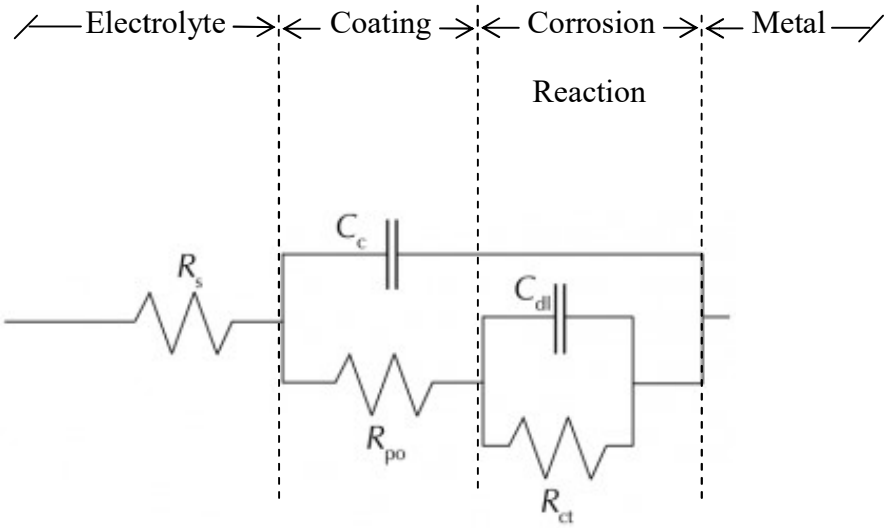

Figure 3.8: Schematic of a typical equivalent circuit model of a coated metal substrate undergoing corrosion [123, 124]

R_s is the solution resistance, also known as the uncompensated resistance or the ohmic resistance. It is defined as the resistance of the electrolyte between the working electrode (the coated metal) and the reference electrode [124]. R_s varies depending on the conductivity of the electrolyte. EIS analysis of coatings generally uses highly conductive electrolytes therefore R_s tends to be very low and is often negligible (i.e. in the range of 1 to 50 Ω) [122, 124].

C_c and R_{po} represent the processes taking place at the coating/electrolyte interface when a coated metal is immersed in an electrolyte. C_c is the capacitance of the undamaged coating. It is directly related to the dielectric constant of the coating ε, according to the following equation:

$$C_c = \frac{\varepsilon \varepsilon_0 A}{d} \tag{3.39}$$

Where ε_0 is the dielectric constant in vacuum (8.86 x 10^{-14} F/cm [4]), A is the coating area and d is the coating thickness.

The dielectric constant ε is affected by the coating permeability, such that the higher the permeability, the higher is ε and hence the higher the coating capacitance [4, 122]. The pore resistance R_{po} is defined as the resistance of a coating exposed to an electrolyte. The pore resistance tends to decrease over time as the electrolyte penetrates into the coating [124]. In effect, R_{po} provides useful information about the protective nature of a coating and how this can change with time [96].

The corrosion reactions taking place at the metal/electrolyte interface are represented by two electrical elements, C_{dl} and R_{ct}, arranged in parallel. C_{dl} is the double layer capacitance. It arises due to the existence of an electrical double layer at the metal/electrolyte interface, consisting of charged ionic species in solution moving towards and balancing charged species at the electrode surface. The charges on either side of the interface are separated by an insulating space, causing the electrode to act as a capacitor [123, 125]. Measuring C_{dl} usually implies that some coating degradation has occurred to enable contact between the bare metal and the electrolyte [124]. C_{dl} is generally much higher than C_c (at least by one order of magnitude [4]) and depends on many factors such as electrode potential, temperature, ionic concentrations, types of ions, oxide layers, electrode roughness, to name a few [122]. R_{ct} is the charge-transfer resistance associated with the transfer of charges across the metal/electrolyte interface during an electrochemical reaction. It is inversely proportional to the corrosion rate [124]. Like C_{dl}, the rate at which the charge transfer reactions occur is dependent on many parameters including electrode potential, temperature and electrolyte concentration [125].

3.2.3 Other accelerated electrochemical tests

The growing need for ever faster corrosion tests which would enable the accurate evaluation of the corrosion performance of components over a much shorter period of time, has led to the development of unconventional accelerated tests such as Rapid Electrochemical Assessment of Paint (REAP) and AC-DC-AC cyclic tests. Both techniques were initially developed as a means to quickly assess the corrosion properties of paints (i.e. organic, non-conductive thin films, primarily). These accelerated tests induce coating failure over much shorter test duration by exposing the test sample to a more aggressive environment while ensuring that the failure mechanisms remain unchanged [126].

3.2.3.1 Rapid Electrochemical Assessment of Paint (REAP)

A team of researchers led by Kendig developed the REAP test in 1996 with the aim of providing, within a 24-hour time period, information predicting the time-to-failure (TTF) of organic coatings on metallic substrates for the automotive industry [5]. The test is a combination of EIS measurements to assess the barrier properties of the coating and DC cathodic polarisation to induce corrosion damage at the metal/coating interface (cathodic disbondment). The experimental set up consists of an electrochemical cell containing the reference electrode (i.e. a SCE) and a counter electrode (usually platinum or any other noble metal) immersed in a solution of 0.5 M NaCl. A large area (around 56 cm^2) of a painted sample is then connected to the cell and the EIS measurements are carried out straight after immersion and again after 24 hours [126]. For DC cathodic polarisation, an identical sample is first of all scribed to remove the coating thereby exposing the metal substrate. The scribed marks consist of two lines, each 2 cm in length and intersecting each other at 90 degrees to form a cross. While immersed in 0.5 M NaCl solution, the scribed sample is subjected to an

applied potential of -1.05 V over a period of 24 hours. At the end of the experiment, an adhesive tape is applied onto the scribed area and pulled to reveal the extent of coating delamination. The average width of the pull-back area is measured and used to estimate the disbondment rate of the coating (dx/dt) from the following equation:

$$\frac{dx}{dt} = \frac{average\ width\ of\ scribe\ mark\ (mm)}{total\ test\ duration\ (hrs)} \tag{3.40}$$

Values of dx/dt are typically in the range of 0.1 mm/hr or lower [127] but, if no coating delamination is observed, then dx/dt is assumed to be 10^{-4} mm/hr [5].

EIS analysis is carried out based on the data recorded from the two EIS experiments. From the results an appropriate equivalent circuit model can be obtained which enables two other REAP parameters to be determined:

- The water uptake in volume percent ($\%v$) calculated from any measured change in coating capacitance (C_C) according to the formula:

$$\%v = 100\ \frac{\log(C_f/Ci)}{\log 80} \tag{3.41}$$

  Where C_f and C_i are the final (at t = 24 hrs) and initial (at t = 0 hrs) coating capacitance respectively.

- The corrosion resistance R_{cor} of the coated metal, obtained from the final EIS measurement after 24 hours of testing.

Using those 3 parameters, Kendig et al. [5] have been able to predict the pull-back TTF from the following equation:

$$TTF = -830.1 + 118\, log\, R_{cor} - 169.2\, log\, \frac{dx}{dt} - 48.03\, \%v \qquad (3.42)$$

Although the constants (i.e. regression coefficients) may change, depending on the metallic/organic substrate/coating system under investigation, it is clear from the equation that while a high R_{cor} value will lead to a longer time to failure, high values of dx/dt and $\%v$ would have the opposite effect.

3.2.3.2 AC/DC/AC cyclic test

The AC/DC/AC cyclic test combines EIS measurements obtained by applying an alternating current (AC) with cathodic polarisation carried out by imposing a direct current (DC) on a test sample. This sequence of AC impedance measurements followed by DC cathodic polarisation is repeated as many times as required to induce coating damage. The technique was first developed in the early 1990s by Hollaender et al. [128, 129] to evaluate the corrosion properties of coated metals (i.e. Al foils coated with organic polymer laminates) for the food packaging industry. Over the years it has been successfully adapted by Suay et al [130, 131] for testing powder and liquid paints applied to steel substrates for the automotive sector.

The test procedure can be described in 4 main steps as illustrated in Figure 3.9:

I. EIS measurements are performed on the coated substrate to assess the initial condition of the coating.

II. DC cathodic polarisation is carried out for a pre-defined period of time to stress the coated system, resulting in coating degradation and / or delamination.

III. A relaxation period, during which the OCP of the coated sample is allowed to return to a stable value.

IV. Further EIS measurements, to re-assess the condition of the coating after DC cathodic polarisation (and relaxation / recovery).

Steps II to IV can be repeated many times throughout the test, depending on the properties of the coating under investigation (such as its permeability to ions or its adhesion to the substrate). The EIS measurements performed after each DC/OCP step are used to determine the extent of coating damage that occurs after each cycle. The EIS data collected are interpreted using equivalent circuit models.

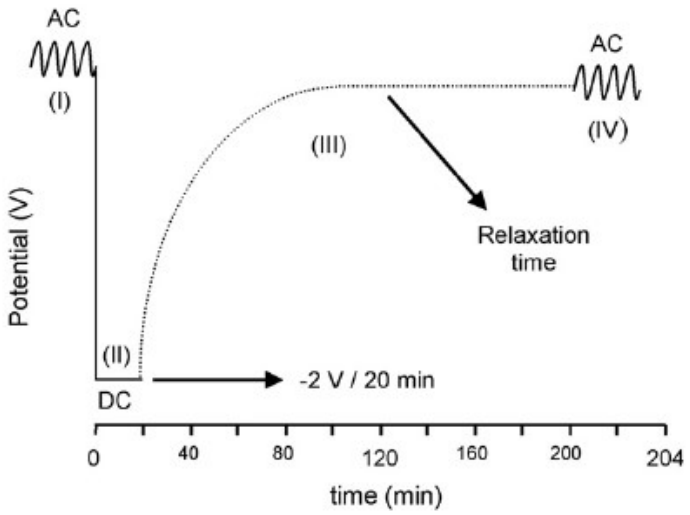

Figure 3.9: Schematic of an AC/DC/AC cyclic test [131]

The AC/DC/AC cyclic test uses a similar experimental set up to that of the REAP test with the electrochemical cell consisting of three electrodes; namely, a coated sample acting as the

working electrode, a standard reference electrode (typically a SCE) and a counter electrode (e.g. a platinum sheet) immersed in an aqueous electrolyte (usually 3.5 wt% NaCl). During DC cathodic polarisation, a negative potential is imposed on the coated sample (i.e. the cathode) causing electrolysis of the electrolyte due to the passage of an electric current through it. Electrolysis of the diluted NaCl solution generates positively-charged cations (H^+ and Na^+) which are attracted to the negatively-charged cathode and negatively-charged anions (Cl^- and OH^-) attracted to the positively-charged anode (i.e. the counter electrode). Oxidation and reduction reactions involving those ions take place at the anode and cathode respectively.

At the anode, hydroxide ions are oxidised to form water and oxygen according to the following equation:

$$4OH^- \rightarrow 2H_2O + O_2 + 4e^- \qquad E^0_{O_2/OH^-} = -0.40V \tag{3.43}$$

The chloride ions (Cl^-) also present at the anode do not oxidise to form chlorine gas (Cl_2) as per the equation below, but instead remain as anions in solution due to the high potential required for this reaction to occur.

$$2Cl^- \rightarrow Cl_2 + 2e^- \qquad E^0_{Cl_2/Cl^-} = 1.358\text{V} \tag{3.44}$$

At the cathode, three reduction reactions are possible:

$$2H^+ + 2e^- \rightarrow H_2 \qquad E^0_{H^+/H_2} = 0V \tag{3.45}$$

$$2H_2O + 2e^- \rightarrow H_2 + 2OH^- \qquad E^0_{H_2O/H_2} = -0.828 \tag{3.46}$$

$$Na^+ + e^- \rightarrow Na \qquad E^0_{Na^+/Na} = -2.711V \tag{3.47}$$

However, reducing hydrogen ions and water is much easier than reducing sodium ions, which therefore means that hydrogen gas is the main product formed at the cathode.

While the hydrogen gas formed beneath the coating causes it to physically delaminate as illustrated in Figure 3.10, the presence of hydroxide ions also contributes to coating delamination and degradation through increasing the alkalinity of the electrolyte [126, 131, 132].

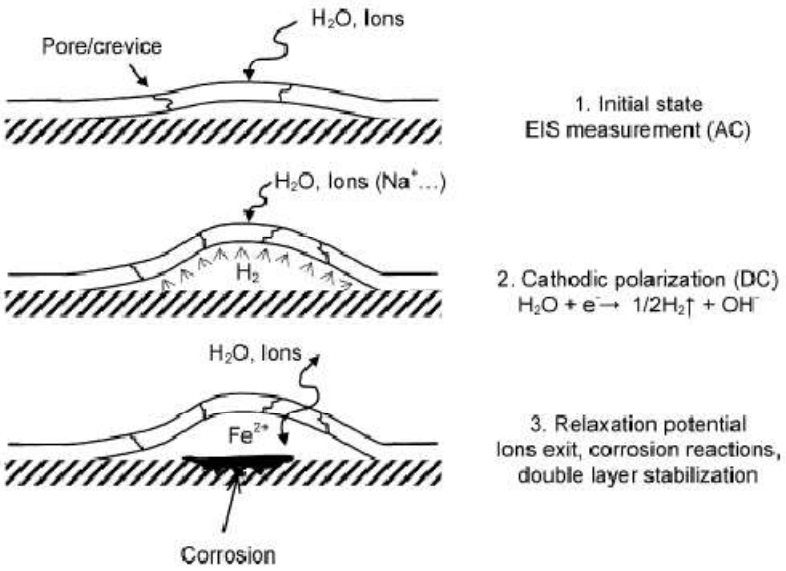

Figure 3.10: Schematic of the effect of the AC/DC/AC cyclic test on a coated metal system [131]

Once the cathodic polarisation step is terminated corrosion of the substrate usually follows, leading to the formation of iron oxides and hydroxides at the corrosion sites (Figure 3.8) [131].

Therefore damage to the coating/substrate system induced by cathodic polarisation occurs due to the loss of coating/substrate adhesion (mainly caused by the presence of H_2 underneath the coating), the formation of pores in the coating enabling ionic species to penetrate through and reach the substrate and lastly the formation of corrosion products at the substrate surface [131].

The relaxation step, during which the potential of the system is allowed to return to a stable value, usually occurs in 2 main stages:

- the first stage of relaxation occurs rapidly with the potential of the system quickly reaching values in a range above -1V as soon as DC polarisation is stopped
- the second stage of relaxation is much slower and corresponds to the electrolyte and ionic species migrating out of the coating [130]

Hydrogen permeation during DC cathodic polarisation

As mentioned above, hydrogen ions (H^+) are attracted to the negatively biased cathode during DC cathodic polarisation. At the cathode surface, a series of reactions are likely to take place leading to the formation and evolution of hydrogen gas ($H_{2(g)}$) and the absorption of hydrogen atoms (H_{abs}) into the coated sample [6].

First of all, H^+ ions in solution react with electrons to form adsorbed hydrogen atoms (H_{ads}) as follows:

$$H^+ + e^- \rightarrow H_{ads} \quad (3.48)$$

H_{ads} subsequently reacts in two ways, either chemically (3.49) or electrochemically (3.50) to form hydrogen gas ($H_{2(g)}$) according to the following equations:

$$H_{ads} + H^+ + e^- \rightarrow H_{2\,(g)} \quad (3.49)$$

$$2H_{ads} \rightarrow H_{2\,(g)} \quad (3.50)$$

Occurring simultaneously with these reactions is the absorption of hydrogen atoms into the metal substrate as described below:

$$H_{ads} \rightarrow H_{abs} \quad (3.51)$$

Equation 3.48 proceeds depending on the H^+ ion concentration of the electrolyte. Therefore the higher the number of H^+ ions present, the higher the number of H_{ads} produced. According to Yan et al [133], the reduction of H^+ into H_{ads} (eq. 3.48) occurs rapidly as the adsorption energy of hydrogen on the metal surface is large. Furthermore if the passive film permeability to hydrogen is high, hydrogen absorption according to equation 3.51 will be fast, causing both reactions 3.49 and 3.50 to be slow due to the reduced number of H_{ads} available at the metal surface. However, if the passive film permeability is low (dense protective film formed) then the rate of hydrogen absorption into the metal would be lower than the rate at which hydrogen gas is produced (from equations 3.49 and 3.50) due to the increased number of H_{ads}. In this case the abundance of H_{ads} at the metal surface will also enable reaction 3.48 to be reversed with H_{ads} losing electrons to form H^+. A summary of these mechanisms is illustrated in Figure 3.11.

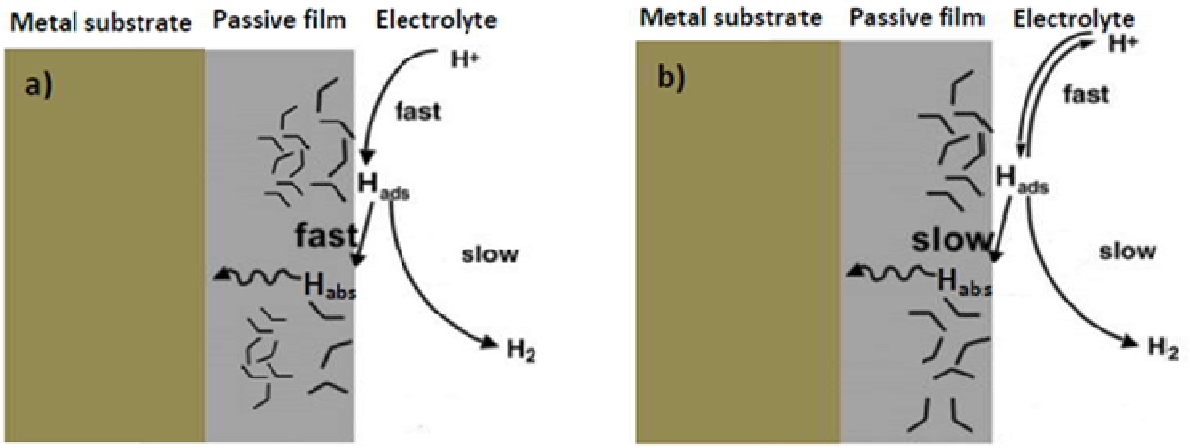

Figure 3.11: Description of the mechanisms of hydrogen evolution at the passive film/ electrolyte interface in the case of a) a porous film and b) a dense film [6, 133]

Hydrogen permeation through a metal during cathodic polarisation is therefore strongly influenced by the nature of the passive film present on the substrate surface. Other factors which may affect the hydrogen permeation rate include surface cleanliness and the presence of defects [134]. Hydrogen permeation has been extensively studied, as reported in chapter 2, with techniques such as the Devanathan-Stachurski electrochemical cell developed in order to measure hydrogen permeation current throughout the polarisation/corrosion process. Hydrogen evolution during DC cathodic polarisation generally takes place in three main stages [6]: the initial stage called the time lag (t_L) is defined as the time required to achieve a steady flow of hydrogen through the metal substrate after imposing a negative potential [134]. This is followed by the charge transient stage, which sees an increase in the hydrogen permeation current as hydrogen progressively diffuses through the metal. In the third and final stage a new steady-state is observed as hydrogen atoms at the metal surface (H_{ads}) reaching saturation level, hindering further diffusion into the metal and instead combining to form hydrogen gas according to equation 3.50.

3.2.3.3 Modified AC/DC/AC technique for testing metallic coatings

As mentioned in the previous section, the AC/DC/AC cyclic test was originally developed to assess the performance of electrically insulating coatings on metallic substrates. Until recently, the technique had not been used to evaluate the corrosion resistance of electrically conductive coatings on metallic substrates. Instead, techniques such as the salt spray test (SST) and conventional EIS (after periodic passive immersion in an aqueous corrosive media) have been extensively used for that purpose. While the simplicity of the test procedure is one of the advantages of the SST, it does not provide any quantitative analysis and the test environment is not representative of the actual working conditions the coated components would be exposed to [2]. The EIS technique on the other hand has seen its popularity rise over the years as it presents many benefits including the ability to provide accurate and quantitative information regarding the conditions of a coating / substrate system [119]. However both techniques are quite time-consuming. While the SST is typically carried out for a minimum of 1000 hours, EIS analysis is performed at regular intervals, over a long period of time in order to get an accurate picture of the degradation mechanisms of a coated system. Unlike these two techniques, the AC/DC/AC cyclic test can provide useful information regarding the corrosion behaviour of a coated metal within a relatively short time period. Indeed the cyclic nature of the test enables stress to be introduced periodically to induce damage to the coating/substrate system (during cathodic polarisation) while subsequently using EIS to investigate the failure mechanisms after each cycle. Recently Indeir et al [135, 136] have modified the test procedure by adding a pH probe to the experimental set up in order to monitor the evolution of the solution pH, an important parameter which affects the rate at which corrosion reactions take place - particularly when

trying to evaluate the properties of inorganic (and often electrically-conducting) coatings. The conventional three-electrode electrochemical cell is therefore augmented with a pH probe, which is connected to a pH meter and supported by pH monitoring software to enable real time recording of the solution pH. This useful addition has been shown to provide more detailed and accurate information regarding the damage mechanisms unfolding during the test.

In this work, the improved AC/DC/AC cyclic test was used to assess the corrosion performance of PVD Al-based coatings while simultaneously evaluating the usefulness of the technique as a tool for discriminating between metallic coatings of different composition and structure.

Chapter 4

Experimental Procedure

In this study, PVD Al-based coatings were deposited on 15/5 PH and 17/4 PH precipitation-hardening stainless steel substrates by electron beam PVD (EBPVD) and magnetron sputtering. This chapter describes in detail the coating deposition processes and the analytical techniques used to assess the coatings' properties. These include structural and compositional analyses using a scanning electron microscope (SEM) with EDAX capability, mechanical testing using an instrumented hardness tester, micro-abrasion wear testing and corrosion tests using an improved AC/DC/AC cyclic DC-polarisation/impedance-spectroscopy test to assess the corrosion performance and durability of the coatings under adverse conditions.

4.1 Substrate materials

Two types of substrate materials were used in this work: 15/5 PH and 17/4 PH. Both substrates are martensitic precipitation-hardened stainless steel, used commonly for components requiring combined high strength and corrosion resistance [137]. They are widely used for structural and dynamically-loaded parts in aerospace applications (e.g. spherical bearings) and so are ideal substrate materials when assessing the corrosion performance of the Al-based coatings. The chemical composition of the substrate materials

obtained from EDX analysis of the surface is presented in Table 4.1. The measured values are comparable to those found in the literature.

Table 4.1: Chemical composition of 15/5 PH and 17/4 PH substrate materials

	Composition (wt. %)						
Material	**Fe**	**Cr**	**Ni**	**Si**	**C**	**Cu**	**Mn**
15/5 PH	Balance	15 ± 0.1	4.6 ± 0.1	0.2 ± 0.03	1.7 ± 0.4	2.8 ± 0.02	0.8 ± 0.03
17/4 PH	Balance	15.3 ± 0.2	4.1 ± 0.2	0.3 ± 0.02	1.3 ± 0.03	2.5 ± 0.2	0.7 ± 0.1

Both substrate materials were supplied in the form of test discs (30 mm diameter, 3 mm thick) with a 3 mm hole drilled to one side (Figure 4.1) which was used for hanging each sample vertically in the chamber by passing a string of annealed 316 stainless steel wire through it. The test discs were received with a highly-polished surface finish of around 0.01 µm Ra.

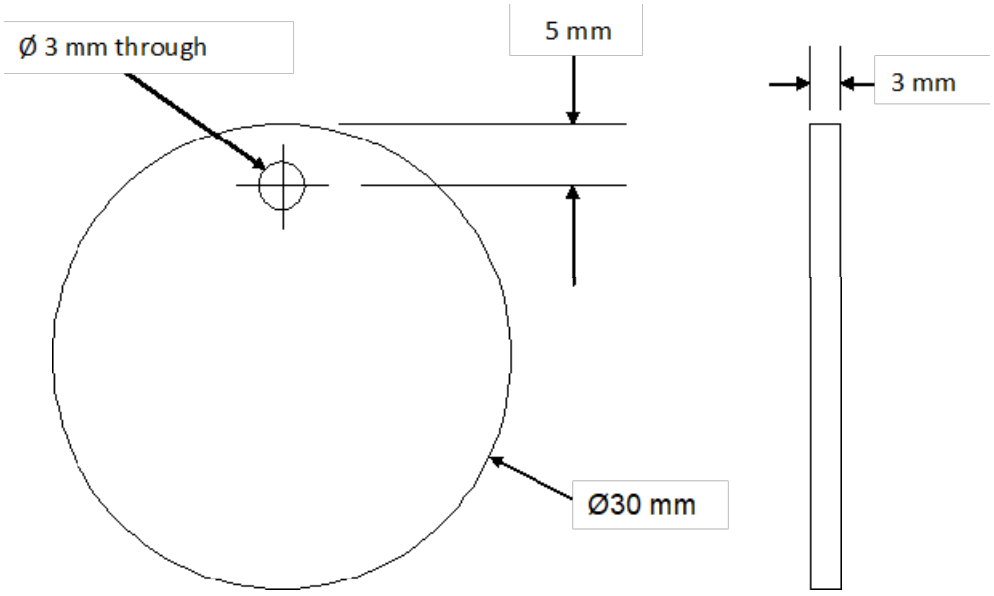

Figure 4.1: Test disc schematic

4.2 Sample preparation and cleaning

Prior to coating deposition, the test samples were rigorously cleaned to remove all surface impurities which could have a detrimental effect on the coating/substrate adhesion. The samples were placed in a cleaning basket and guided through an automated cleaning line where they were ultrasonically cleaned in two tanks of alkaline solutions heated to 60^{o}C and rinsed in tanks containing reverse osmosis (RO) water. They were subsequently dried in a hot nitrogen tank at 120^{o}C. The cleaning process typically lasts around 25 minutes. The cleaned samples were then placed inside the treatment chamber, ready for PVD coating.

4.3 Coating deposition equipment and processes

Two PVD techniques, namely Electron Beam Physical Vapour Deposition (EBPVD) and Closed-Field Unbalanced Magnetron Sputtering (CFUBMS), were investigated for the deposition of metallic Al-based coatings. Coating deposition by these processes generally takes place in two stages. First of all the coating material is made to undergo a phase transformation from solid to vapour with the second stage involving the migration and condensation of the vapour onto the surface of the components to form the coating. The two processes differ in the way the material to be deposited is transformed from solid to vapour. While EBPVD relies on thermal evaporation of a molten source, magnetron sputtering uses high energy ion bombardment of a solid target material in order to vaporise it. These two PVD techniques were used extensively during the initial trials to enable the deposition of metallic Al-rich deposits, although the coatings described in this thesis were deposited by magnetron sputtering as the coating rig was fully automated which enabled repeatable

deposition of thick and dense coatings with very little operator input variability. Both techniques are described in more detail in the following sections.

4.3.1 Electron Beam PVD (EBPVD)

4.3.1.1 EBPVD coating deposition equipment

A coating machine generally consists of a deposition chamber, a pumping system to enable the process to be carried out at high vacuum and a set of power supplies used during coating deposition. A schematic of the coating chamber and pumping system used in this study is illustrated in Figure 4.2.

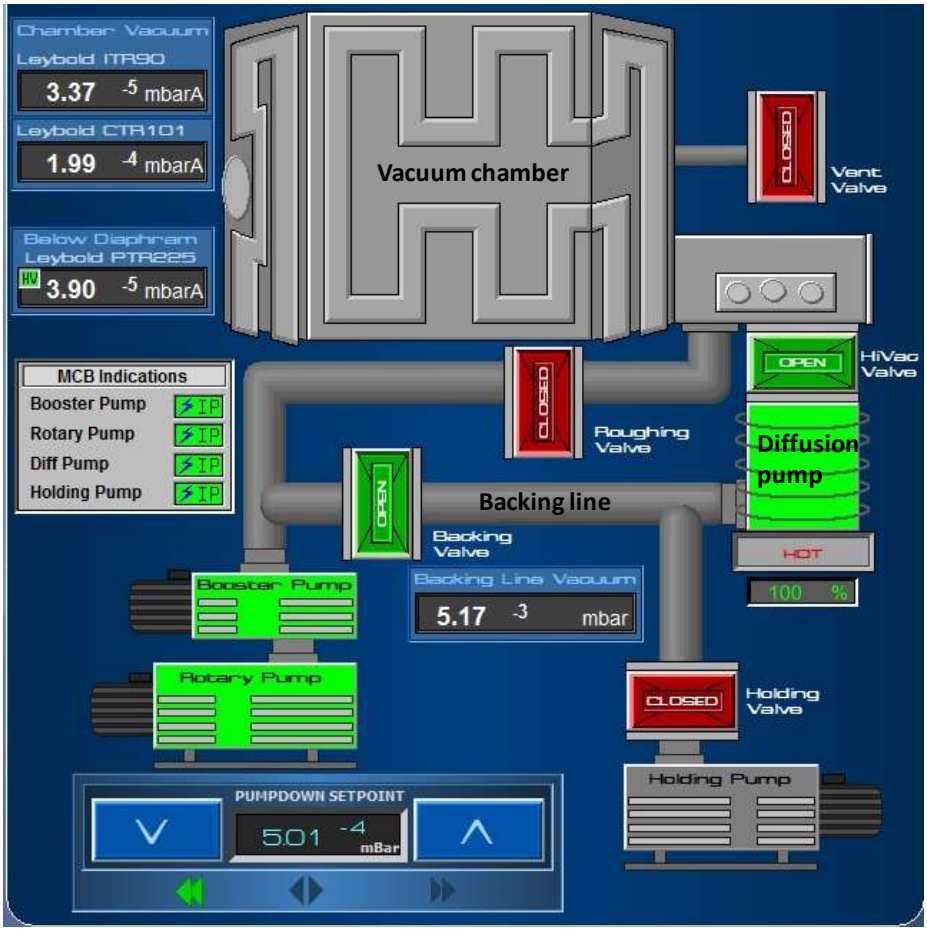

Figure 4.2: Schematic of the EBPVD coating chamber and pumping system

As shown in Figure 4.2, the pumping system consists of four main pumps: two rotary pumps (one of which is called the holding pump), a roots pump (or booster pump) and a diffusion pump. Rotary pumps generally operate at pressures ranging from atmospheric (~ 1 x 10^5 Pa) down to 0.01 Pa. Roots pumps can reach slightly lower pressures (around 0.001 Pa) while diffusion pumps operate in the pressure range from 10 Pa up to 10^{-8} Pa, enabling the chamber to reach a high vacuum state. Roots pumps which cover the pressure range between the rotary and the diffusion pumps are used to increase the overall pumping speed of the system – hence they are often referred to as booster pumps. In the set up illustrated above, a booster pump is connected to a rotary pump and both are used in the first stage of pumping (the roughing stage). The second rotary pump is called the holding pump and its main function is to maintain a low pressure in the backing line during the roughing stage. A summary of the vacuum pumps used are provided in Table 4.2.

Table 4.2: Type of pumps used to achieve the required vacuum in an EBPVD chamber

Vacuum pump	**Manufacturer**	**Model**	**Operating pressure range (Pa)**
Rotary vane pump	Oerlikon Leybold Vacuum	D40B	10^5 - 10^{-2}
Roots (booster) pump	Oerlikon Leybold Vacuum	WAU251	10^3 - 10^{-3}
Rotary (holding) pump	Oerlikon Leybold Vacuum	D25B	10^5 - 10^{-2}
Diffusion pump	Oerlikon Leybold Vacuum	DIP8000	10 - 10^{-8}

The pumping sequence used to evacuate the coating chamber is described as follows:

- Step 1: the rotary and booster pumps are activated with the roughing valve open allowing the chamber to be evacuated down to a pressure of around 8 Pa. The holding pump and diffusion pump are also switched on with the holding valve open to maintain a relatively low pressure in the backing line (~ 0.5 Pa).

- Step 2: once the target pressure set point is reached, the roughing valve is closed to terminate the roughing stage. The holding valve is also closed.
- Step 3: the backing valve is opened.
- Step 4: the HiVac (stands for 'high vacuum') valve which connects the diffusion pump to the chamber is then opened, enabling a progressively higher vacuum to be achieved. Pressure values as low as 10^{-4} Pa have been measured in this vacuum system.

As mentioned above, several power supplies connected to different components in the chamber are operated during the deposition process (Table 4.3). These include:

- A workpiece bias power supply which biases the workpiece (i.e. carousel, carousel arms, jigging fixtures and components to be coated) negatively, with respect to the chamber walls
- A filament bias power supply connected to a tungsten filament
- A crucible bias power supply which biases the crucible(s) positively, with respect to the chamber walls
- An EB high-voltage power supply which powers the EB gun(s)

Table 4.3: Power supplies used during the EBPVD coating deposition process

Power supply	**Manufacturer**	**Model**	**Power (kW)**
Workpiece bias	Hüttinger Electronic	BP48	48
Filament bias	Hüttinger Electronic	Scalo 30	90
Crucible bias	Hüttinger Electronic	TruPlasma Bias 3018	18
EB gun	Telemark	TT15 LK0020	15

4.3.1.2 Process description

During electron beam PVD the coating material, which is generally in the form of a solid slug positioned inside a water-cooled copper crucible, is evaporated by magnetically focussing a high energy electron beam onto it, with the resultant vapour migrating towards the workpiece where it condenses to form the coating. For the AlCr(N) deposited by EBPVD, the coating materials (i.e. Al and Cr) were evaporated from two separate slugs by directing individual beams of electrons onto each slug surface. The electron beams were generated in a high vacuum plenum chamber at a pressure below 0.1 Pa by thermionic emission from a heated tungsten filament located inside the EB gun assembly. A high negative bias voltage (i.e. -7 kV) was applied to accelerate the electrons away from the filament and a magnetic field was used to deflect the electron beam through 270 degrees [138], directing it through a slot in the deposition chamber floor into the appropriate crucible. A positive bias was applied on each crucible in order to attract more electrons onto each evaporant slug (enhancing the evaporation of coating material) and to increase the level of ionisation of the vapour present just above the slugs. The components to be coated were biased negatively to attract positively charged metal ions as they enter the workpiece cathode sheath - as well as to accelerate secondary electrons emitted from the workpiece into the plasma negative glow region, where they can cause further ionisation. A tungsten filament was used in the deposition chamber volume to further enhance ionisation of the plasma. This negatively biased filament was heated to emit electrons (by thermionic emission) which were subsequently accelerated into the plasma. Argon was used as the carrier gas during coating deposition. The twin-crucible EBPVD coating rig consisting of two separate crucibles which can house two different coating materials is shown in Figure 4.3. A schematic of the process chamber configuration is

shown in Figure 4.4. This set-up enabled the evaporation of more than one element at a time, hence making it possible to produce alloy coatings over a wide range of compositions.

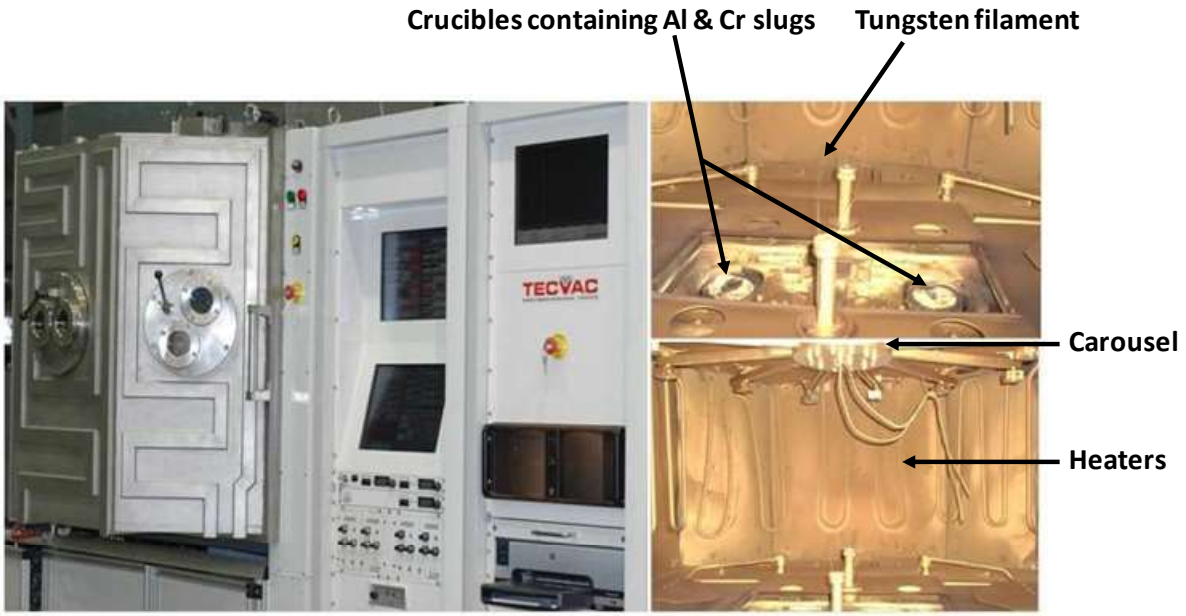

Figure 4.3: EBPVD coating deposition rig

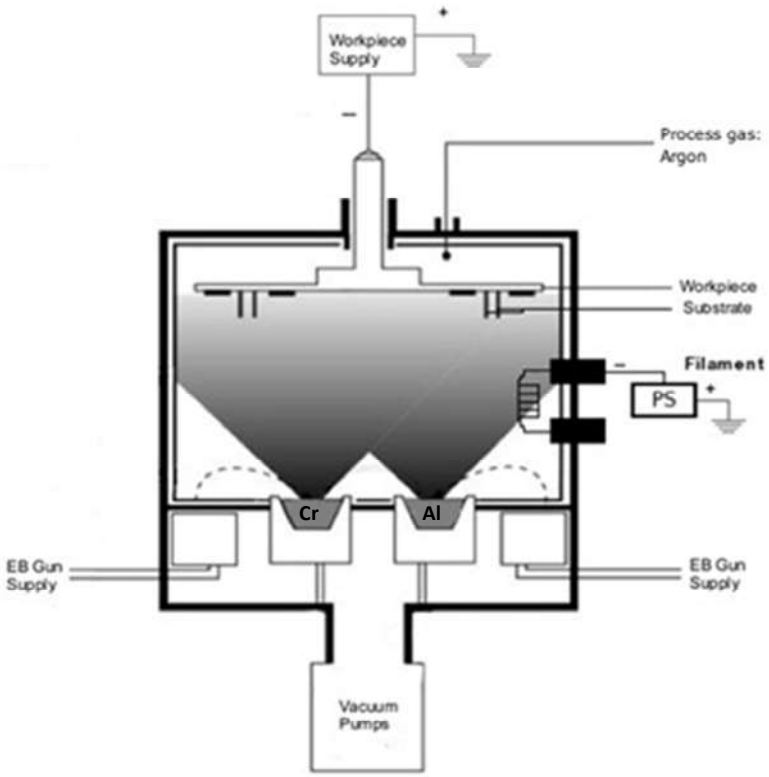

Figure 4.4: Schematic of twin EBPVD coating deposition rig chamber

A range of AlCr(N) coatings containing various amount of chromium and nitrogen were deposited using this technique. The process parameters used during the initial trials are listed in Table 4.4.

Table 4.4: Process parameters used in the deposition of AlCr(N) coatings by EBPVD

	AlCr(N) process parameters
Temperature (^{o}C)	300 - 400
Substrate bias voltage (V)	-50
Argon base pressure (Pa)	0.3
Nitrogen flow rate (sccm)	20 - 75
Filament bias voltage (V)	-150
Crucible bias voltage (V)	+50

The EBPVD system presents many advantages. It enables the evaporation and deposition of a variety of materials and alloys. Furthermore, unlike magnetron sputtering or cathodic arc evaporation PVD processes, the rate of evaporation from the source(s) is independent of the plasma parameters. It is a versatile process which can be used to deposit coatings over a wide range of temperatures. Its high deposition rate is also a major advantage, making it possible for newly developed coatings to be successfully produced on an industrial scale. However, depositing thick coatings (above 10 μm) while maintaining stable process conditions can be a challenge – particularly when researching new coating compositions. In this study we were unable to deposit AlCr(N) coatings with thickness above 5 μm in a repeatable manner which was one of the reasons for switching to magnetron sputtering as the main coating deposition technique for subsequent trials. Indeed during the trials to increase the coating thickness, it became evident that as more Al and Cr were evaporated, process parameters such as the Al/Cr ratio (obtained by Optical Emission Spectroscopy (OES), a technique used to collect photons of light characteristic of each element present in the plasma) were more difficult to

closely control. This is because as the amount of Cr and Al in each slug decreases, it becomes necessary to move the EB spot around in order to find more material to evaporate which causes fluctuations in the Al and Cr counts (number of photons collected per unit time) leading to unstable process conditions. The other reason for choosing magnetron sputtering was to enable the deposition of Al-based coatings at lower process temperatures (below 200^{o}C) which would be ideal in applications where thermally-sensitive materials (such as low-alloy steels or high-strength aluminium alloys) are used.

4.3.2 Closed-Field Unbalanced Magnetron Sputtering (CFUBMS)

4.3.2.1 Magnetron sputtering coating deposition equipment

With a similar set up to that of the EBPVD coating deposition rig, the magnetron sputter machine consists of a vacuum chamber connected to a pumping system and several power supplies. In this case however, the high vacuum diffusion pump was replaced by two turbomolecular pumps for two main reasons: 1) the turbo pumps are more environmentally-friendly (no oil used, therefore providing the added benefit of reducing the maintenance service requirements) and 2) they offer a much faster pumping speed (1280 l/s for N_2 [139]) which is essential due to the size of the deposition chamber (measured working volume of around 1.12 m^3 compared to 0.72 m^3 for the EBPVD machine). The magnetron sputter chamber and pumping system are illustrated below (Figure 4.5) with details of the type of pumps used summarised in Table 4.5.

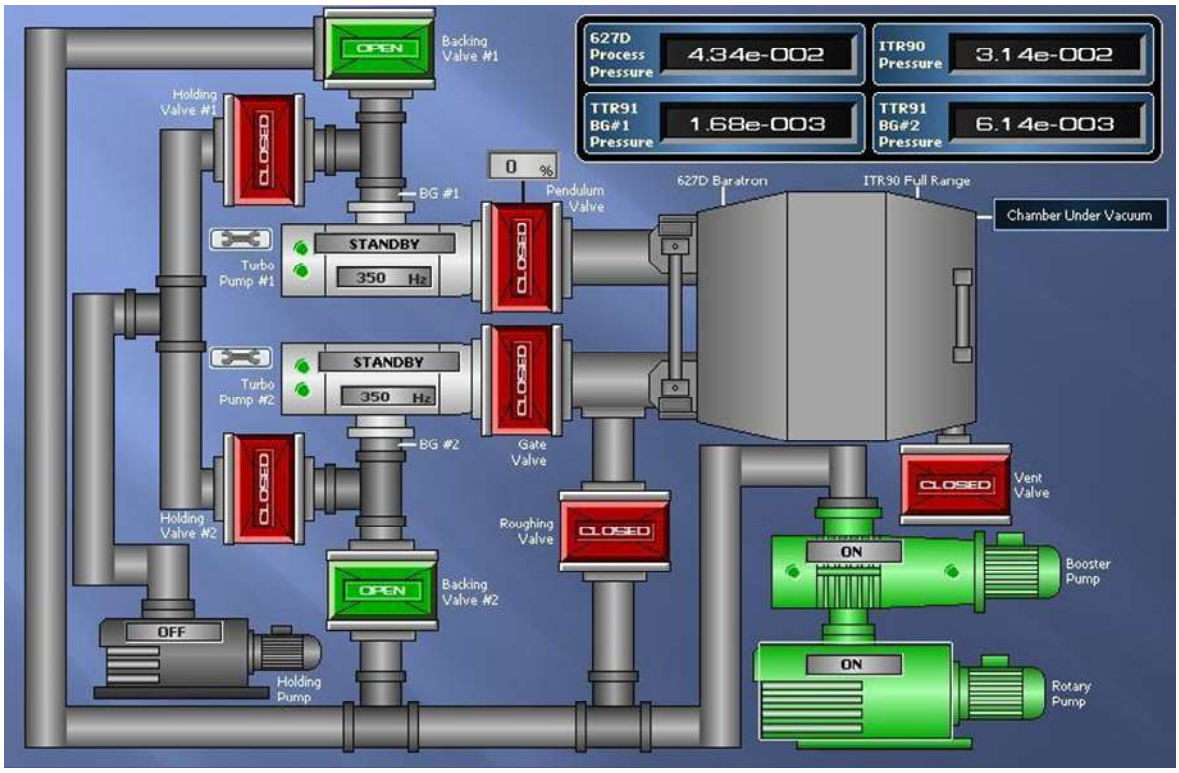

Figure 4.5: Schematic of the magnetron sputter coating chamber and pumping system

Table 4.5: Types of pumps used to achieve the required vacuum in a magnetron sputter chamber

Vacuum pump	Manufacturer	Model	Operating pressure range (Pa)
Rotary vane pump	Oerlikon Leybold Vacuum	D40B	10^{5} - 10^{-2}
Roots (booster) pump	Oerlikon Leybold Vacuum	WAU251	10^{3} - 10^{-3}
Rotary (holding) pump	Oerlikon Leybold Vacuum	D16B	10^{5} - 10^{-2}
Turbomolecular pump	Oerlikon Leybold Vacuum	TURBOVAC T1600	10 - 10^{-8}

The pumping sequence carried out in order to achieve a high vacuum in the chamber (with pressures in the range of 5 to 8 x 10^{-4} Pa) is identical to the one described for EBPVD in section 4.3.1.1.

Three main power supplies are used during the magnetron sputtering process. A workpiece bias power supply which biases negatively the components to be coated, a filament bias

power supply connected to a tungsten filament for thermionic electron emission and a DC-pulse power supply connected to each magnetron. Details of each power supply are provided in Table 4.6.

Table 4.6: Power supplies used during magnetron sputtering

Power supply	Manufacturer	Model	Power (kW)
Workpiece bias	Advanced Energy	Pinnacle Plus	10
Filament bias	Huttinger Electronic	TruPlasma Bias 3008	8
Magnetron	Advanced Energy	Pinnacle Plus	10

4.3.2.2 Process description

As mentioned above, magnetron sputtering was used to deposit thick PVD Al-based coatings on steel substrates at temperatures below 200^{o}C. The process involves the ejection of atoms from a target material by high energy ion bombardment followed by the deposition of the vaporised particles onto the substrate where they condense to form the coating [140]. Argon was used as the carrier gas during coating deposition. The argon atoms were ionised through collisions mainly with secondary electrons but also other energetic neutral and ionised species. The argon ions generated are accelerated towards the negatively biased target causing, upon impact and momentum transfer, the removal of coating material from the target (Figure 4.6). It has been reported that the energy of the impacting ions must be greater than 30eV in order to enable particle ejection from the target surface [138].

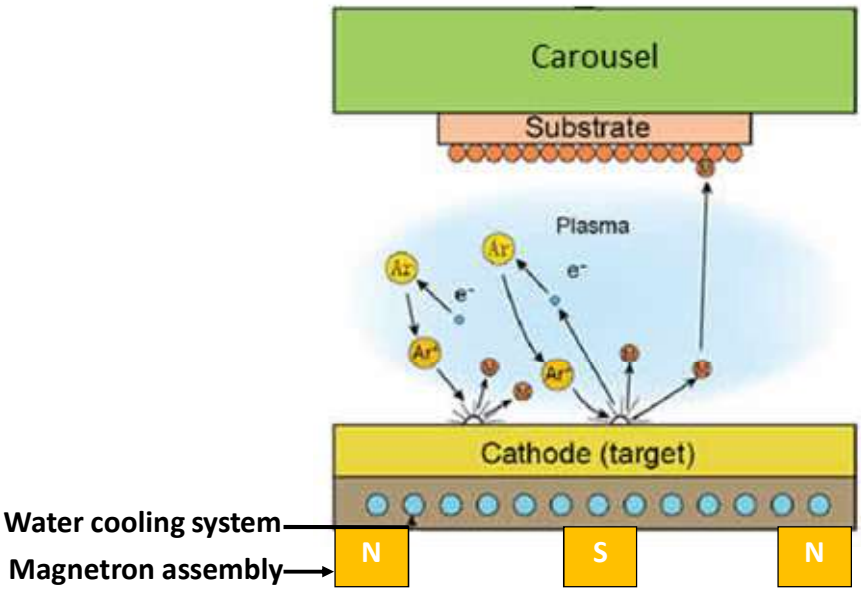

Figure 4.6: Schematic of the magnetron sputtering process (image adapted from [141])

A set of magnets is present behind each target and positioned in an unbalanced configuration such that the outer magnets are stronger than the inner magnet. This arrangement not only generates magnetic field lines between the outer and inner magnets (conventional magnetron sputtering) but also creates field lines which are directed away from the target towards the substrate. This configuration enables some secondary electrons to follow these newly generated field lines expanding the plasma away from the surface of the target, in the direction of the substrate where they can cause further ionisation. Generating more ions and electrons closer to the substrate effectively increases the ion bombardment at the substrate surface. High substrate ion current densities, in the range of 2 to 10 mA/cm^2, have been measured for unbalanced magnetron sputtering. These values are much higher than those reported for conventional magnetron sputtering (less than 1 mA/cm^2) [142].

The magnetron sputter coating rig used in this project (Figure 4.7) consists of six magnetrons (three on each chamber door as shown in Figure 4.8) fitted behind each target. An image of a magnetron and target assembly is illustrated in Figure 4.9.

Figure 4.7: Magnetron sputter coating deposition rig

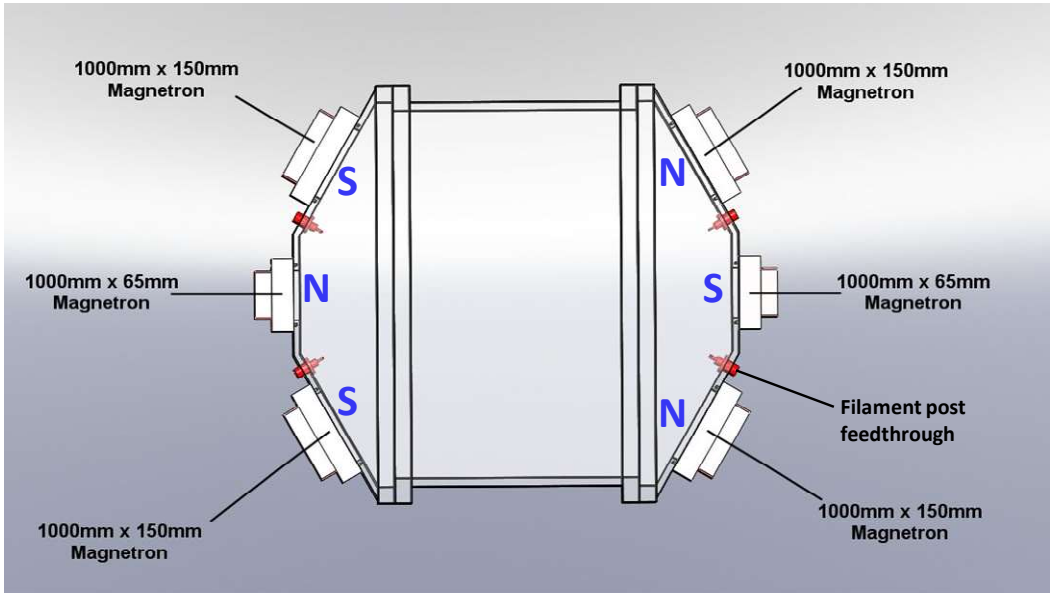

Figure 4.8: Magnetron configuration

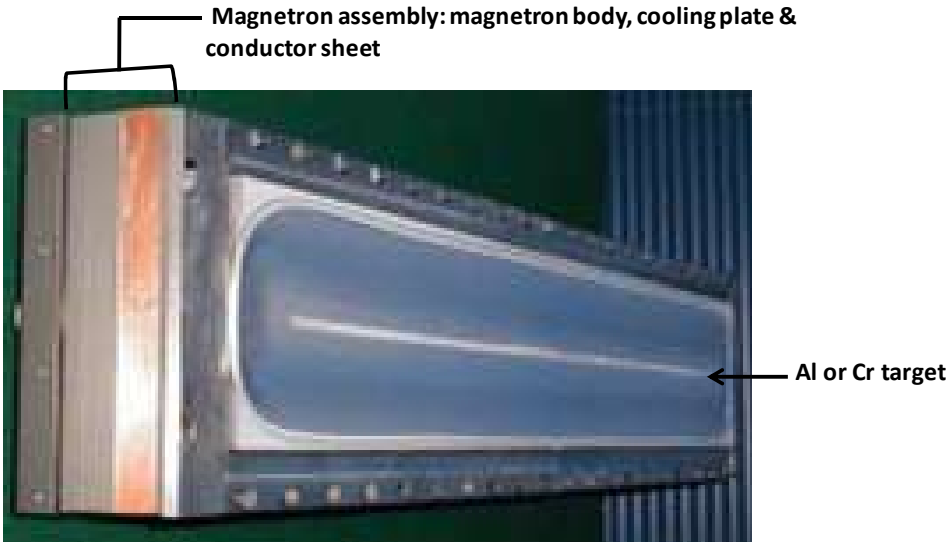

Figure 4.9: A magnetron assembly (image courtesy of Gencoa)

The magnetrons are arranged in a closed-field system whereby adjacent magnets have opposite magnetic polarities. This enables the field lines between magnetrons to become linked which minimises the loss of energetic secondary electrons to the chamber walls, resulting in an increase in the ionisation levels of the plasma and higher ion current densities nearer the substrate. Figure 4.10 illustrates the magnetic field lines generated as a result of the selected magnetron configuration.

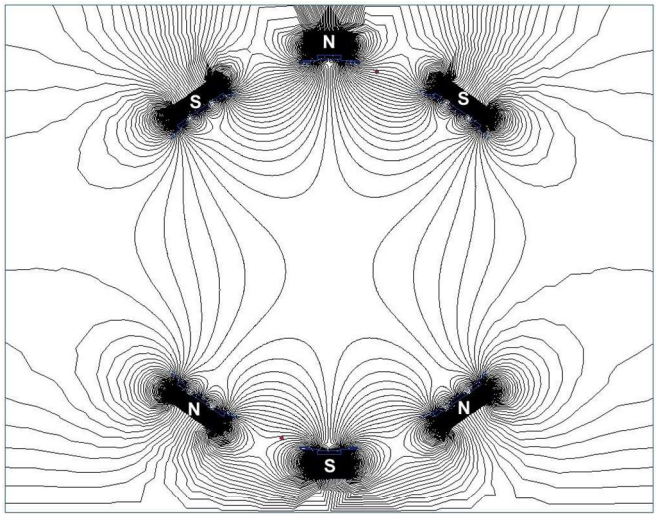

Figure 4.10: Schematic of the magnetron configuration displaying the magnetic field lines (image copywrite of Gencoa, reproduced with permission)

During the coating deposition process, a negative bias was applied on the workpiece in order to attract positively charged metal ions as they enter the workpiece cathode sheath and accelerate the secondary electrons generated into the plasma, enhancing the ionisation levels. A tungsten filament which enables electron generation by thermionic emission is sometimes used in order to further increase the ionisation levels in the plasma. However for the purpose of this work, coating deposition was carried out without the use of a tungsten filament so as to keep the process temperature below 200^{o}C.

4.3.2.3 Coating deposition parameters

PVD AlCr(N) coatings were deposited by magnetron sputtering on 15/5 PH steel substrates. The substrate temperature - which was monitored throughout the deposition process by inserting two thermocouples in a dummy part of similar shape and size to the components to be coated - was maintained below 200^{o}C. Such low temperatures are required in some cases when coating thermally sensitive materials (e.g. high strength low-alloy ferritic steels) and in other instances for swaged aerospace bearings, where internal surfaces have been lined with a low-friction polymer and exposure to elevated temperatures (i.e. above 170^{o}C) for an extended period of time can have a detrimental effect on the functional properties of the liners, eventually causing them to seize.

The magnetron sputtering rig was fitted with six metal targets: four large targets (1010 x 156 x 10 mm) and two small targets (1008 x 65 x 10 mm). The small (Cr) targets were used not only during the deposition of a thin pure Cr adhesive interlayer but also in combination with the large targets (made of Al or Cr) for the main coating deposition. The six targets were fitted on each door of the chamber and typically arranged as shown in Figure 4.9.

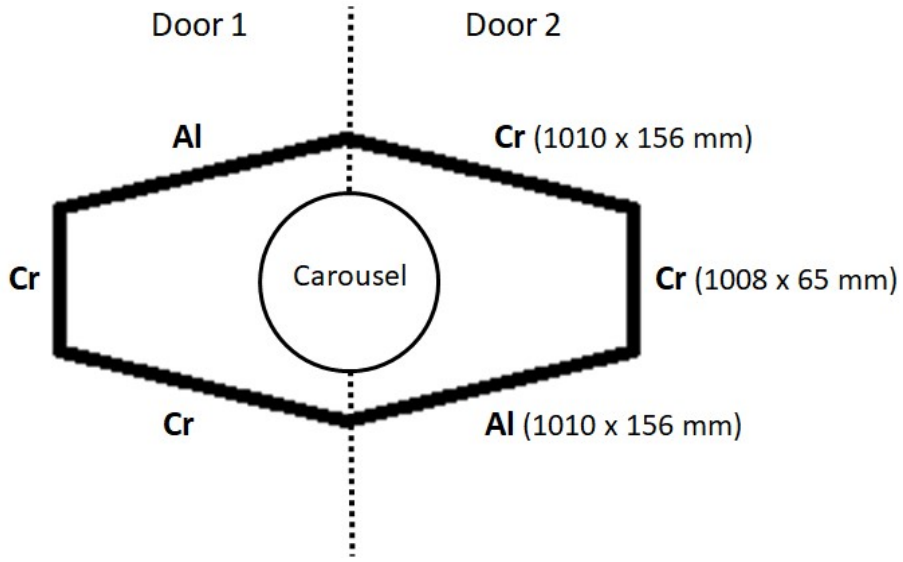

Figure 4.11: Schematic of targets positioning in the chamber for AlCr(N) coating deposition

The test discs to be coated were jigged on specialised fixtures and placed on a carousel which allows them not only to rotate past each of the targets at a set rotation speed but also to rotate along their own axis, enabling uniform coating deposition. The chamber is evacuated until a high vacuum is reached (below 0.1 Pa) before switching on the heaters. The heating step is essential in order to remove as much as possible of the moisture present in and around the chamber wall shields, as this could otherwise compromise the adhesion of the coating to the substrate. The test samples were heated to 150^{o}C and the substrate cleaning / coating deposition sequence was started once the chamber base pressure was below 0.005 Pa. The substrates were first of all sputter cleaned for 10 minutes in an argon diode plasma at a pressure of 2 Pa and a substrate negative bias of 500 V so as to remove all surface impurities prior to coating deposition. In all cases, a thin (~ 200 nm) pure Cr layer was deposited as the first coating layer, in order to improve the coating / substrate adhesion. During coating deposition, the substrate negative bias was set at 30 V, the argon base pressure at 0.5 Pa and the power on each magnetron was varied in order to adjust the Cr content of the coatings to achieve the targeted coating compositions. As soon as all the targets were at the correct

coating deposition set point, nitrogen gas was admitted to the chamber at a constant flow rate of 25 sccm and 35 sccm for AlCrN coatings with low (around 10 – 12 at%) and high (18 at%) nitrogen content, respectively. Table 4.7 provides a summary of the main deposition parameters.

Table 4.7: Process parameters used in the deposition of AlCr(N) coatings by magnetron sputtering

		AlCr(N) process parameters
	Temperature (^{o}C)	≤ 200
	Substrate bias voltage (V)	-30
	Argon base pressure (Pa)	0.5
	Nitrogen flow rate (sccm)	25 / 35
Al target set point	Voltage (V)	430 - 480
	Current (A)	16 - 19
Cr target set point	Voltage (V)	330 - 390
	Current (A)	1.5 - 4

4.4 Coating characterisation

A range of analytical techniques were used to assess the structural, mechanical, wear and corrosion properties of the Al-based coatings produced. A brief description of each technique and the associated equipment used in this study are provided in the following sections.

4.4.1 Scanning electron microscopy

A scanning electron microscope (Carl Zeiss EVO MA25, Figure 4.12) equipped with an Energy Dispersive X-ray (EDX) spectrometry system was used to observe the microstructure

and measure the thickness and composition of as-deposited Al-based coatings. It was also used to examine the corroded areas after AC/DC/AC cyclic corrosion testing, in order to assess the extent of coating damage that had occurred. The microscope used was fitted with a lanthanum hexaboride (LaB_6) filament which generates electrons by thermionic emission. The electron beam is subsequently accelerated by a high voltage (typically 20kV) through a set of condenser lenses, objective lenses and deflection coils which enable it to focus into a probe point that can be rastered across the surface of the sample [143]. The high energy incident beam hits the specimen surface causing, by transfer of the kinetic energy from the bombarding particles, the ejection of different types of electrons (namely secondary, backscattered and Auger electrons) and also causes X-rays to be emitted from the material (Figure 4.13) that can be spectroscopically analysed.

Figure 4.12: Scanning electron microscope (Carl Zeiss EVO MA25) [144]

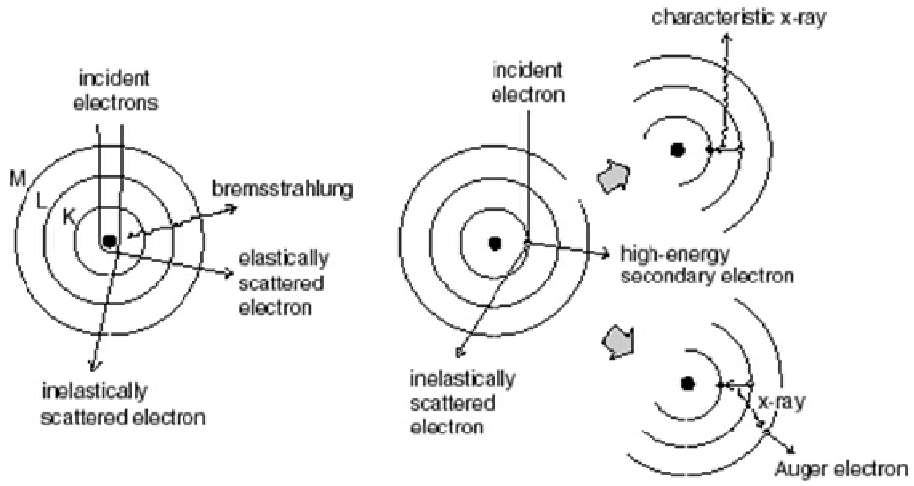

Figure 4.13: Different types of electrons and X-rays generated when an electron beam hits a sample surface [145]

The electrons generated are collected by the appropriate detectors. Images produced from secondary electrons (which are generated as a result of the inelastic scattering of incident primary electrons with atoms in the test samples) give topographical information of the sample surface. Backscattered primary electrons provide compositional contrast between chemically different areas - with regions of high atomic number appearing brighter since, the higher the atomic number (i.e. heavier substrate/coating atoms), the larger the collision cross-section for electrons to be backscattered. Emitted X-rays, generated when an electron from a higher energy shell moves to a lower energy orbital (in order to fill the void left by primary electron impact ejection of an inner electron) are detected by an EDX spectrometer. The energies of the X-rays collected are characteristic of each atom in a material, enabling elemental composition information to be obtained.

In this project, chemical and structural analyses of the Al-rich deposits were carried out at the surface of the test samples and along their cross-sections immediately after coating deposition in order to check the structural uniformity and determine the initial composition and thickness of the coatings under study. Surface analysis of the corroded areas was

subsequently performed to investigate any structural and compositional changes that may have occurred as a result of corrosion testing.

4.4.2 X-ray diffraction (XRD)

X-ray diffraction is a non-destructive technique used to determine the crystallographic structure of materials by identifying the different crystalline phases present and their preferred orientation. This analytical technique can also provide other useful structural information including the grain size, the average spacing between layers of atoms and a measure of any internal stresses generated within the material [145]. An X-ray diffractometer generally consists of an X-ray tube, a monochromator and a detector. The X-ray tube comprises an evacuated chamber in which sits a number of components, essential for the generation of X-rays:

- A source of electrons, typically provided by a heated tungsten filament which generates electrons by thermionic emission
- A metallic X-ray target source - generally made of copper (Cu), but other metals such as molybdenum (Mo), cobalt (Co), Iron (Fe) or chrome (Cr) can also be used
- A large potential difference (i.e. 20 – 50kV) between the two abovementioned electrodes, which ensures that electrons emitted by the tungsten filament (cathode) are accelerated at high speed towards the target X-ray source (anode)

Electrons bombarding the target surface cause the ejection of inner shell electrons from the target atoms. X-rays, characteristic of the target material, are generated when high energy electrons from the outer shells move to the inner shells to fill the void left by the ejected electrons. A K_{α} X-ray is produced when an electron from the L shell moves to the K shell to

fill the gap left by a dislodged K-shell electron while a K_β X-ray is generated when the void in the K-shell is filled by an electron from the M shell. K_α X-rays have higher intensities than K_β X-rays. Historically, metal foil filters were used to filter out K_β X-rays, with the choice of filter dependent on the anode material used. Adjacent metals with atomic numbers less than that of the anode metal (Z-1) were suitable filter materials therefore if for example a Cu anode is used, the metal foil filter will be made of nickel (Ni). Another way of generating a single-wavelength X-ray beam (K_α radiation) is by diffracting X-rays from single crystal monochromators which are generally made of materials such as graphite or germanium. The monochromatic beam is then collimated as it passes through a set of slits before being accelerated towards the specimen surface [146]. As the incident beam hits the sample, it causes electrons around the atoms to begin oscillating at the frequency of the incident beam, diffracting X-rays in all directions which will combine and interfere with each other, resulting in destructive interference. However if the atoms are arranged in a regular pattern, as is the case in a crystal, the electromagnetic waves generated will be in phase, thus interacting in a constructive manner to diffract well-defined X-rays (in different directions) - many of which will be collected by a strategically positioned detector. Constructive interference only occurs when Bragg's law is satisfied (Figure 4.14).

Bragg's law: $$n\lambda = 2d\,sin\theta \quad (4.1)$$

Where n is an integer, λ is the wavelength of the incident X-ray beam, d is the distance between atomic layers in a crystal and θ is the incidence angle.

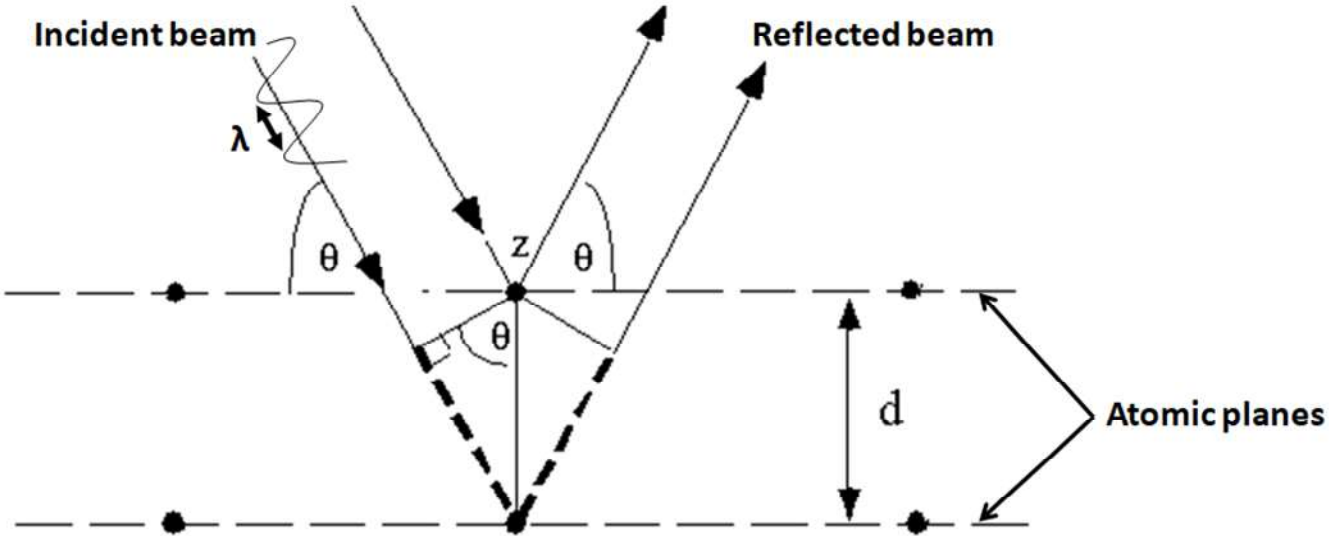

Figure 4.14: Schematic diagram of Bragg's law showing the conditions under which constructive interference occurs

In conventional XRD, the incidence angle θ (the angle at which the incident beam hits the sample surface) is equal to the angle of the diffracted beam with respect to the sample surface (Figure 4.15).

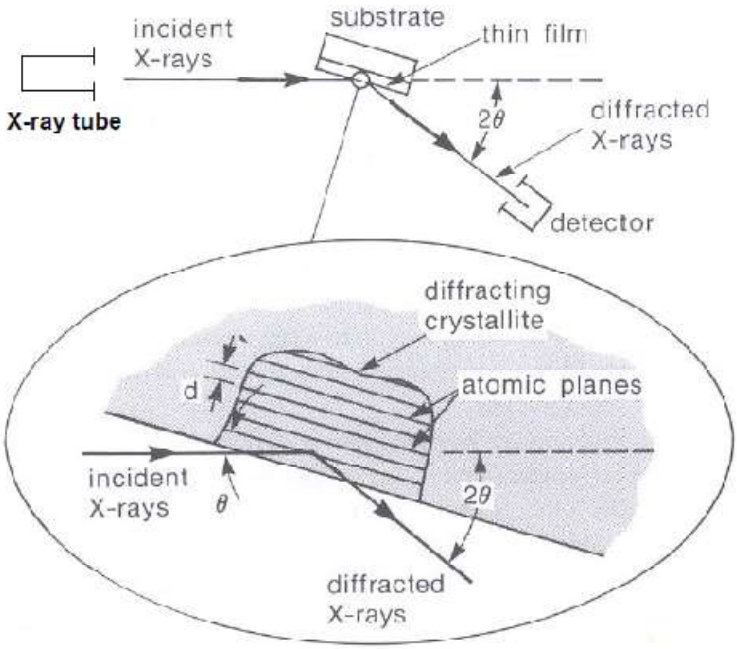

Figure 4.15: Schematic of a conventional XRD experiment. Image obtained from [105]

In this work, conventional XRD was performed on PVD Al-based coatings using a Bruker D2 Phaser X-ray diffractometer (Figure 4.16) with Cu-Kα radiation (λ = 0.15406 nm, tube voltage = 30kV, current = 10mA). Standard θ/2θ scans were carried out with the diffraction angle (2θ) set in the range of 30° to 100° at a step time of ~0.4 s per step size of 0.02°.

Figure 4.16: X-ray diffractometer (Bruker D2 Phaser). Image obtained from [147]

4.4.3 Mechanical testing

Hardness and elastic modulus measurements were carried out on Al-based coatings by instrumented indentation testing using a Fischerscope HM2000 equipped with a Vickers indenter (Figure 4.17).

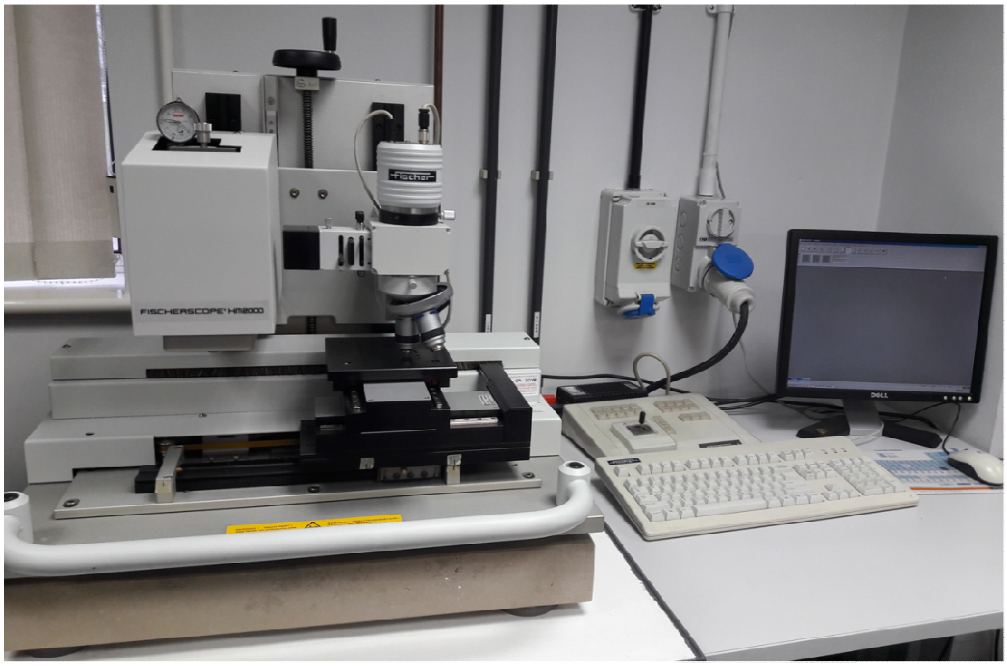

Figure 4.17: Fischerscope HM2000 instrumented indentation hardness tester

Instrumented indentation hardness testing enables the hardness of thin films to be measured accurately, by using very small indentation loads to minimise the substrate contribution. With this equipment, indentation forces in the range of 0.4 to 2000 mN can be applied. For the Al-rich coatings, a maximum indentation force of 50 mN was used in order to satisfy the Bückle rule, a widely known rule-of-thumb which advises that the maximum penetration depth be less than 10% of the overall coating thickness in order to minimise the effect of the substrate on the measured hardness and elastic modulus [148]. Although this rule is not universally true for all coating/substrate systems [149, 150], it has been proven to enable accurate measurements of the mechanical properties of hard coatings, particularly those with thickness ranging from 5 to 50 μm [150].

In instrumented indentation, an indenter pressed against the surface of a sample, is progressively loaded until the maximum predefined load is achieved (Figure 4.18). The displacement of the indenter tip is continuously monitored as the indenter penetrates deeper

into the sample with increasing load as illustrated in Figures 4.18 and 4.19 where h_{max} denotes the maximum indentation depth, h_f the permanent indentation depth once the applied load is removed and h_c the contact depth at the maximum indentation load which differs from h_{max} as a result of elastic deformation taking place in the area surrounding the indenter head. The resultant load-displacement curve (Figure 4.19) can be used to determine the coating hardness, H, according to the following equation:

$$H = \frac{Pmax}{A} \tag{4.2}$$

Where $Pmax$ is the maximum indentation load and A is the projected contact area at maximum load, which is obtained from the maximum indentation depth, h_{max}, and the radius of the indenter.

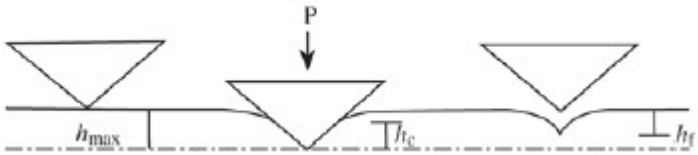

Figure 4.18: Schematic drawing of the loading / unloading of an indenter during hardness testing [151]

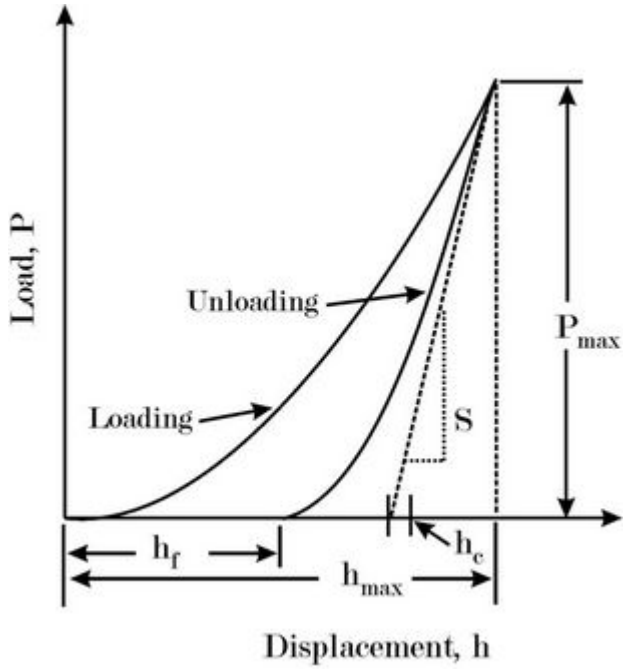

Figure 4.19: Schematic representation of the load-displacement curve [152]

The indentation modulus E_{IT} which is very similar to the elastic modulus can be calculated from the following equation [153]:

$$E_{IT} = \frac{1 - v^2}{\frac{1}{E_r} - \frac{1 - v_i^2}{E_i}} \tag{4.3}$$

Where v and v_i are the Poisson's ratios of the coating and the indenter respectively, E_i the modulus of the indenter and E_r the reduced modulus. E_r is related to the stiffness of the material S (obtained from the initial slope of the unloading curve) and the projected contact area A as given by the equation below:

$$E_r = \frac{S\sqrt{\pi}}{2\sqrt{A}} \tag{4.4}$$

Around 40 indentations were performed on each sample. The results presented in the following chapter are an average of those measurements.

4.4.4 Micro-abrasion wear testing

Micro-abrasion (also called ball cratering) wear testing was used to assess the wear resistance properties of the Al-based coatings under investigation. During the test, wear is generally initiated by rotating a ball in a controlled way against a flat coated surface in the presence of an abrasive medium (Figure 4.20) [154, 155].

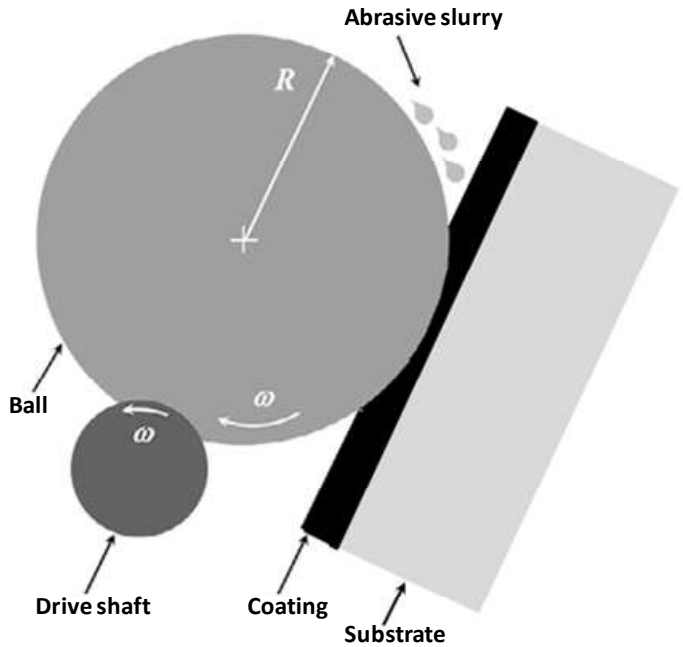

Figure 4.20: Schematic representation of the micro-scale abrasive wear test [156]

In this study, micro-scale abrasion testing was carried out in accordance with BS ISO 26424:2008 [157] using a Plint TE-66 micro-abrasion tester (Figure 4.21). Each test sample was mounted on a deadweight-loaded lever and placed in direct contact with a 1-inch (25.4 mm) diameter polished SAE 52100 steel ball. A test load of 0.1N was applied during each experiment. The abrasive media consisted of an aqueous suspension of SiC (grade P1200) particles with average size of 3.1 μm. The mixture of SiC particles and distilled water provided a slurry concentration of 0.2 g/ml. The steel ball was rotated at an average speed of 76.4 rpm (giving a tangential sliding velocity of 0.1 m/s). The test was carried out for a limited duration, defined in terms of number of cycles of ball rotation, so as to prevent perforation of the coating. Pre-defined numbers of 30 and 50 cycles were used during testing of each sample, which corresponded to sliding distances of 2.4 m and 3.9 m, respectively.

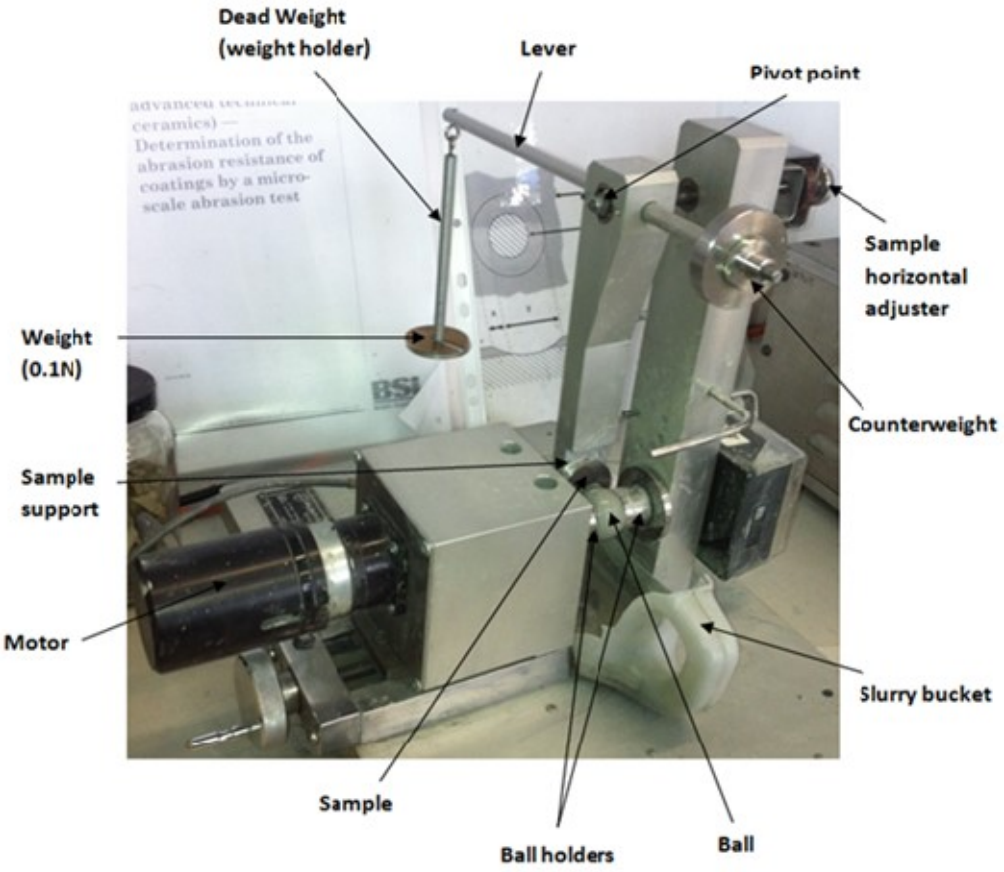

Figure 4.21: Micro-abrasion test equipment

From the size of the crater on the test sample it is possible to determine the wear volume V [154]:

$$V = \frac{\pi b4}{64R} \tag{4.5}$$

Where b is the radius of the crater and R the radius of the ball (for $b \ll R$).

The wear rate can then be calculated using the Archard wear law [154] which states that:

$$V = KSN \tag{4.6}$$

Where K is the wear rate, S the sliding distance and N the applied load.

Therefore the wear rate is: $$K = \frac{\pi b4}{64 \quad S\,N} \tag{4.7}$$

In this experiment, the wear volume was measured by non-contact optical surface profilometry (OSP) using a Zemetrics ZeScope™ 3D optical surface profilometer which relies on light interference to produce a 3D profile of the surface under study and provide a wide range of topographical information including surface roughness and wear volume. From the wear volume, the wear rate was then calculated using equation (4.7). The surface profilometer also provided depth profiles of each crater.

4.4.5 AC/DC/AC cyclic corrosion testing

Al-based coatings deposited in this study were subjected to laboratory corrosion testing, in order to study their corrosion behaviour in a controlled environment. As mentioned in Chapter 3, the AC/DC/AC cyclic test which combines open circuit potential measurements, DC cathodic polarisation and EIS analysis, was recently modified to include a pH meter so as to provide a more detailed picture of the corrosion behaviour of the (electrically-conductive) coatings under investigation [6].

4.4.5.1 Test set up

An electrochemical cell consisting of three electrodes immersed in 3.5 wt% NaCl was set up for the experiments. A fresh electrolyte was prepared before each test by mixing 34 g of reagent grade sodium chloride with 920 ml of deionised water in accordance with ASTM G44-99 [158]. The three electrodes consisted of a saturated calomel electrode (SCE) used as the reference electrode, a counter electrode made of platinum and a working electrode consisting of an AlCr(N)-coated 15/5 PH test disc with an area of 1 cm^2 exposed to the electrolyte. All three electrodes were connected to a Solartron SI 1287 electrochemical interface equipped with a 1250 frequency response analyser. A pH probe was also immersed in the electrolyte with the other end connected to a pH meter (HANNA, HI-5222-02) and a computer equipped with HANNA's proprietary software control desk, in order to monitor the solution pH throughout the duration of the test. Figures 4.22 and 4.23 represent the test equipment used and a schematic of the experimental set up, respectively.

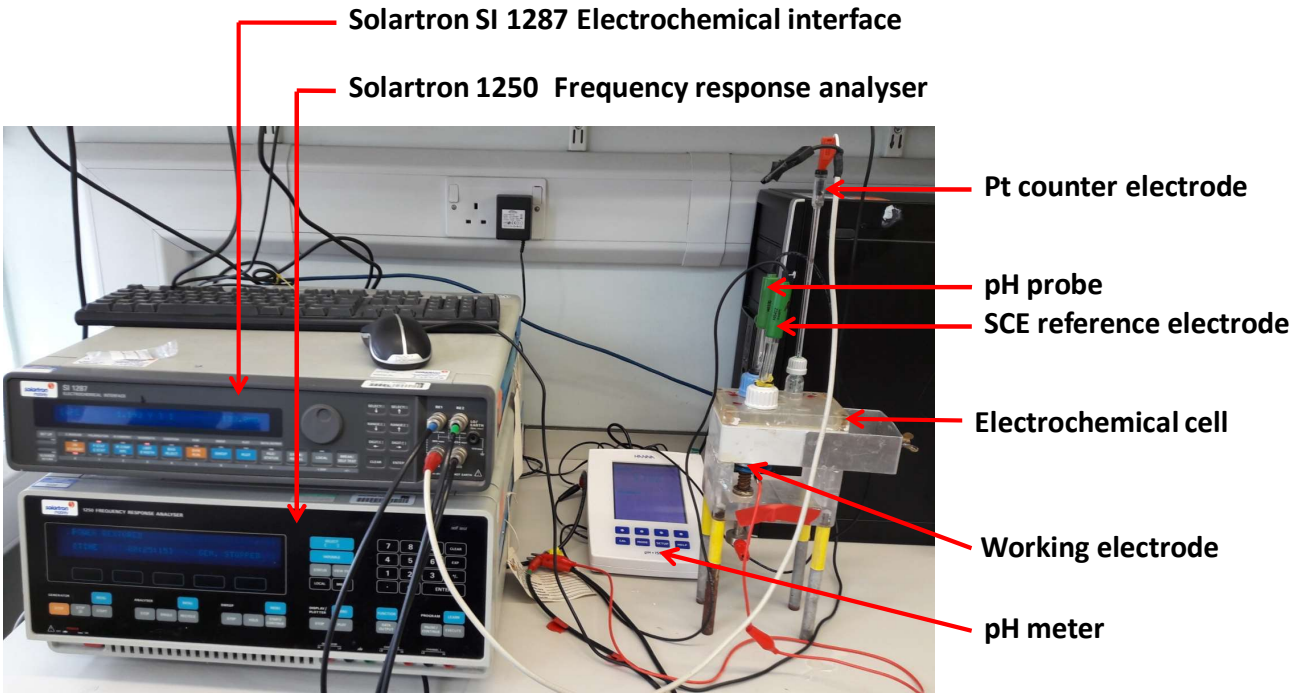

Figure 4.22: Corrosion test equipment configuration

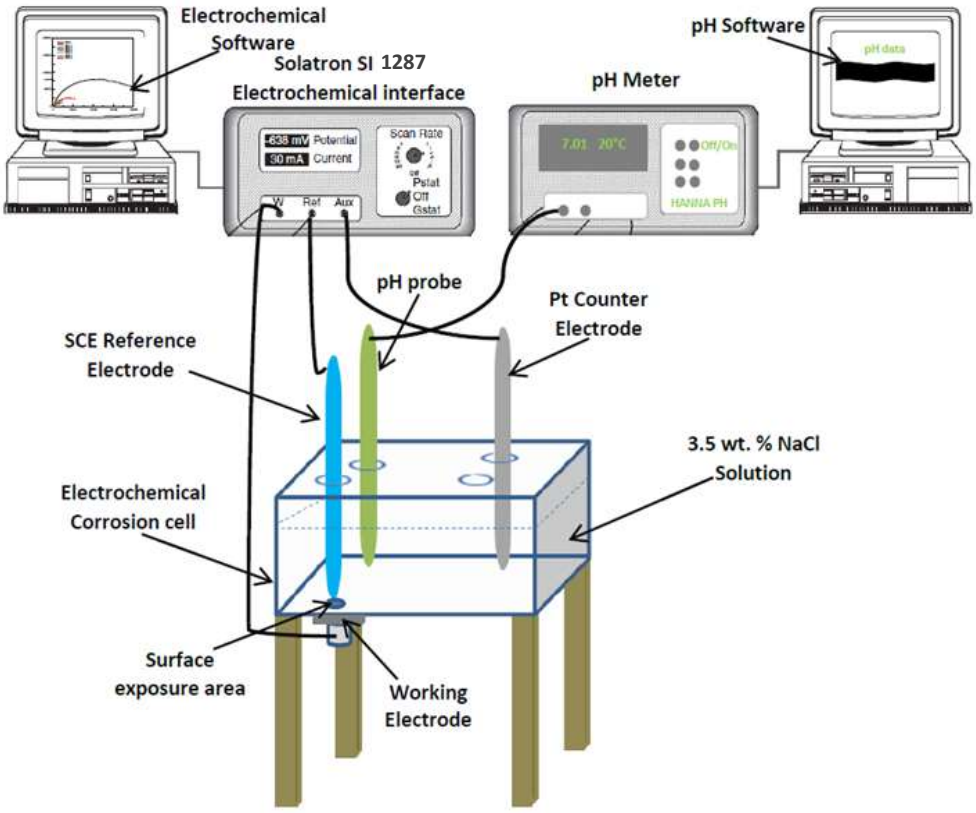

Figure 4.23: Schematic of the experimental set up used during the AC/DC/AC cyclic test [6]

4.4.5.2 AC/DC/AC cyclic test procedure

The open circuit potential (E_{OCP}) of the 15/5 PH steel substrate and all the AlCr(N) coatings was measured prior to the start of the AC/DC/AC cyclic test in order to determine the initial potential of both substrate and coatings and assess any changes in potential with time. The test involved measuring the resting potential of the working electrode (i.e. each test sample) with respect to the SCE reference electrode over a period of two hours. The potential is continuously monitored during this time which enables a plot of the evolution in potential with time to be generated in each case.

The AC/DC/AC cyclic test is started immediately after the end of the two-hour OCP period and takes place over several steps:

I) The initial AC measurement (AC_i) is performed to assess the condition of the sample prior to the start of DC cathodic polarisation. It takes place over 15 minutes and involves applying a 10 mV AC signal on the test sample and recording its response over a large range of frequencies.

II) The DC cathodic polarisation step (DC_n) is then started by applying -1.5V vs. SCE on each test sample for a duration of 20 mins, to induce coating damage.

III) The DC step is followed by a 3-hour relaxation step (OCP_n) during which the OCP of the sample is monitored against the SCE.

IV) Further AC measurements (AC_n) are subsequently performed to re-assess the condition of the coating after each DC cathodic polarisation (and relaxation) step.

'n' represents the number of cycles - which in this case is 6, as steps II to IV were repeated 6 times for each sample over a total test duration of around 24 hours per sample. A schematic diagram of the test procedure is provided in Figure 4.24. The solution pH was measured

throughout the test in order to monitor any changes in pH and evaluate their effect on the corrosion behaviour of the coatings under study.

The 6-cycle test was carried out once on three AlCr(N) coatings with varying Cr content. Ideally a minimum of three repeats is required in order to evaluate the reliability of the technique and ensure that the results provide an accurate assessment of the corrosion performance of the Al-rich coatings. In this instance the test was only performed once due to a shortage of available test area on existing test samples and lack of time to reproduce the coatings on larger samples for corrosion testing. Fortunately it was still possible to obtain some meaningful results regarding the corrosion performance of the coatings from analysing the EIS and pH data collected throughout the test.

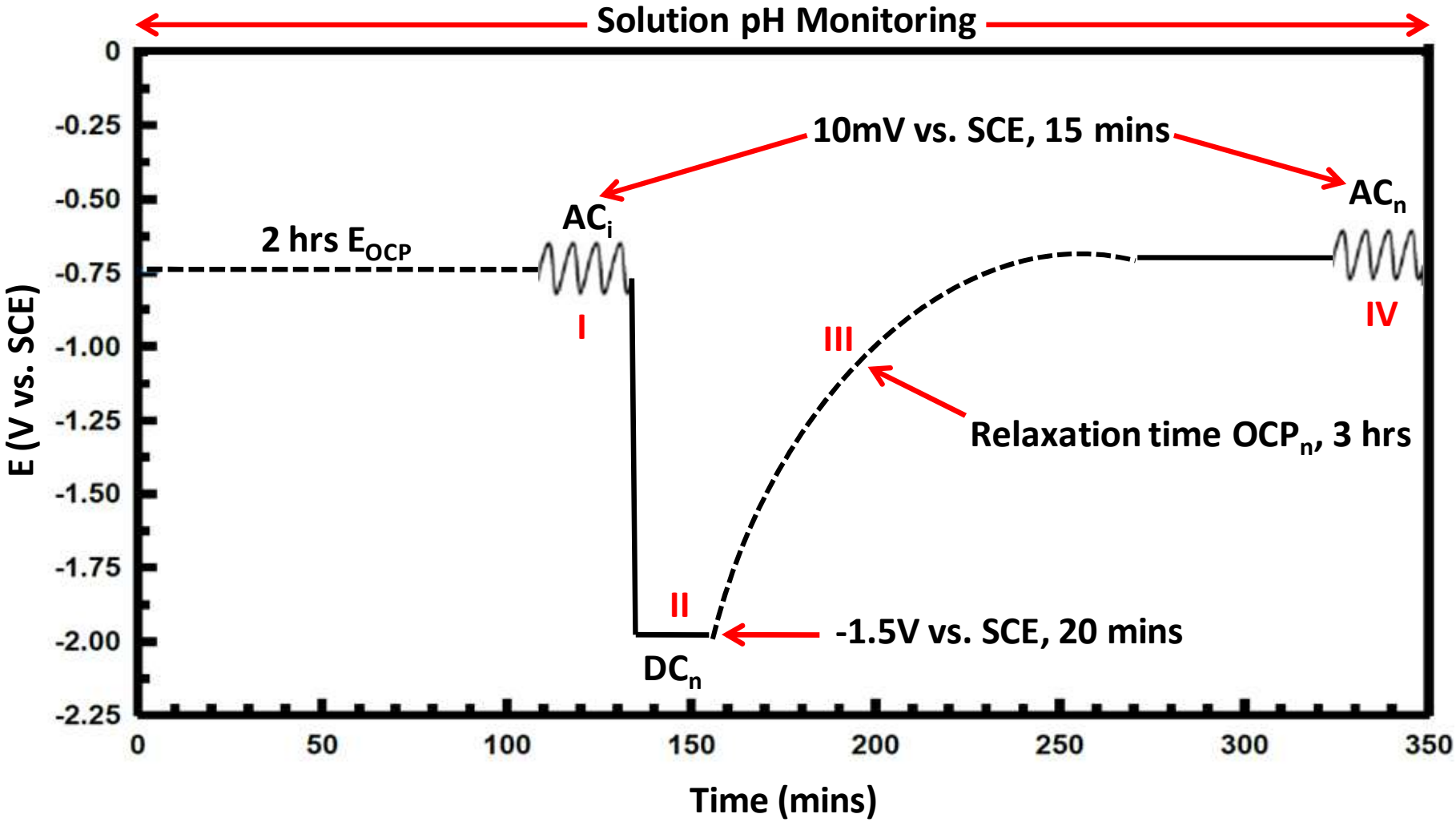

Figure 4.24: Schematic diagram describing the AC/DC/AC cyclic test procedure (modified from [6])

Chapter 5

Evaluation of the properties of PVD AlCr(N) coatings

This chapter describes studies into selected metallic AlCr(N) coatings with varying amounts of chromium (Cr) and nitrogen (N). These were investigated in order to assess the effect of the alloying elements on their structural, mechanical and tribological properties. The Cr content was varied from 4 to 16 at% while the N content was fixed at around 11 at% for the first three coatings and 18 at% for the remaining coating. The corrosion properties of three out of the four AlCr(N) coatings described above, were also examined after subjecting the coatings to the AC/DC/AC electrochemical corrosion test. The selected coatings contained 4, 13 and 16 at% Cr and two different N contents: 11 and 18 at%. In all cases, the percentage of alloying element was kept relatively low (below 20 at %) so as to retain the sacrificial properties exhibited by pure aluminium as a result of its highly electronegative potential. It is worth noting that for the corrosion experiments, the three AlCr(N) coatings were produced on two different stainless steel substrates: while the coatings containing 4 and 16 at% Cr were deposited on 15/5 PH, the one containing 13 at% Cr was applied on 17/4 PH due to the lack of available samples coated with this particular coating on 15/5 PH steel. However, both substrate materials are fairly similar, differing only slightly in terms of their Cr and Ni content as described in Chapter 4. Furthermore, their open circuit potential values were found to be very close so the difference in substrate materials should have very little impact on the corrosion behaviour of the AlCr(N) deposits. A summary of the AlCrN coatings deposited on the two stainless steel substrates and subsequently tested are illustrated in Table 5.1 below.

Table 5.1: Summary of selected AlCrN coatings deposited on two types of stainless steel substrates and tested to assess their structural, mechanical, tribological and corrosion properties

		Structural, mechanical and tribological testing on AlCrN-coated	AC/DC/AC corrosion test on AlCrN-coated	
Coating composition (at%)	**Substrate**	**15/5 PH**	**15/5 PH**	**17/4 PH**
Al-4%Cr-12%N	15/5 PH	✓	✓	x
Al-8%Cr-11%N	15/5 PH	✓	x	x
Al-13%Cr-11%N	15/5 PH & 17/4 PH	✓	x	✓
Al-16%Cr-18%N	15/5 PH	✓	✓	x

Studying this range of compositions will provide useful information regarding the effect of adding different proportions of alloying elements on the properties of the coatings, with a view to enable better coating design which can be tailored to meet the requirements of specific applications.

5.1 Compositional and structural analyses

Compositional analysis was carried out on the surface and cross-section of selected AlCr(N) coatings (Figures 5.1, 5.2, 5.3 and 5.4). On the surface of each coated sample, EDX analysis was performed on three different areas with the results showing that all the coatings are aluminium-rich, differing only in the amount of chromium and nitrogen present. The Cr content was found to be in the range of 4 to 16 at% while around 11 at% nitrogen was recorded for three of the coatings, increasing slightly to 18 at% for the fourth AlCr(N) deposit. Depending on the measured Cr and N content, the selected coatings are referred to by the following designations: Al-4Cr-12N, Al-8Cr-11N, Al-13Cr-11N and Al-16Cr-18N. The gradual increase in the Cr content of the coatings can be clearly seen when comparing the EDX spectra taken at the surface of each coated sample as shown in Figures 5.1 – 5.4

which display a progressive increase in the intensity of the chromium peaks as the Cr content increases. For Al-16Cr-18N, a higher intensity nitrogen peak was recorded due to the increase in the nitrogen content of the coating.

EDX analysis was also carried out on the cross-sections of each coating (Figures 5.1b, 5.2b, 5.3b and 5.4b) in order to check for compositional uniformity. The results confirmed the presence of the three main coating elements (Al, Cr and N) and revealed that, in each case, the elemental composition appears uniform throughout the coating thickness, with only minor fluctuations recorded.

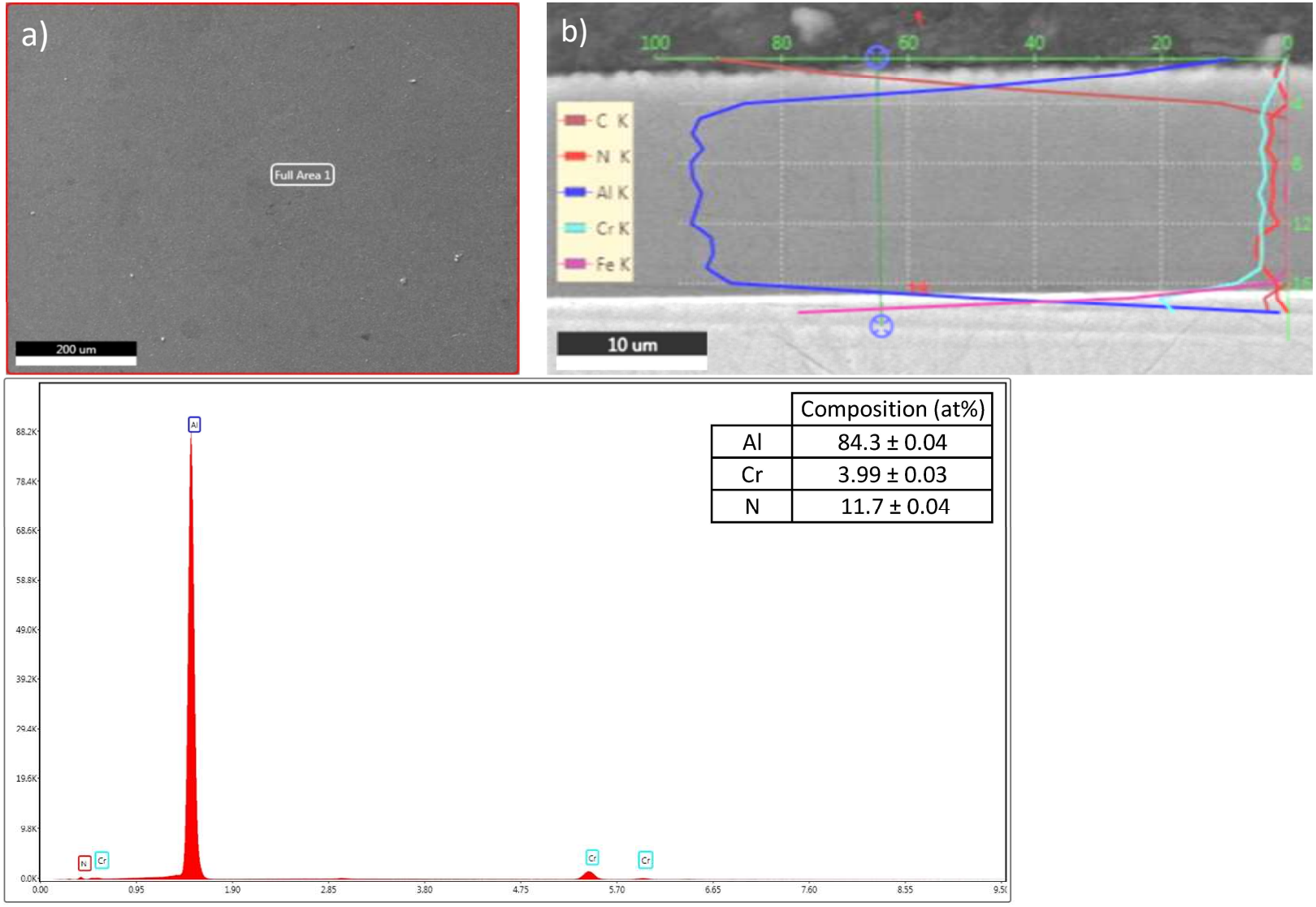

	Composition (at%)
Al	84.3 ± 0.04
Cr	3.99 ± 0.03
N	11.7 ± 0.04

Figure 5.1: Compositional analysis of Al-4Cr-12N deposited on 15/5PH steel at a) the surface and b) the cross-section

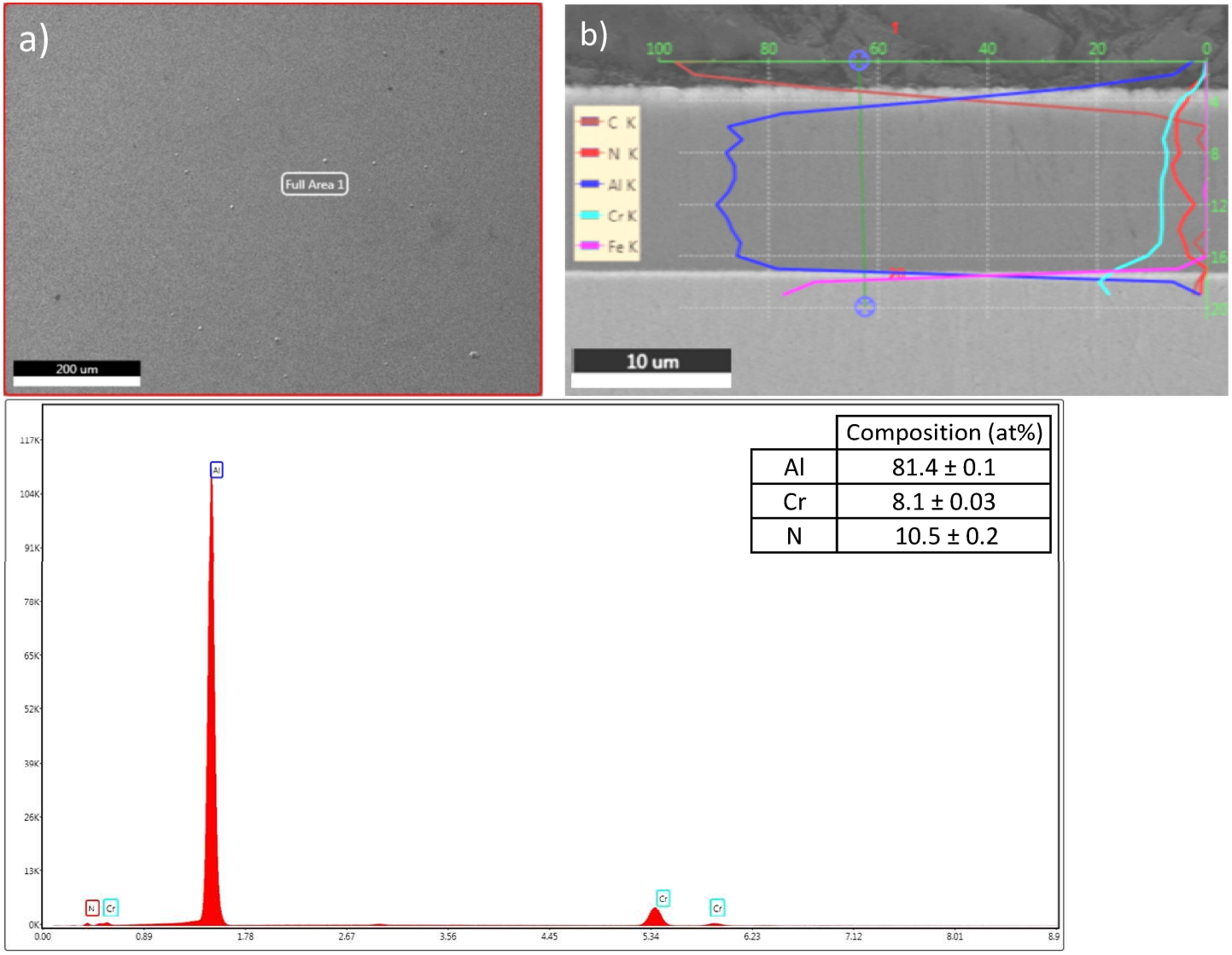

	Composition (at%)
Al	81.4 ± 0.1
Cr	8.1 ± 0.03
N	10.5 ± 0.2

Figure 5.2: Compositional analysis of Al-8Cr-11N deposited on 15/5PH steel at a) the surface and b) the cross-section

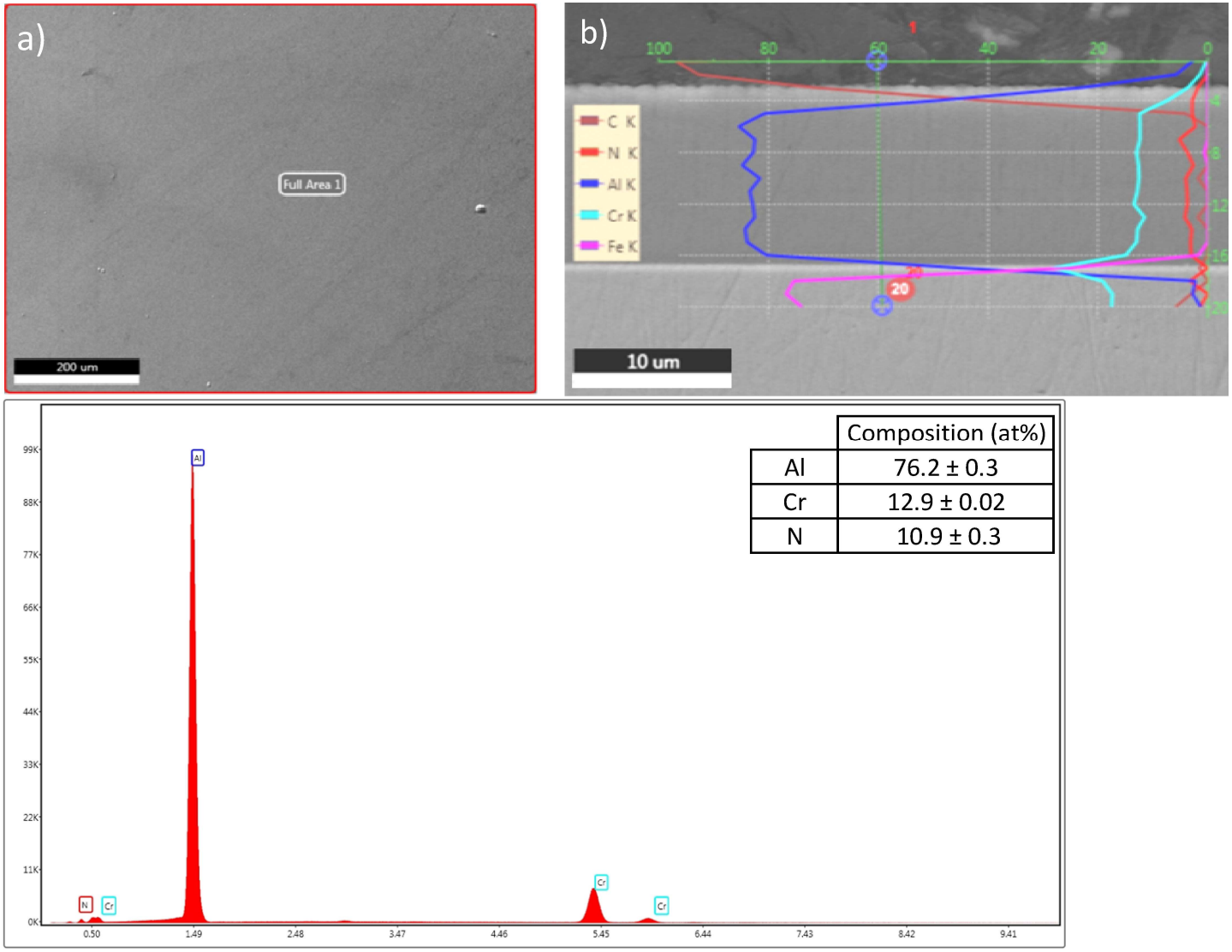

	Composition (at%)
Al	76.2 ± 0.3
Cr	12.9 ± 0.02
N	10.9 ± 0.3

Figure 5.3: Compositional analysis of Al-13Cr-11N deposited on 15/5PH steel at a) the surface and b) the cross-section

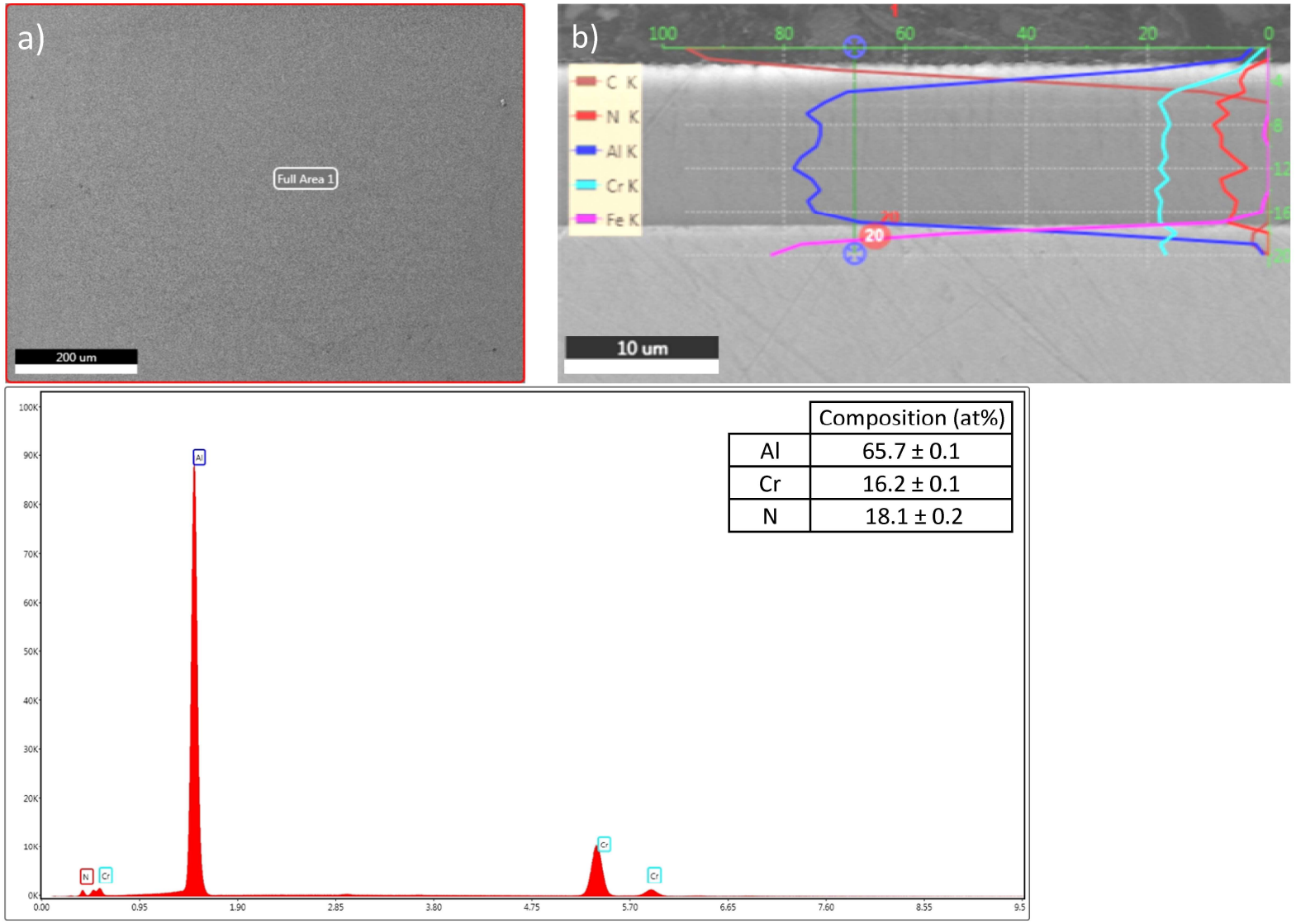

	Composition (at%)
Al	65.7 ± 0.1
Cr	16.2 ± 0.1
N	18.1 ± 0.2

Figure 5.4: Compositional analysis of Al-16Cr-18N deposited on 15/5PH steel at a) the surface and b) the cross-section

SEM characterisation of the coatings' surfaces at high magnification (Figures 5.5 a-d) exposed significant structural difference between the coatings. Indeed it is evident from the topological images that, with increasing Cr content, the coating structure changes, becoming more compact with much smaller columns. This effect is observed when comparing the surface structure of Al-4Cr-12N, Al-8Cr-11N and Al-13Cr-11N. However for Al-16Cr-18N (Figure 5.3d) which has the highest Cr and N content, no further reduction in the size of the columns is observed, instead the columnar structure looks very similar to that of Al-8Cr-11N. Images of the AlCr(N) coating cross-sections (Figures 5.5 e-h) showed that in all cases dense, uniform and well-adhered deposits were produced on the surface of the 15/5 PH steel substrate. Cross-sectional analysis revealed the presence of a very thin Cr interlayer in contact with the substrate and a thick AlCr(N) layer on top. The purpose of the Cr interlayer is to promote better adhesion between the AlCr(N) coating and the underlying substrate. The coatings' thickness was measured in several places along the length of the cross-sections with the results presented as follows:

- Al-4Cr-12N: 15.1 ± 0.05 μm
- Al-8Cr-11N: 14.4 ± 0.04 μm
- Al-13Cr-11N: 14.3 ± 0.1 μm
- Al-16Cr-18N: 11.9 ± 0.04 μm

Thick coatings (with thicknesses above 10 μm) were produced in all cases, which should be beneficial in providing barrier protection to the underlying steel substrate.

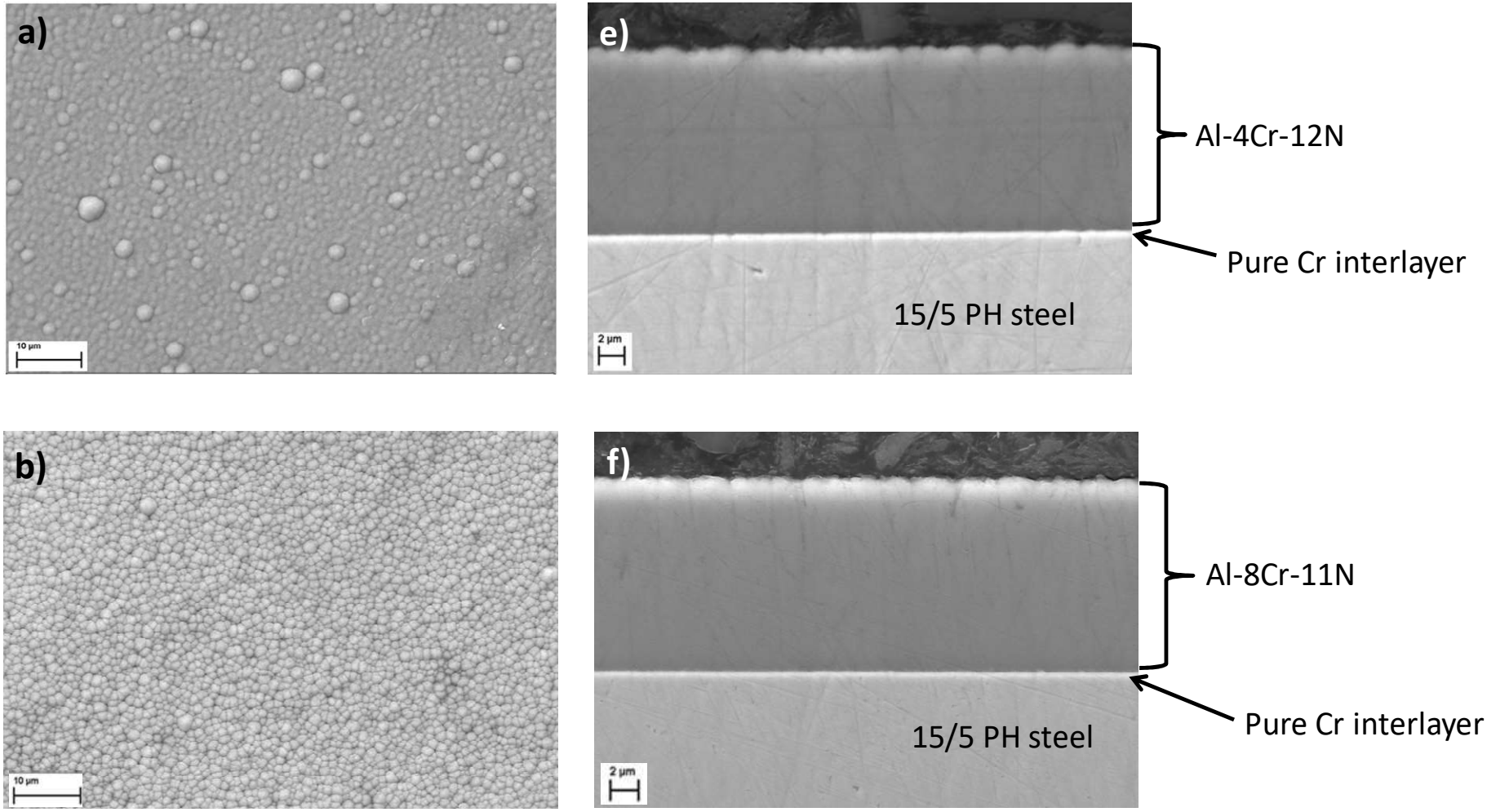
a)
10 µm
e)
2 µm
Al-4Cr-12N
Pure Cr interlayer
15/5 PH steel
b)
10 µm
f)
2 µm
Al-8Cr-11N
Pure Cr interlayer
15/5 PH steel

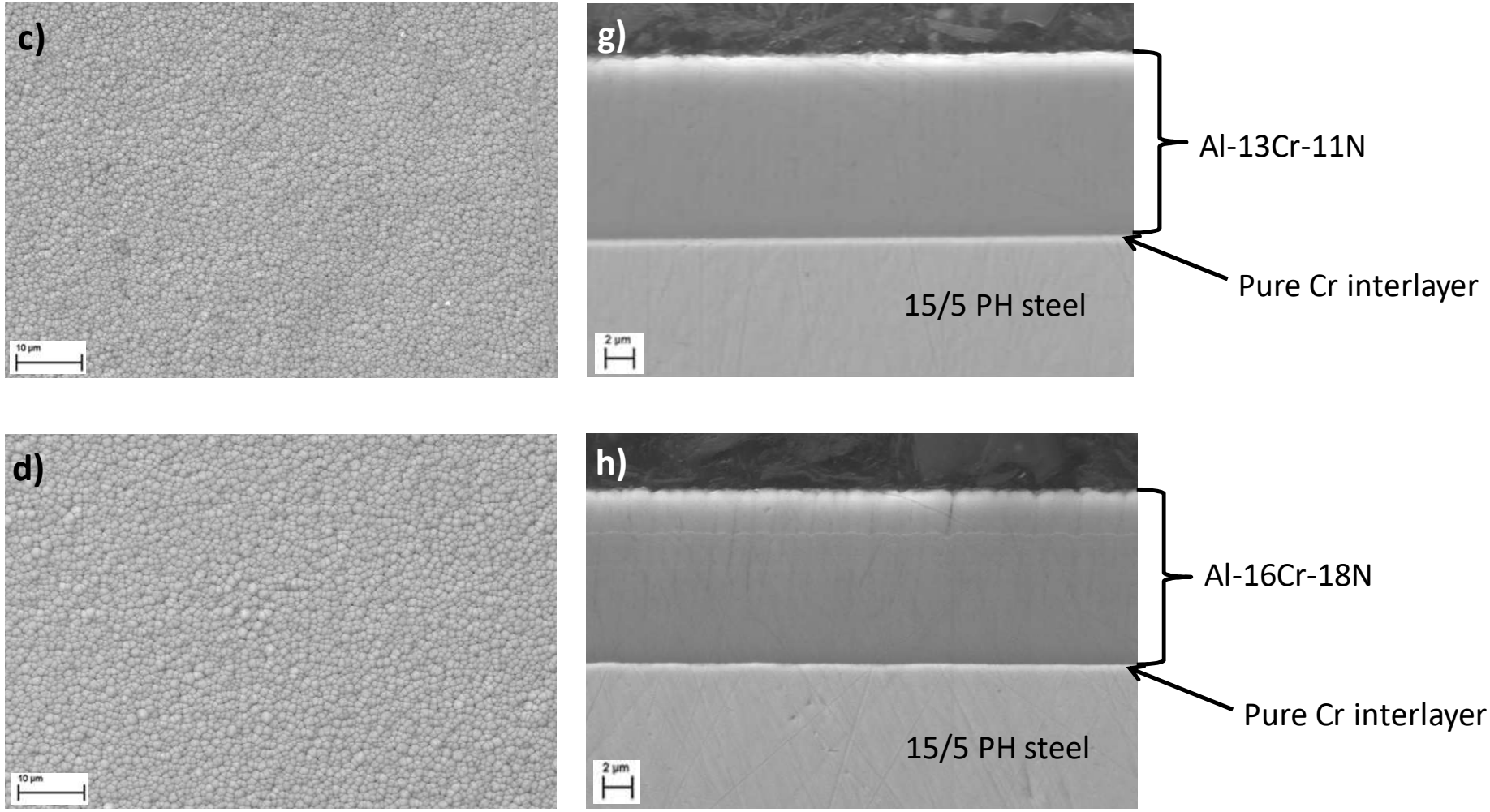

Figure 5.5: SEM micrographs of the surface and cross-sections of Al-4Cr-12N (a & e), Al-8Cr-11N (b & f), Al-13Cr-11N (c & g) and Al-16Cr-18N (d & h)

5.2 Phase composition

X-ray diffraction patterns of the uncoated 15/5 PH substrate and the AlCr(N) coatings are presented in Figure 5.6. For the 15/5 PH steel substrate the X-ray diffraction pattern consists mainly of several Fe-Cr-Ni martensitic (M) peaks at 2θ = 45°, 51°, 65°, 82° and 99° corresponding to the martensite phase structure at different crystallographic orientations and a small γ-Fe peak at 44° diffraction angle indicative of the presence of an austenitic phase.

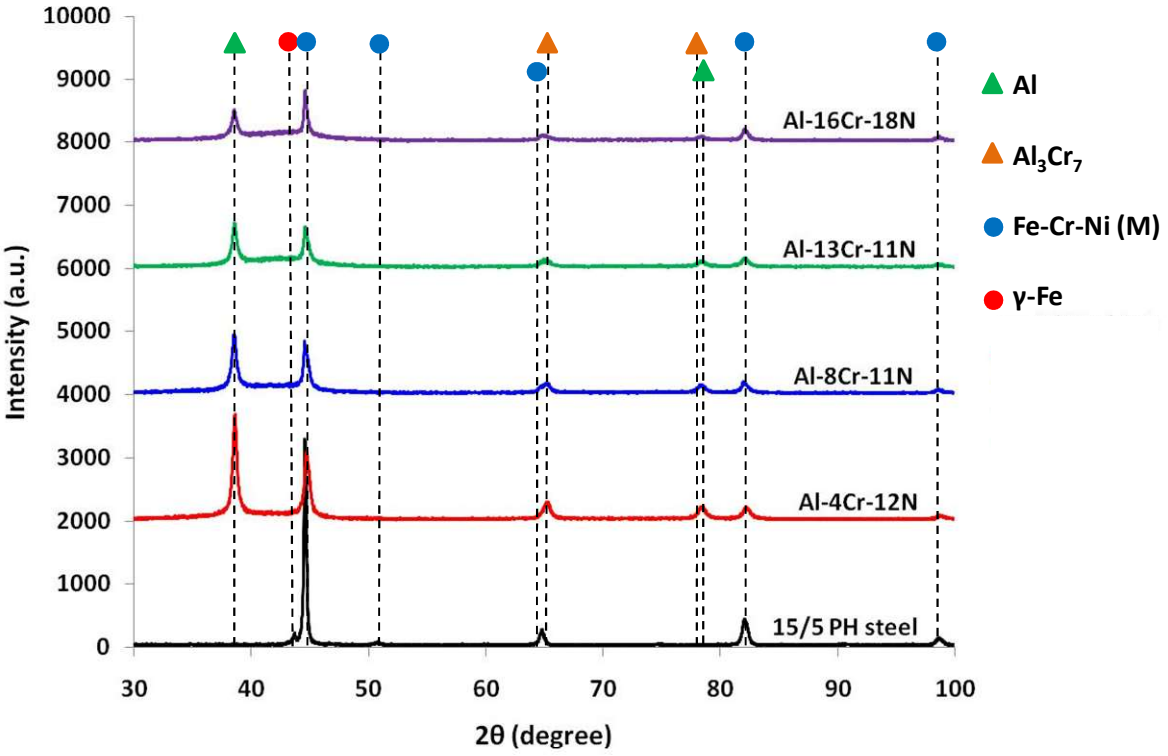

Figure 5.6: X-ray diffraction patterns of the 15/5 PH substrate and AlCr(N) coatings

The martensitic peaks are also visible in the XRD pattern of all the coatings at 2θ = 45°, 82° and 99°. In addition, the diffraction patterns of all the AlCr(N) coatings display two Al peaks at 2θ = 39° and 78.7° corresponding to the supersaturated fcc α-Al solid solution and two low-intensity peaks of the Al_3Cr_7 intermetallic phase at 66° and 78.4° diffraction angles. Although the coatings exhibit identical XRD patterns in terms of the crystalline phases present, the

peak intensities appear to decrease with increasing Cr and N content. This effect could be attributed to the reduction in grain size (grain size refinement) which occurs as the Cr content increases. Sanchette et al. [93] who observed this effect in numerous studies, reported that the greater the difference in atomic radii between Al and any transition metal, the sharper the decrease in the mean grain size as the alloying element content increases, eventually leading to amorphisation of the coating. As the atomic radius of Cr (0.125 nm) is significantly smaller than that of Al (0.143 nm), grain size refinement (as confirmed by the reduction in peak intensity) is more pronounced with increasing Cr content. A similar effect is observed with the addition of nitrogen [93, 159].

It can also be seen from the XRD patterns of the coatings that the intensity of the substrate peak at $2\theta = 45^{o}$ appears to be higher in Al-4Cr-12N compared to all the other AlCr(N) deposits of similar thicknesses, seemingly decreasing in intensity with increasing Cr content, except for Al-16Cr-18N where the substrate peak intensity is very similar to that of Al-8Cr-11N. As X-rays penetrate significantly deeper into pure Al than pure Cr (confirmed by data obtained from the AbsorbDX X-ray penetration depth software presented in Table 5.2), the diffracted X-ray signal is therefore significantly attenuated in Cr-rich coatings which probably explains the lower intensity substrate peaks observed in the XRD trace of the coatings with a higher Cr content.

Table 5.2: Penetration depth at 95% signal of Cu-Kα X-rays in Al and Cr

	Penetration Depth (μm)	
Element	$2\theta = 30^{o}$	$2\theta = 90^{o}$
Al	29.1	79.6
Cr	2.2	6

5.3 Mechanical properties of as-deposited AlCr(N) coatings

The mechanical properties of all four AlCr(N) coatings were evaluated using a Fischerscope instrumented Vickers ultra-microindentation tester to carry out hardness and modulus measurements. The results indicate that both hardness and modulus increase with increasing chromium and nitrogen content in the coating (Figure 5.7).

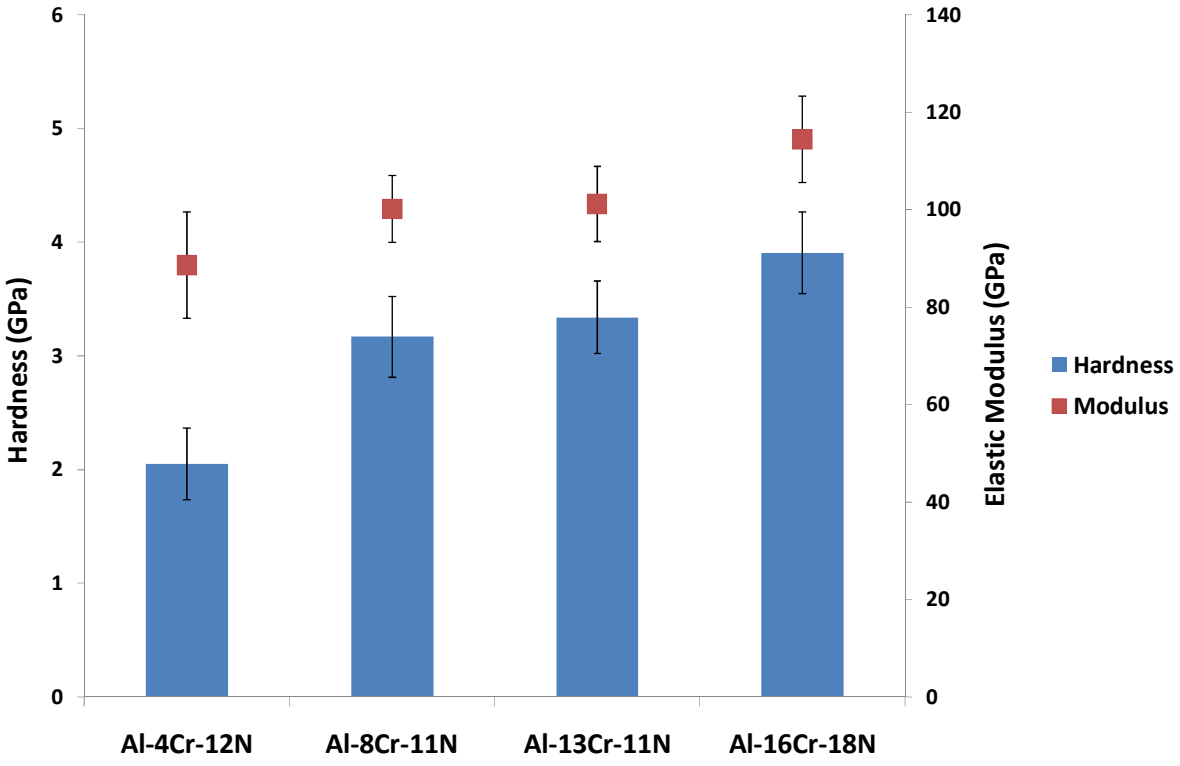

Figure 5.7: Hardness and elastic modulus of AlCr(N) coatings

The hardness of Al-4Cr-12N was measured at 2 GPa increasing to around 3.2 GPa as the Cr content doubles. Further increase in the chromium and nitrogen content leads to a noticeable increase in hardness with maximum hardness values of 3.9 GPa recorded for Al-16Cr-18N.

These values are much higher than those measured for a pure Al coating (0.8 GPa) and an AlCr coating containing 10 at% Cr but no nitrogen (~ 2 GPa) - confirming the benefit of using alloying elements for improving the mechanical properties of pure Al metallic films.

The elastic modulus displays a similar trend, increasing moderately, from 89 to 100 GPa, as the Cr content increases from 4 to 8 at%. A small increase is subsequently observed as the Cr content reaches 13 at% followed by a more noticeable increase in elastic modulus with values approaching 114 GPa recorded for Al-16Cr-18N. These values therefore lie within the range of the elastic modulus of Al (typically 72 GPa) and that of Cr (around 280 GPa) - though much closer to the modulus of pure Al due to the presence in all the AlCr(N) coatings of an aluminium-rich crystalline matrix as confirmed by the XRD data in Figure 5.4. The reported improvement in mechanical properties can be explained by changes in the coating structure occurring with increasing chromium and nitrogen content, resulting in the formation of a much finer grain structure as described in section 5.2. This observed hardening effect with increasing Cr content in Al-rich coatings was reported by Sanchette [95] who attributed it to a combination of solid solution and grain size refinement. The more compact coating structure formed with increasing alloying element content has an effect on the measured open circuit potential of the coating as described in section 5.6.

5.4 Wear behaviour of as-deposited AlCr(N) coatings

Micro-abrasion wear testing of the AlCr(N) coatings was carried out in order to evaluate their wear properties. The results, which show the wear rate of the coatings at two different sliding distances (2.4 m and 3.9 m), are presented in Figure 5.8. The wear rate of a nitrogen-free AlCr coating containing 10 at% Cr (referred to as Al-10Cr) was included for comparison purposes. It is clear from the wear data that there is a strong correlation between wear rate

and hardness as the wear rate appears to decrease with increasing chromium and nitrogen content in the coating (hence increasing hardness). When looking at the AlCr(N) coatings, the highest and lowest wear rate values were measured for Al-4Cr-12N and Al-16Cr-18N, respectively. It can be noted that for each AlCr(N) coating, the wear rate values recorded at 2.4 and 3.9 m sliding distances appear to be very similar (within the statistical error).

Comparing the wear rate of the AlCr(N) coatings to that of Al-10Cr which does not contain any nitrogen, it is clear that the latter exhibits the highest wear rate – higher even than the wear rate of Al-4Cr-12N and that of Al-8Cr-11N which has a similar chromium content. This highlights the beneficial effect of nitrogen addition in improving the tribological properties of the coatings.

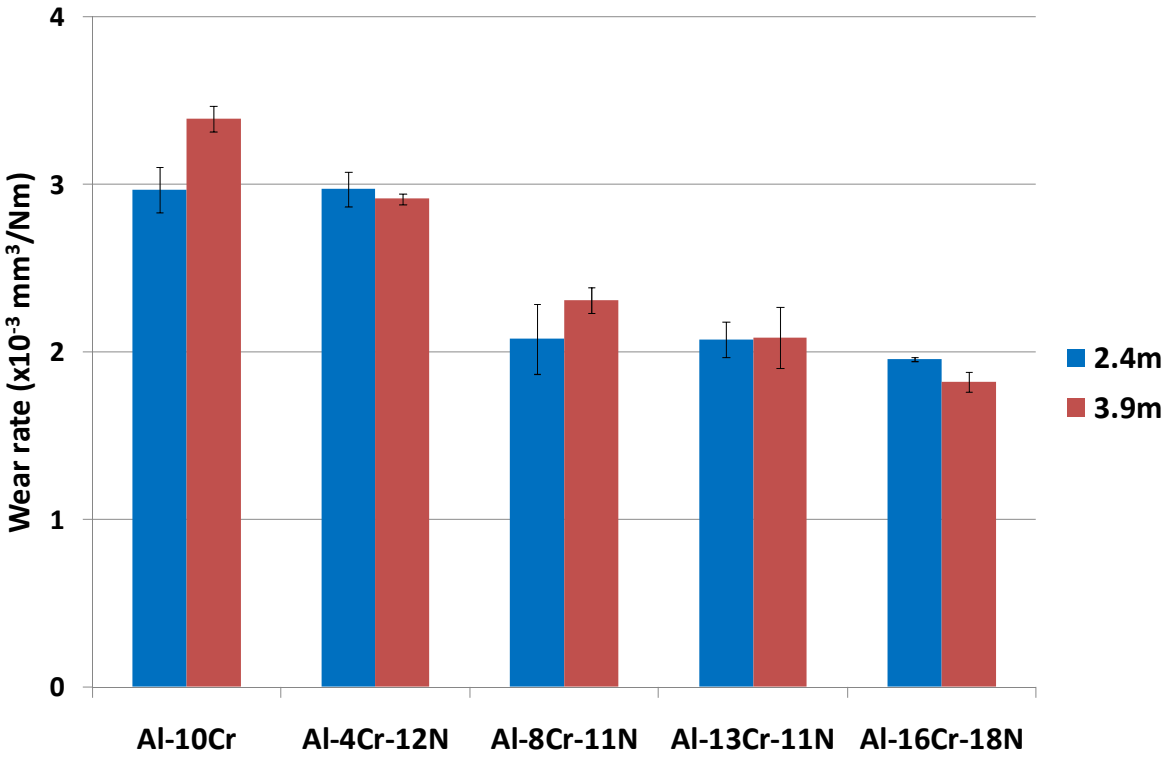

Figure 5.8: Wear rate of AlCr(N) coatings

The overall wear rate of the AlCr(N) coatings is fairly high, ranging between 1.8 x 10^{-3} and 3 x 10^{-3} mm^3/Nm. Depending on the application, a metallic coating with lower wear rates might be more desirable. A recent study by Lawal et al. [160] has shown that it is possible to increase the abrasive wear resistance of metallic Al-based coatings by adding such elements as nickel, titanium, silicon, boron and nitrogen to the aluminium matrix. Indeed the research showed that nanostructured/amorphous AlNiTiSiB(N) coatings exhibit much improved abrasive wear properties displaying in some instances (depending on the coating composition) wear rates comparable to those of a ceramic CrN coating.

Wear depth profiles of the AlCr(N) coatings were obtained at both sliding distances. Although each test was repeated three times, the depth profiles presented in Figure 5.9 are those of the second repeat, shown as an example with the first and third repeats exhibiting similar results. The wear depth profile of Al-10Cr was also included for comparison.

It is clear from the depth profiles that the maximum crater depth is around 5.5 μm which indicates that the micro-abrasion tests carried out at 2.4 m and 3.9m sliding distances did not cause coating perforation as all the coatings (including Al-10Cr) are above 10 μm in thickness, enabling accurate evaluation of the abrasive wear performance of the coatings with negligible influence from the steel substrate. At both sliding distances, the depth of the crater varies depending on the proportion of alloying element in the coating. Indeed the higher the chromium and nitrogen content, the shallower the crater. Although this effect is observed at both sliding distances, Al-4Cr-12N, Al-8Cr-11N and Al-13Cr-11N appear to have very similar depth profiles at 3.9 m sliding distance (Figure 5.7b), making it difficult to discriminate between them. It might be useful to repeat the test at a shorter sliding distance than 3.9m (or with a less aggressive abrasion medium – e.g. Al_2O_3) and observe any changes in the depth profiles of the coatings.

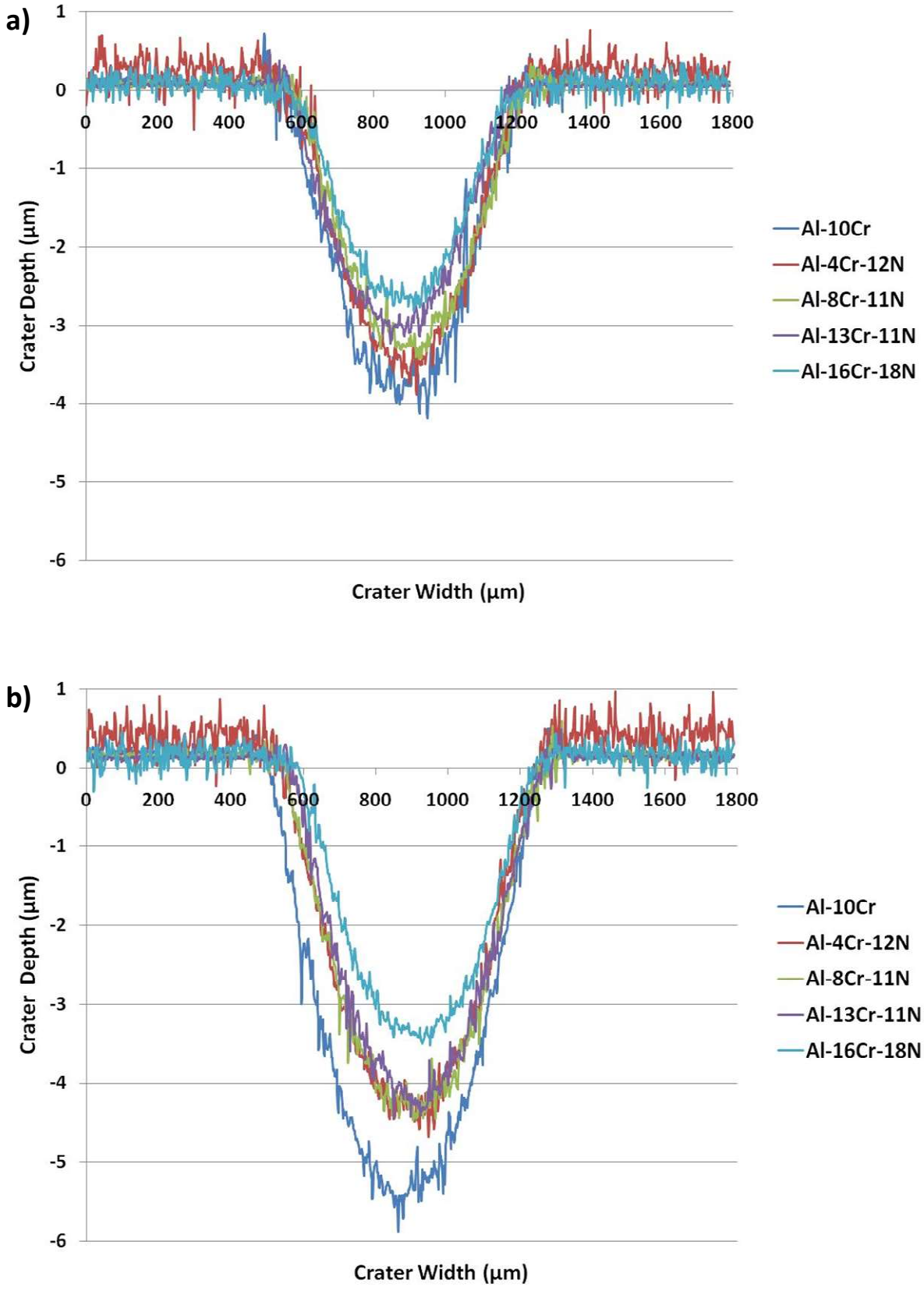

Figure 5.9: Micro-abrasion crater depth profiles of AlCr(N) coatings at a) 2.4m and b) 3.9 m sliding distance

5.5 Surface morphology of the corroded areas

The corroded areas of Al-4Cr-12N, Al-13Cr-11N and Al-16Cr-18N were observed under the SEM and compositional analysis was carried out to determine the corrosion products after six successive DC/OCP cycles.

For Al-4Cr-12N, two areas were selected for close inspection as shown in Figure 5.10. Compositional analysis of the selected areas revealed that the coating is still present on the surface of the sample after the AC/DC/AC cyclic test with no detectable sign of the substrate (i.e. negligible content of Fe, Ni and Cu). Al, Cr and N can be found in both areas, although in different proportions. Oxygen is also present is both areas as shown by the high intensity peak detected at 0.525 keV, which suggests the presence of an oxide layer. The aluminium content is significantly higher in area 2 compared to area 1, indicating that the oxide layer is thinner in area 2 which therefore allows more sampling of the coating lying underneath. The oxide film is probably a mixture of a Cr oxide layer (formed from the Cr in the substrate which became partially exposed during the first DC/OCP cycle as later confirmed by the electrochemical results) and an Al oxide layer formed as a result of partial coating dissolution. The oxide film was found to grow thicker with each subsequent DC/OCP cycle - protecting the coating from further damage.

For Al-13Cr-11N, three main areas were selected for analysis, as shown in Figure 5.11. The SEM micrograph appears to show that coating delamination has occurred with layers of coating being removed. Subsequent EDX analysis of the selected areas confirmed that the substrate has been exposed in areas 2 and 3, as indicated by the presence of Fe in area 2 and Fe, Ni and Cu in area 3. Although the coating is still present in area 1 (no substrate peaks detected), the high chromium and oxygen content measured suggests the presence of an oxide layer (probably Cr_2O_3) on the surface. Coating dissolution has clearly occurred, as indicated by the significant reduction in the Al content measured (15 at% Al compared to 76 at% in the

undamaged coating). The EDX data shows that the Cr oxide layer is also present in area 2 and area 3, probably formed from the Cr in both coating and substrate. As mentioned above, area 3 consists mainly of the steel substrate covered by an oxide layer, although some traces of coating remain, as confirmed by the small amount of Al detected.

The corroded surface of Al-16Cr-18N looks very similar to that of Al-13Cr-11N. For this coating, three main areas were also selected for investigation as pictured in Figure 5.12. No substrate peaks are visible in area 1, which seems to contain small amount of aluminium and nitrogen from the remaining coating and high levels of chromium and oxygen - indicative of the presence of a Cr oxide layer on the surface. In area 2 the proportions of Al, Cr and N have significantly decreased, which suggests that the coating has been severely damaged. As the coating is removed, more of the substrate is sampled during analysis, as confirmed by the visible substrate peaks of Fe, Ni and Cu. The oxygen content is still high, which indicates the presence of an oxide film – probably a Cr oxide layer from the Cr in the substrate material. Most of the coating has been removed in area 3, with EDX data showing mainly substrate peaks and very little Al and N. the Cr content remains high due to the high amount of Cr in the substrate. A very thin Cr oxide layer has also formed on the substrate surface, as indicated by the small amount of oxygen detected.

From the EDX analysis carried out on the corroded areas of the three AlCr(N) coatings after the AC/DC/AC cyclic test, it is clear that severe coating damage has occurred for the coatings with the highest amount of Cr (i.e. Al-13Cr-11N and Al-16Cr-18N) whereas for Al-4Cr-12N a stable protective oxide film was generated on the coating surface protecting it from further damage.

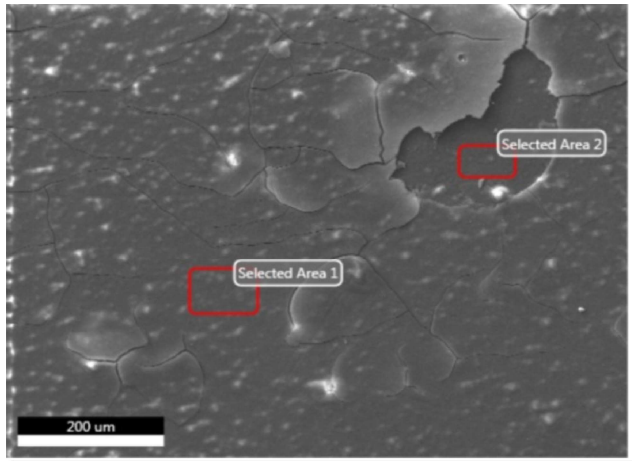

	Composition (at%)	
	Area 1	Area 2
Al	15.56	36.68
Cr	8.98	5.75
N	1.47	1.89
Na	1.90	0.81
Cl	2.11	1.14
O	59.50	48.50
Fe	0.14	0.12
Ni	0.03	0.03
Cu	0.02	0.03
C	10.28	5.07

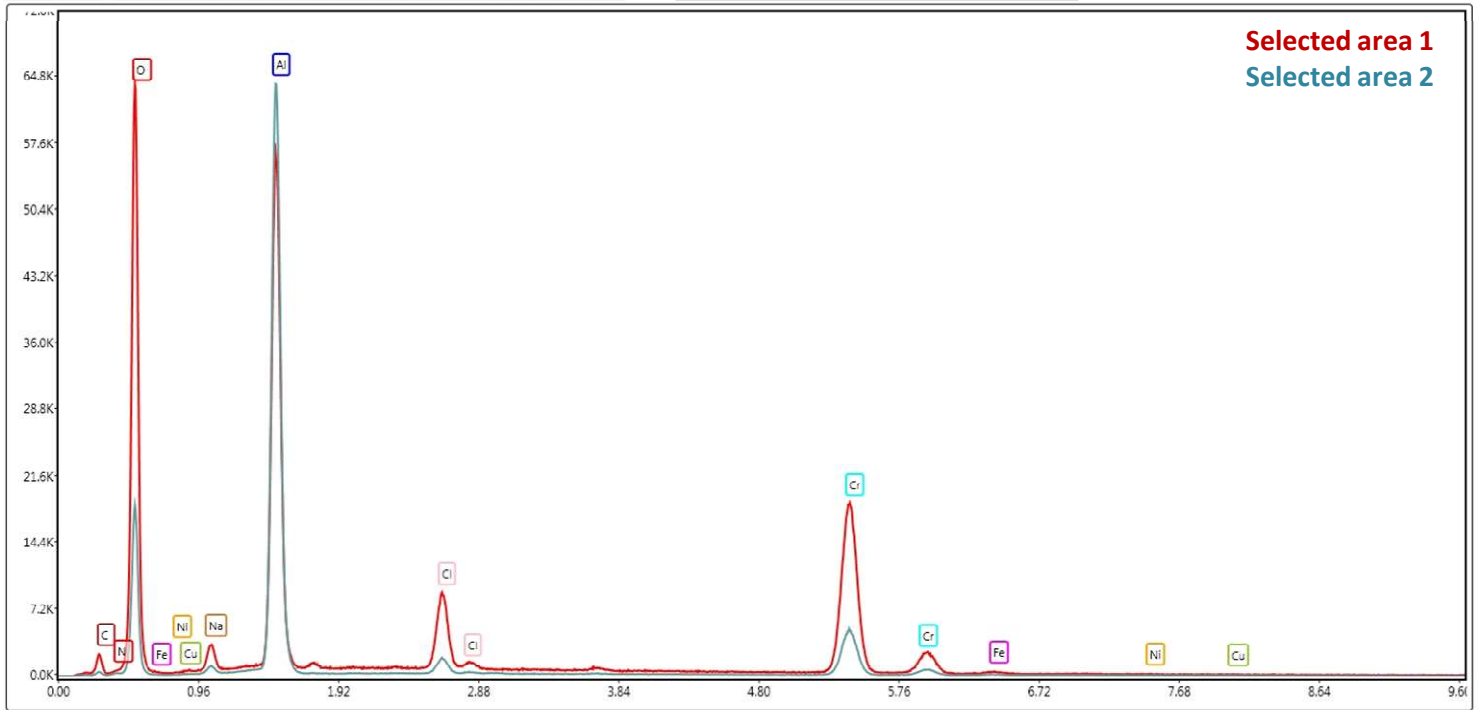

Figure 5.10: SEM micrograph and EDX spectrum analysis of the corroded area of Al-4Cr-12N after six DC/OCP cycles

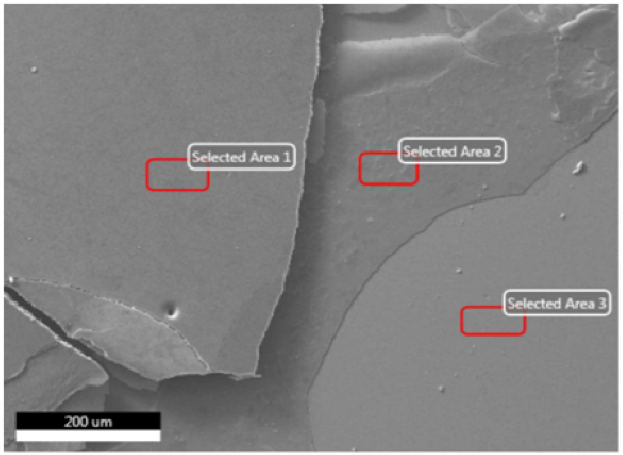

	Composition (at%)		
	Area 1	Area 2	Area 3
Al	15.15	14.33	9.87
Cr	22.53	25.49	28.85
N	8.33	7.05	3.71
Na	3.61	2.22	1.22
Cl	1.02	1.32	0.22
O	44.57	36.42	19.71
Fe	0.14	8.06	27.45
Ni	0.03	0.39	1.60
Cu	0.03	0.26	1.16
C	4.60	4.47	6.22

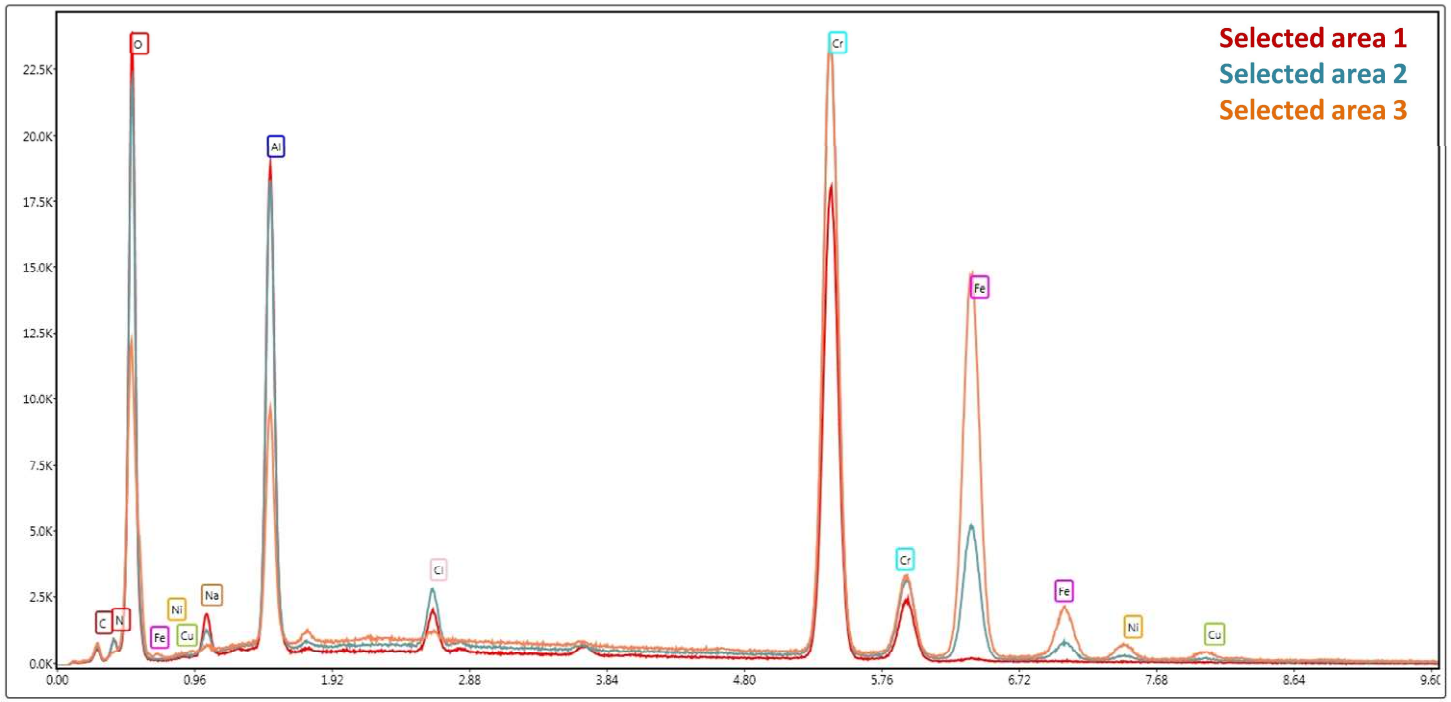

Figure 5.11: SEM micrograph and EDX spectrum analysis of the corroded area of Al-13Cr-11N after six DC/OCP cycles

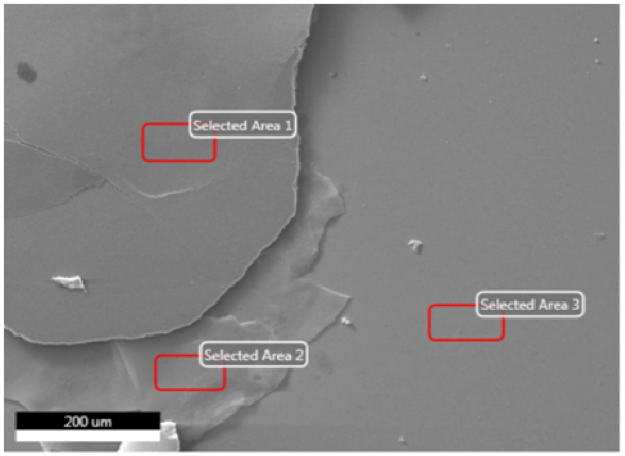

	Composition (at%)		
	Area 1	Area 2	Area 3
Al	8.42	5.65	1.67
Cr	27.62	14.02	14.56
N	12.05	7.79	3.92
Na	3.51	2.67	0.47
Cl	1.48	0.29	0.02
O	42.64	35.25	8.71
Fe	0.27	24.88	60.52
Ni	0.05	1.40	3.43
Cu	0.05	0.87	2.24
C	3.91	7.19	4.46

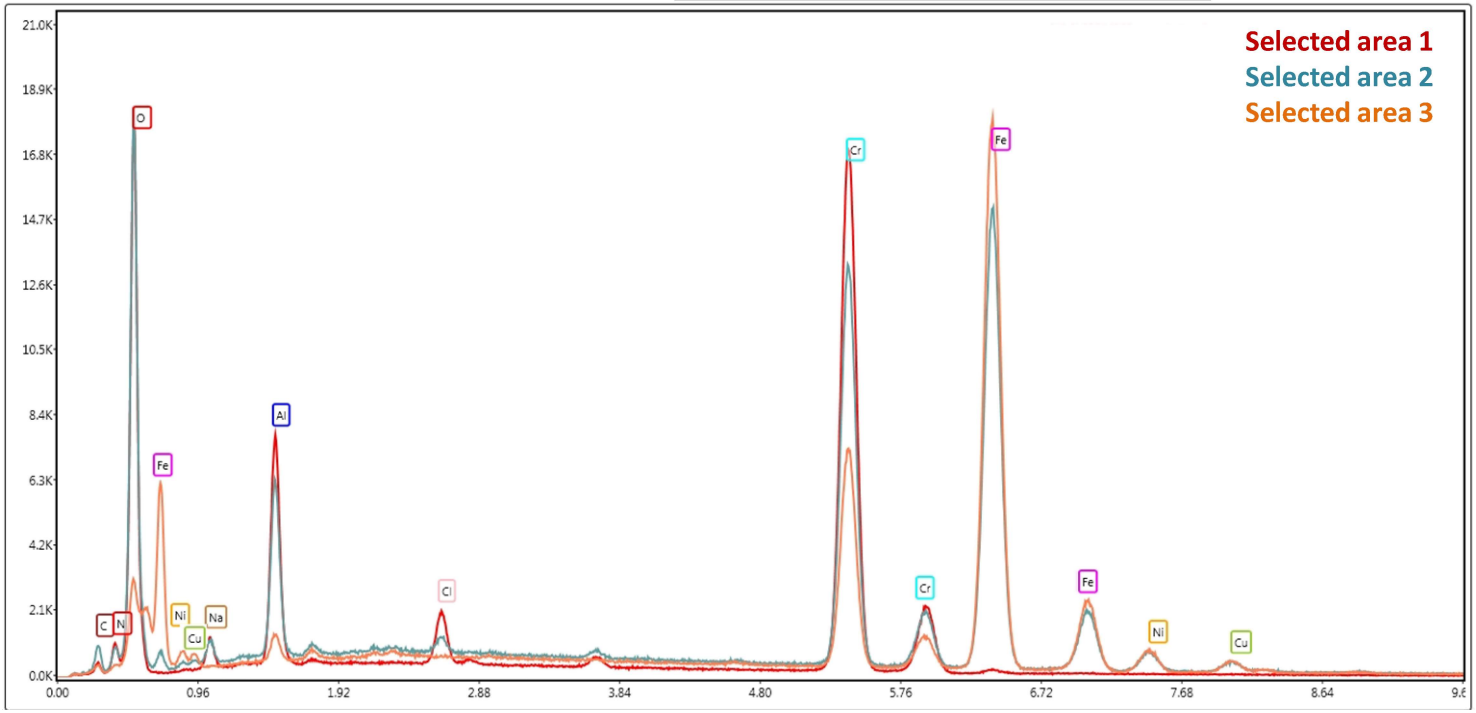

Figure 5.12: SEM micrograph and EDX spectrum analysis of the corroded area of Al-16Cr-18N after six DC/OCP cycles

Visual observation of the corroded areas of all three AlCr(N) coatings was performed immediately after the end of the test, with pictures taken while the samples were still immersed in the electrochemical cell (Figure 5.13). It can be seen from the images that disbanded coating debris is present on the surface of Al-13Cr-11N and Al-16Cr-8N, caused by significant coating degradation occurring during the test (as confirmed by EDX analysis in Figures 5.11 and 5.12). The debris generated appears to be significantly bigger in size for Al-16Cr-18N compared to Al-13Cr-11. In contrast there is a noticeable absence of any corrosion products on the surface of Al-4Cr-12N, which has been protected from corrosion damage by a highly stable passive film, as revealed in Figure 5.10.

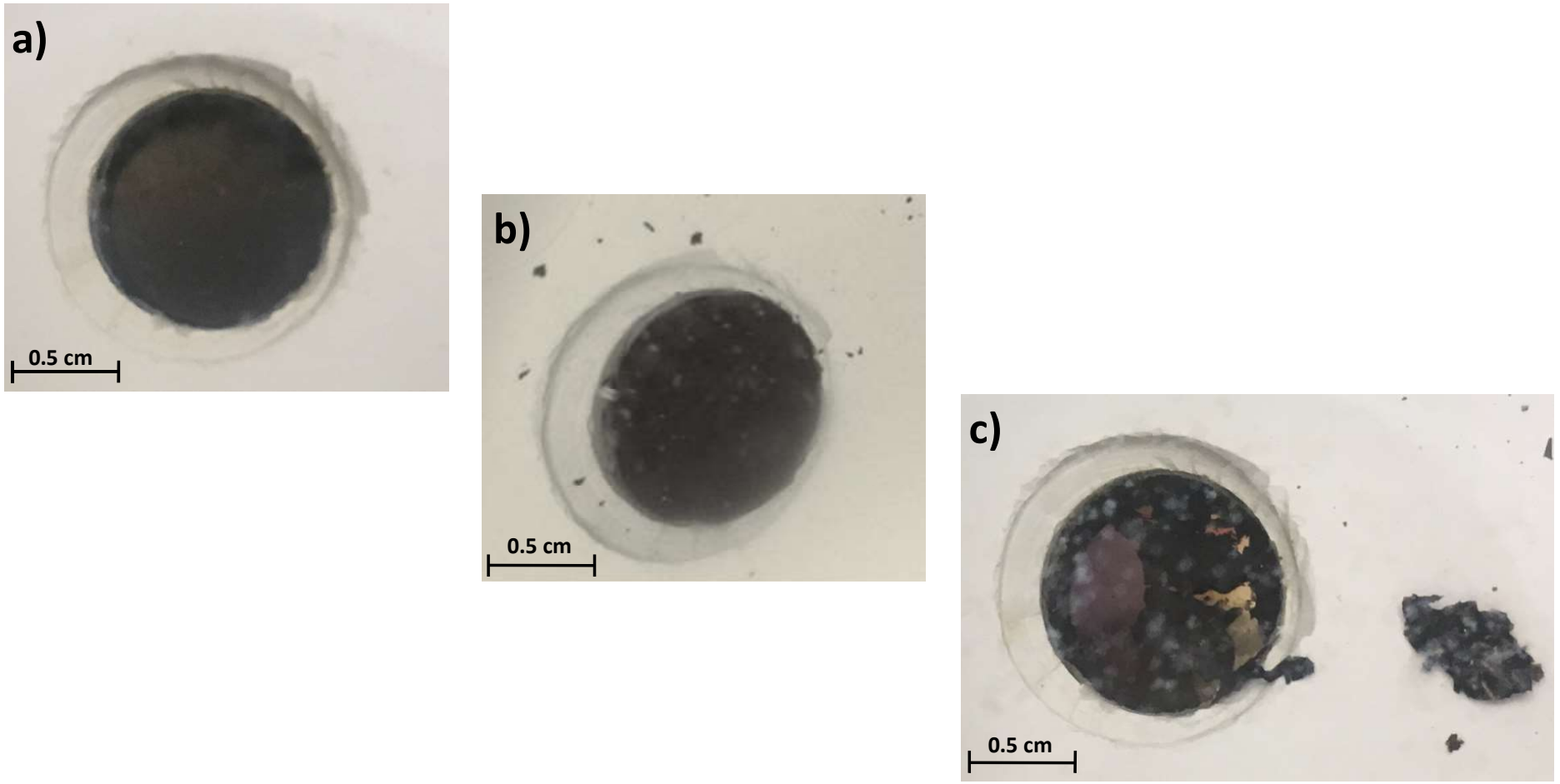

Figure 5.13: Visual observation of a) Al-4Cr-12N, b) Al-13Cr-11N and c) Al-16Cr-18N in the electrochemical cell after six consecutive DC/OCP cycles

5.6 Electrochemical evaluation of the corrosion performance of AlCr(N) coatings

5.6.1 Initial OCP (E_{OCP})

The initial open circuit potential (E_{OCP}) of the substrate and the three AlCr(N) coatings was measured against a saturated calomel electrode (SCE) over a two-hour period, prior to starting the AC/DC/AC cyclic test. The results of the E_{OCP} data recorded throughout the test are presented in Figure 5.14, together with the final OCP values for each sample at the end of the two hours.

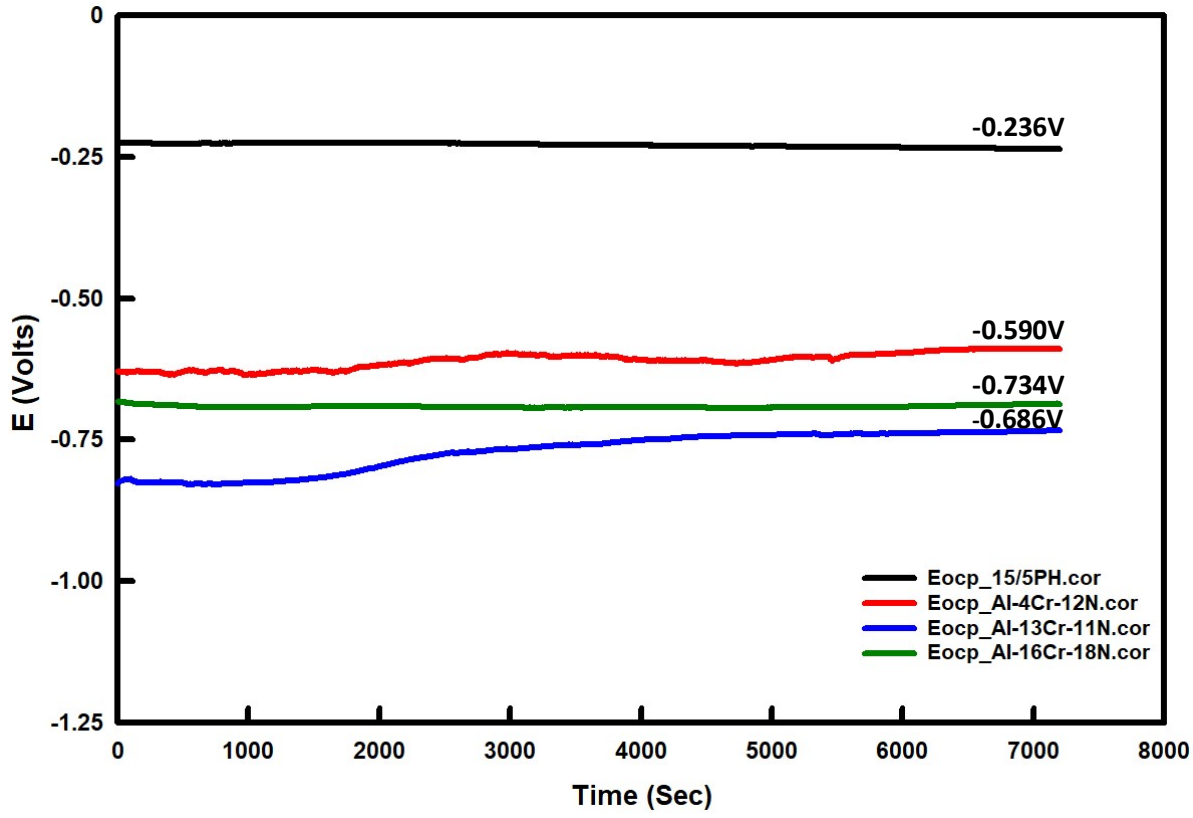

Figure 5.14: Initial OCP (E_{OCP}) of PVD AlCr(N) coatings and uncoated 15/5 PH substrate

The results show that the potentials of all the AlCr(N) coatings are electronegative with respect to the 15/5 PH steel substrate which indicates that the coatings are able to provide

sacrificial protection to the underlying steel substrate. As previously mentioned, Al-13Cr-11N was deposited on a 17/4 PH substrate, whose OCP was measured to be -0.292V after two hours of immersion, confirming that the two substrates have quite similar initial potentials. When comparing the OCP of the coatings, it is clear that Al-13Cr-11N and Al-16Cr-18N exhibit very similar potentials with measured OCP values found to be more electronegative than those of Al-4Cr-12N. This is surprising, given that the potential of Cr (-0.385 V/SCE) is more noble than that of Al (-1.072 V/SCE) [94]; any Cr addition is expected to push the overall coating potential in the positive direction. The fact that the AlCr(N) coatings with the higher Cr content have a more electronegative potential than that of Al-4Cr-12N could be due to several reasons:

1) According to Walsh et al [161], "the corrosion potential of porous deposits on a metal surface varies between the potential of the coating and the substrate". Since Al-4Cr-12N is probably more porous than the other two coatings due to its lower chromium and nitrogen content, its OCP is therefore significantly influenced by the 15/5PH substrate's OCP which being more noble, brings the overall coating potential towards more positive values. In contrast, Al-13Cr-11N and Al-16Cr-18N are probably less porous with a more tightly-packed structure (as a result of increasing alloying element content), which has the effect of reducing the influence of the substrate's OCP on the actual coating's OCP, hence leading to a more electronegative potential.
2) Another factor which could influence the OCP is the coating structure, more precisely the type and proportions of intermetallic phases present. For example, the presence in the coating of Al-rich intermetallic phases (e.g. $Al_{80}Cr_{20}$) would 'trapped' a significant amount of Al atoms leaving the coating matrix rich in Cr (and deficient in Al). As the potential of Cr is more electropositive (-0.385 V/SCE) than that of Al (-1.072 V/SCE), this would have the effect of pushing the overall coating potential in

the positive direction. The opposite effect would therefore be observed in the presence of Cr-rich intermetallics. For the three AlCr(N) coatings under investigation, the Al_3Cr_7 intermetallic phase was identified from the XRD data presented in Figure 5.6 which, from the above reasoning should have led to Al-4Cr-12N being more electronegative than the other two coatings. However this effect was not observed probably due to the low amount of Al_3Cr_7 intermetallics present (i.e. low intensity peaks at $2\theta = 66^o$ and 78.4^o) in all the AlCr(N) coatings.

3) The different composition/thickness of the coating surface passive film (i.e. the native oxide film) could also influence the measured coating OCP.
4) The pure Cr adhesion-promoting layer applied on the substrate prior to depositing the AlCr(N) coatings (as seen in Figures 5.5 e-h) could also affect the overall measured potential, more likely forcing it in the positive direction for (the less dense) Al-4Cr-12N due to the potential of the Cr interlayer also being comparatively noble.

Although their OCP values are fairly close, Al-16Cr-18N appears to have a slightly more electropositive potential (-0.734 V) compared to that of Al-13Cr-11N (-0.686 V) which suggests that increasing the chromium and nitrogen content does lead to ennoblement of the potential as reported in several studies [94, 95].

5.6.2 Evolution of the OCP after six DC/OCP cycles

During the six-cycle test, each cathodic polarisation step was immediately followed by a relaxation stage during which the OCP of the selected AlCr(N) coatings was monitored for a period of three hours. The evolution of the OCP for Al-4Cr-12N, Al-13Cr-11N and Al-16Cr-18N is presented in Figure 5.15. The initial OCP (E_{OCP}) of the 15/5PH steel substrate and those of the three AlCr(N) coatings prior to starting the test are included for comparison.

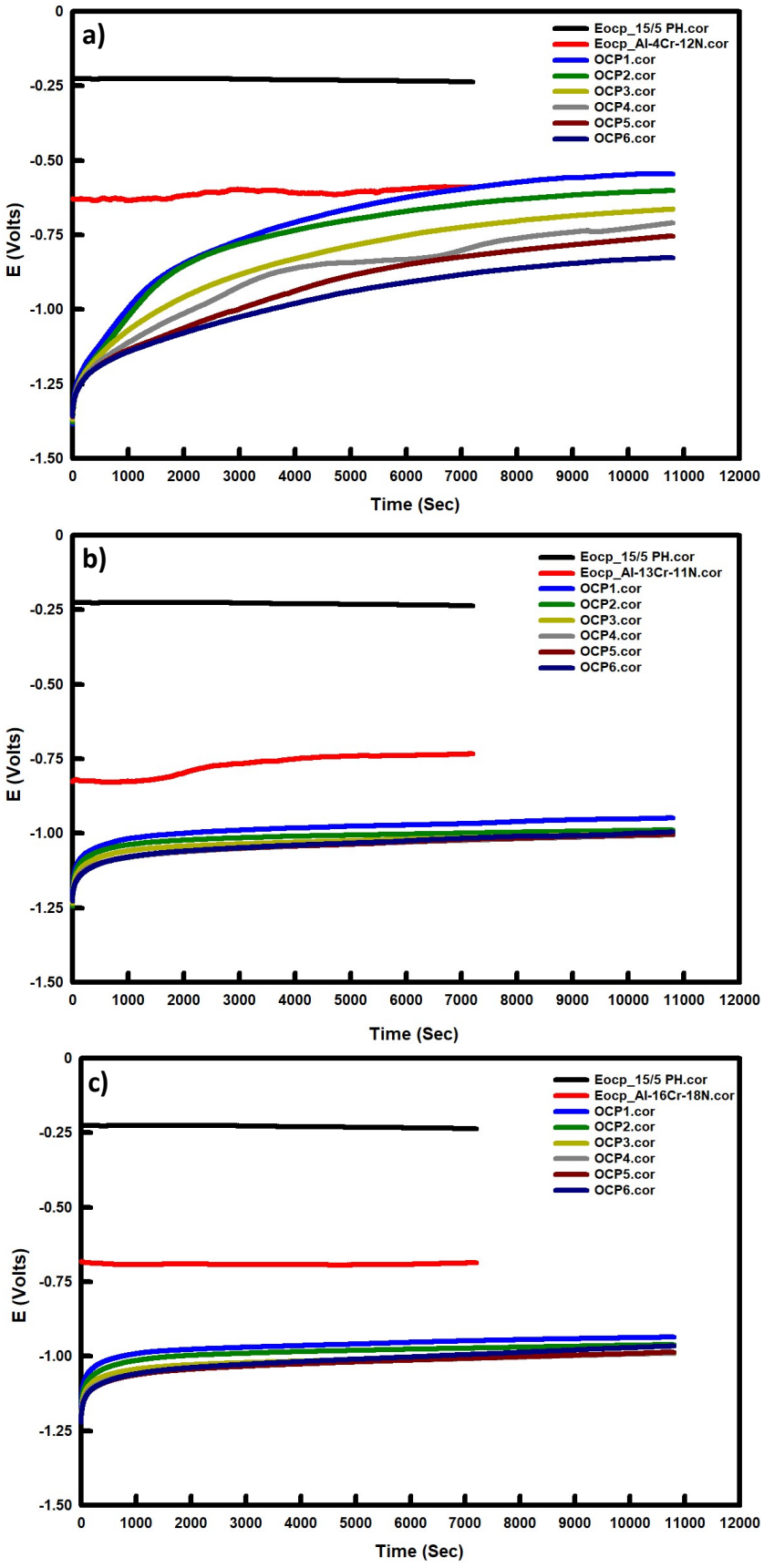

Figure 5.15: Evolution of the OCP of a) Al-4Cr-12N, b) Al-13Cr-11N and c) Al-16Cr-18N through six DC/OCP cycles

For Al-4Cr-12N, as shown in Figure 5.15a, the OCP quickly increases to -1.25V and above at the end of each DC step when the imposed potential of -1.5V is removed. OCP1 is the trend of the coating potential recorded throughout the three hours following DC1. From the results, it is clear that OCP1 showed the highest increase in potential with the final value measured to be -0.546V which exceeds that of the initial coating potential (-0.590V). This indicates that some level of coating degradation occurred during the DC1/OCP1 cycle, partially exposing the 15/5PH substrate and forcing the overall coating OCP towards more positive values. However, with increasing DC/OCP cycles, the anodic potential progressively decreased reaching a value of -0.826V at the end of OCP6. This gradual decrease can be attributed to the formation of two separate oxide films:

- A Cr-rich oxide layer in areas where the substrate has become exposed during the initial cycle
- A dense Al-rich oxide film (probably aluminium hydroxide ($Al(OH)_3$ as described in section 3.1.5) which built-up within the pores and at the surface of the coating

These oxide films - the presence of which was confirmed by EDX analysis (Figure 5.10) – had the beneficial effect of increasing the overall corrosion resistance of the coating, thereby protecting the underlying metal substrate.

From the plot of potential versus time describing the evolution in OCP for Al-13Cr-11N (Figure 5.15b), it is clear that once each DC cathodic polarisation step is completed, the potential quickly rises from -1.5V to -1.25V and continues to increase over a short period of time before becoming stable. In the initial stages of the relaxation period, the potential appears to decrease with increasing number of DC/OCP cycles. However the potential values measured towards the end of the relaxation step appear to be very close, particularly for OCP2 – OCP6. The highest potential value of -0.949V was recorded at the end of OCP1 decreasing slightly to between -0.989V and -1.004V for OCP2 – OCP6. In all cases the

potential therefore remained lower than the E_{OCP} of the coating and that of the substrate material (even though the substrate has been partially exposed as shown in Figure 5.11) due to the formation of a stable Cr-rich oxide film which has the benefit of improving the overall corrosion resistance of the coating/substrate system.

The evolution in OCP for Al-16Cr-18N (Figure 5.15c) follows a similar trend to that of Al-13Cr-11N with the potential decreasing slightly with increasing number of DC/OCP cycles but overall remaining lower (in the range of -0.936V to -0.989V) than the initial potential of the coating and that of the 15/5 PH substrate. Despite the fact that some coating damage occurred during the test, causing partial exposure of the substrate (as evident in Figure 5.12), the measured potential stayed fairly low. This is due to the formation of a dense oxide film - probably at the coating surface (from the high Cr content measured by EDX) and also in areas where the substrate has become exposed – which has the effect of enhancing the corrosion resistance properties of the coated material.

5.6.3 Evolution of EIS during six DC/OCP polarisation/relaxation cycles

EIS analysis of the AlCr(N) coatings was carried after the initial two-hour OCP (designated EISi) and subsequently after each consecutive DC/OCP cycle (EIS1-6) in order to monitor the condition of the coating/substrate system throughout the test. The results of the analysis are presented in terms of Nyquist plots in Figure 5.16 and Bode plots in Figures 5.17 (phase angle vs. frequency) and 5.18 (impedance modulus vs. frequency).

5.6.3.1 Nyquist plots

The EIS spectra of Al-4Cr-12N, Al-13Cr-11N and Al-16Cr-18N are illustrated in Figures 5.16a, 5.16b and 5.16c respectively. From the results it is clear that all AlCr(N) coatings displayed very different electrochemical corrosion behaviour during testing.

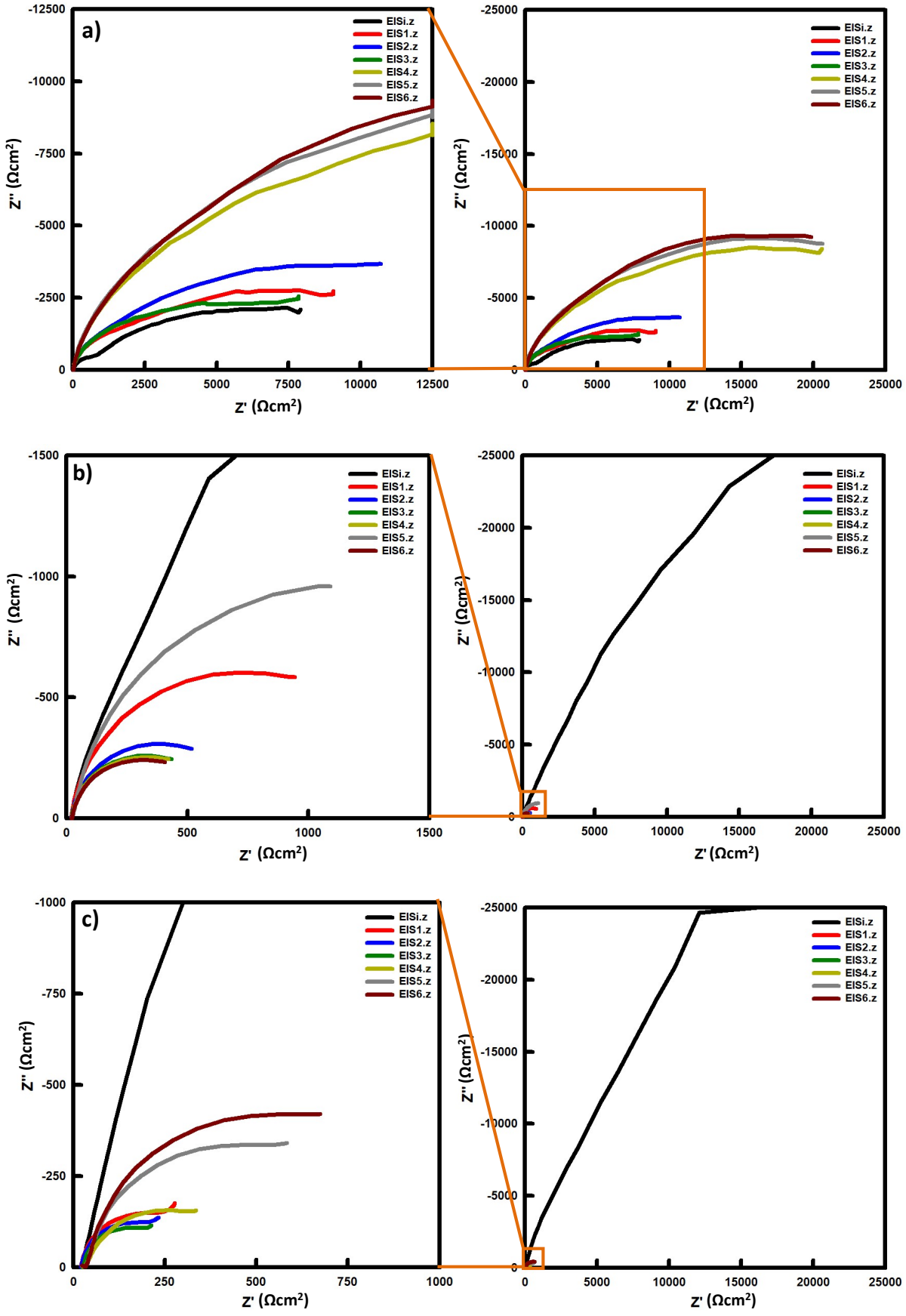

Figure 5.16: Nyquist plots of a) Al-4Cr-12N, b) Al-13Cr-11N and c) Al-16Cr-18N at initial E_{OCP} and after six successive DC/OCP cycles

For Al-4Cr-12N, the initial impedance spectrum (EISi) exhibits an incomplete semicircle at high frequencies, which is related to the capacitive nature of the passive film formed during the initial OCP (E_{OCP}). Subsequent EIS spectra (EIS1-6) showed an increase in semicircle radius with increasing number of DC/OCP cycles. This observed increase in semicircle radius can be attributed to an increase in the charge transfer resistance (R_{ct}) of the passive film which forms during OCP1-6, hence an increase in its corrosion resistance. It is evident that the characteristics of the passive film (i.e. thickness and/or permeability) change with each DC/OCP cycle. Indeed while a moderate increase in semicircle radius is observed for EIS1-3, a more significant increase is noted for EIS4-6. The increase in charge transfer resistance in the early DC/OCP cycles (EIS1-3) suggest the formation of a stable oxide film with improved corrosion resistance properties compared to those of the native oxide film present at EISi. The oxide film formed during OCP1-3 is probably a mixture of chromium oxide due to partial substrate exposure (as confirmed in Figure 5.15a by the observed increase in the potential of OCP1 beyond that of the initial coating OCP) and aluminium hydroxide as a result of coating dissolution. Although a slight reduction in semicircle radius was observed for EIS3, this was followed by a more significant increase in radius for EIS4-6 which can be attributed to an increase in the charge transfer resistance of both passive film and coating. This occurred as a result of the formation and build-up of a highly stable oxide film consisting probably of aluminium hydroxide at the coating surface and a mixed unhydrated Cr-Al oxide within the coating pores. The passive film in effect acts to plug the “holes” in the originally porous structure resulting in a considerable increase in the overall corrosion resistance of the coated system.

For Al-13Cr-11N the initial spectrum (EISi), which covers a wide range of frequencies, suggests the formation of a stable passive film - probably a Cr-rich oxide - on the coating surface during E_{OCP}. However after DC1/OCP1, a significant decrease in semicircle radius is

observed which can be attributed to a reduction in the charge transfer resistance of the coating as well as that of the passive film formed during OCP1, therefore implying that the native oxide film present at E_{OCP} (and possibly some coating) has been completely removed during DC1 and subsequently replaced by a less corrosion-resistant film during the relaxation step (OCP1). With subsequent DC/OCP cycles, a more gradual reduction in semicircle radius is observed up to DC4/OCP4, indicating that the thin passive film which re-formed during successive relaxation periods is unable to provide adequate corrosion protection to the underlying substrate/coating system, leading to further coating degradation with each DC step. The spectrum at EIS5 appears to show some improvement in corrosion resistance as the semicircle radius increases slightly, although remaining smaller than the one recorded at EISi. However this is short-lived as the spectrum at EIS6 reveals that further reduction in charge transfer resistance (hence corrosion resistance) of the passive film has occurred. The poor corrosion resistance properties of the passive film and coating were confirmed by EDX analysis (Figure 5.11) which showed that significant coating degradation has taken place, exposing the 15/5PH substrate.

The EIS spectra of Al-16Cr-18N appear to be very similar to those of Al-13Cr-11N during the initial cycles (EISi – EIS3). The spectrum at EISi suggests that a stable, corrosion-resistant Cr oxide film was generated on the coating surface during the initial OCP. However, with increasing number of DC/OCP cycles a significant reduction in semicircle radius is observed, which can be attributed to a decrease in charge transfer resistance (and therefore corrosion resistance) of the passive film and coating. This is probably due to coating degradation taking place during each DC step coupled with the fact that thin, less corrosion-resistant passive films formed during each subsequent relaxation period. A noticeable increase in semicircle radius was recorded from EIS4 onwards, indicating an improvement in the corrosion performance of the passive film. This is probably due to the build-up of a

chromium oxide film on the surface of any remaining coating as well as in areas where the substrate has become exposed, contributing to the overall increase in corrosion resistance.

5.6.3.2 Bode plots

Bode plots of phase angle versus frequency for Al-4Cr-12N, Al-13Cr-11N and Al-16Cr-18N are presented in Figures 5.17a, 5.17b and 5.17c, respectively. For Al-4Cr-12N, the initial spectrum (EISi) recorded at E_{OCP} displays two main peaks in the middle and high frequency ranges. A high phase angle peak at -64^{o} observed in the high frequency range is attributable to the capacitive nature of the passive film which formed on the surface of Al-4Cr-12N at E_{OCP}. The presence in the middle frequency range of a small phase angle peak at -33^{o} is indicative of the capacitive behaviour of the coating due to its porous structure. EIS spectra EIS1-6 obtained after six successive DC/OCP cycles are characterised by one main phase angle peak over a wide range of frequencies which confirms the presence of a stable oxide film on the surface of Al-4Cr-12N. For EIS spectra 4-6, the phase angle peak shifts towards the low frequency range with increasing number of DC/OCP cycles. Furthermore, the single peak not only broadens but also experiences an increase in phase angle displaying -76^{o} for EIS5. This suggests the formation of a highly stable oxide film, of which the effectiveness in providing corrosion protection increases with increasing number of DC/OCP cycles.

For Al-13Cr-11N, two main peaks are visible on the EISi spectrum in the low and middle frequency range with phase angles of -64^{o} and -72^{o}, respectively. Moreover the peaks are broad, covering a wide range of frequencies which confirms the stable nature of the passive film formed at E_{OCP}. However the profile of the spectrum dramatically changes right after the first DC/OCP cycle, displaying a single narrow peak in the low frequency range and a slight

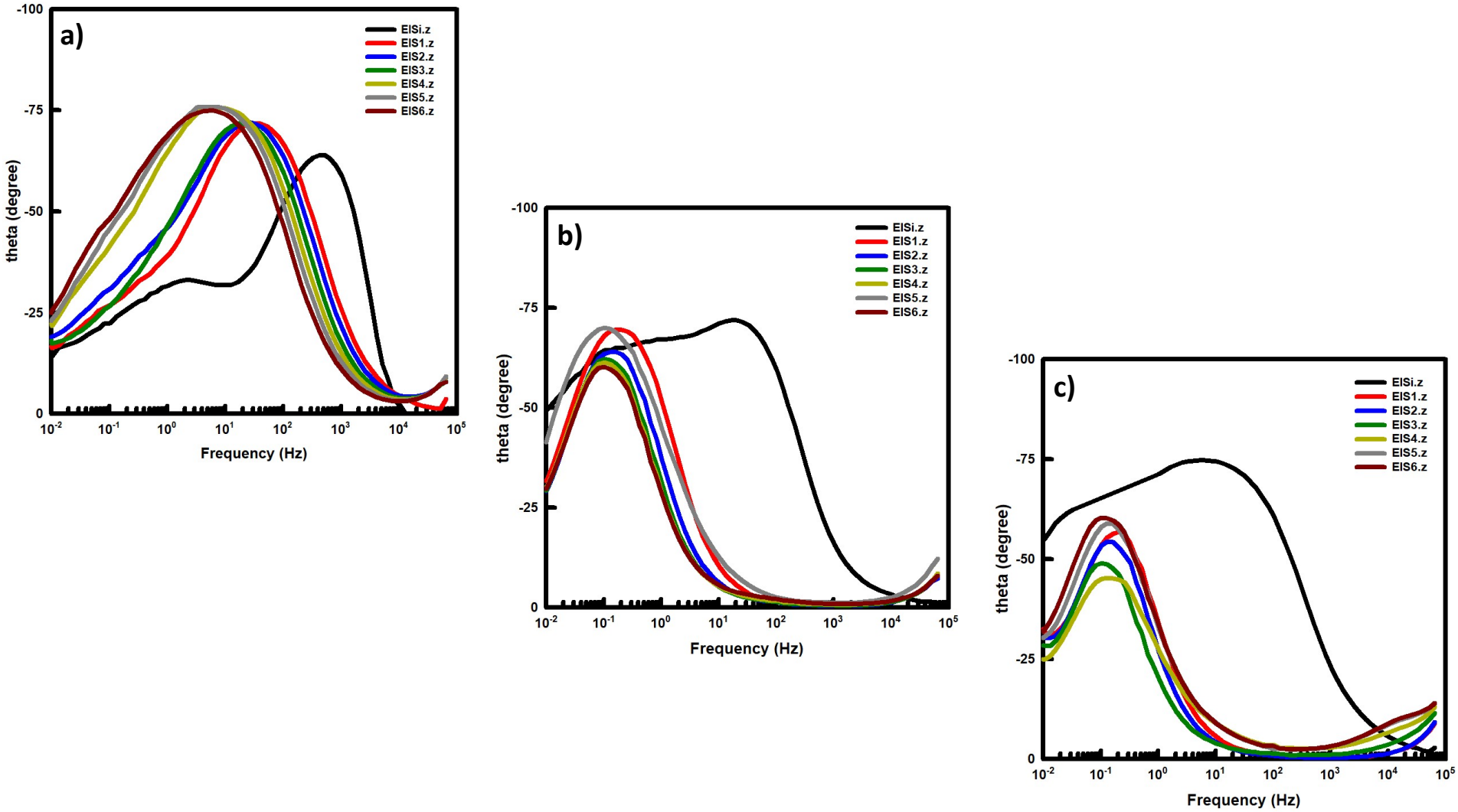

Figure 5.17: Bode plots (phase angle vs. frequency) of a) Al-4Cr-12N, b) Al-13Cr-11N and c) Al-16Cr-18N at initial E_{OCP} and after six successive DC/OCP cycles

reduction in phase angle to -70^{o}, which suggests that the passive film formed during OCP1 is not as corrosion resistant as the native oxide film. A similar profile was obtained for the spectra of EIS2-6, with the main difference being that further reduction in phase angle was observed, with the lowest phase angle of -60^{o} recorded for EIS6. This indicates a gradual decrease in the corrosion performance of the passive films generated, during each subsequent relaxation period.

The spectrum of Al-16Cr-18N at EISi displays a broad peak in the middle frequency range with a measured phase angle of -75^{o}, the highest recorded for the native passive films generated on the surface of the three AlCr(N) coatings. This can be attributed to the formation of a stable Cr-rich oxide film on the coating surface at E_{OCP}. With increasing number of DC/OCP cycles, a noticeable decrease in phase angle (down to -45^{o} for EIS4) coupled with a narrowing of the peak, are observed as a result of significant coating damage occurring during each DC step (as confirmed by EDX analysis in Figure 5.12) - as well as a reduction in the corrosion resistance properties of the thin passive film generated during subsequent relaxation periods. EIS4-6 are characterised by a slight broadening of the peak, as well as an increase in phase angle to above that measured for EIS1, which indicates that some improvement in corrosion performance has occurred, probably due to the build-up of a Cr-rich oxide film at the surface of both substrate and coating.

Bode plots of impedance modulus versus frequency for Al-4Cr-12N, Al-13Cr-11N and Al-16Cr-18N are illustrated in Figures 5.18a, 5.18b and 5.18c, respectively. For Al-4Cr-12N, the impedance modulus $|Z|$ at EISi was measured to be 8.2 x 10^{3} Ωcm^{2}. This value steadily increased with increasing number of DC/OCP cycles up to EIS2, which indicates an increase in the corrosion resistance of the coated system. A slight drop in impedance modulus was observed at EIS3, which exhibits the lowest recorded impedance value of 7.2 x 10^{3} Ωcm^{2}.

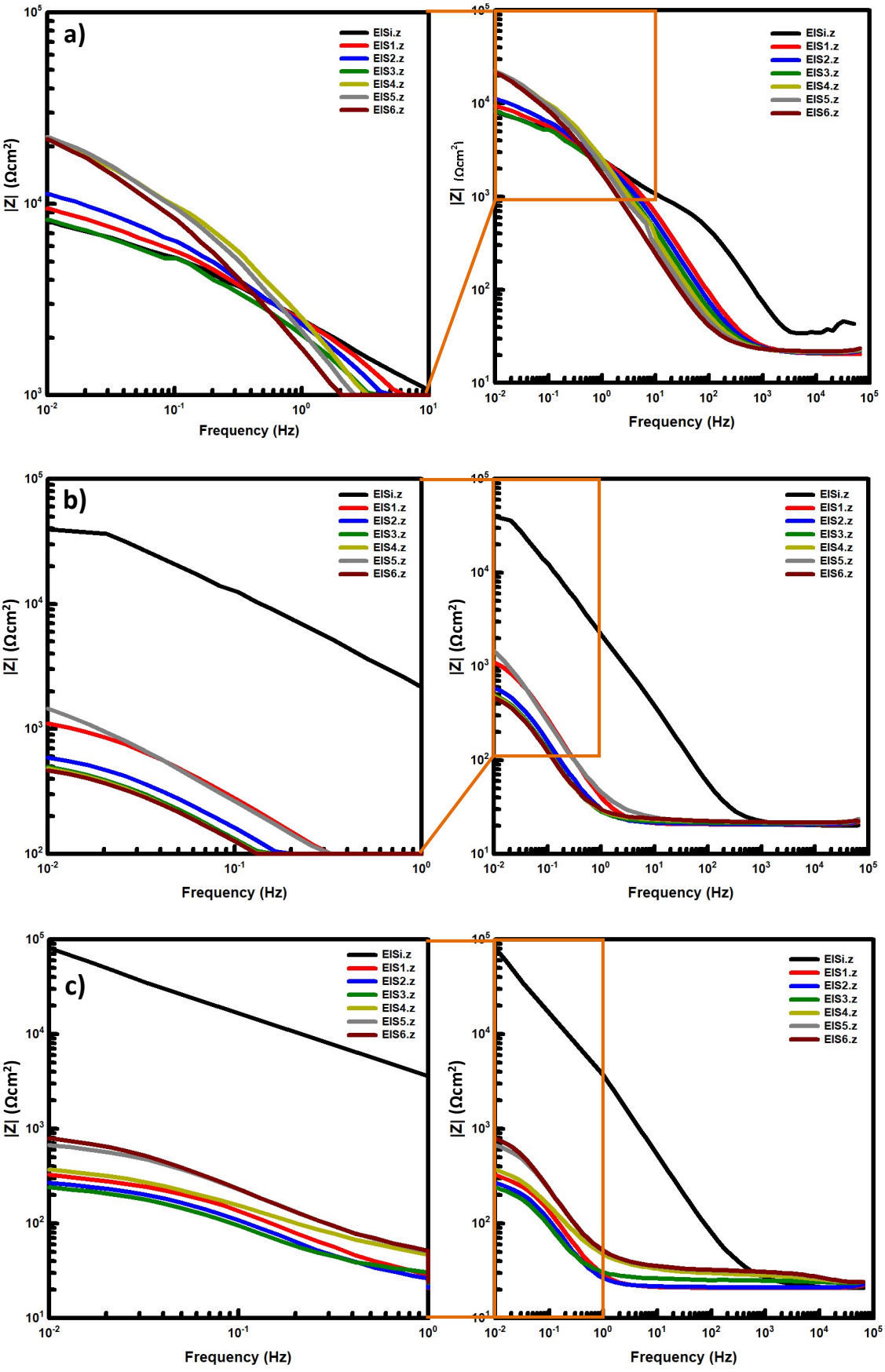

Figure 5.18: Bode plots (impedance modulus vs. frequency) of a) Al-4Cr-12N, b) Al-13Cr-11N and c) Al-16Cr-18N at initial E_{OCP} and after six successive DC/OCP cycles

From EIS4 onwards $|Z|$ significantly increases, reaching a value of 2.2 x 10^4 Ωcm^2 - which can be attributed to a considerable increase in the charge transfer resistance (and hence the corrosion resistance of the passive film/coating system), as a result of the formation and build-up of a highly stable oxide film. Overall, the EIS spectra seem to exhibit a similar slope, showing a progressive decrease in impedance with increasing frequency and reaching a plateau at a frequency of 1000 Hz.

For Al-13Cr-11N, the highest Bode modulus was recorded at EISi (3.9 x 10^4 Ωcm^2) which implies the formation of a highly stable passive film on the coating surface during the initial OCP. The slope of the EISi spectrum shows a steady decrease in impedance with frequency until a plateau region is reached at around 1000 Hz. However, for EIS1-6 the slope of the spectrum looks significantly different, with the impedance rapidly dropping and reaching a plateau at a much lower frequency (around 1 Hz). Furthermore, the impedance value significantly decreased to around 1.1 x 10^3 Ωcm^2 after the first DC/OCP cycle (EIS1), indicating that the new passive film generated during OCP1 is less corrosion-resistant compared to the native oxide film (which was probably removed during DC1). The impedance continues to steadily decrease with increasing number of cycles, reaching 4.7 x 10^2 Ωcm^2 at EIS6. This suggests a significant reduction in the corrosion resistance of the coated system - probably as a result of severe coating degradation taking place during each DC step, coupled with the formation of thin passive films during successive relaxation steps (which provide very little protection against corrosion).

For Al-16Cr-18N, the impedance value at E_{OCP} was measured to be 8.1 x 10^4 Ωcm^2, the highest recorded value for all three AlCr(N) coatings under investigation. This suggests that, owing to the high Cr content of the coating, a highly stable corrosion-resistant Cr-rich oxide film was generated on the coating surface during the initial OCP. However a significant decrease in impedance is observed with successive DC/OCP cycles up to DC3/OCP3,

indicating that the passive film which forms during each relaxation step is unable to provide adequate corrosion protection. From EIS4 onwards, a noticeable increase in impedance is recorded which suggests that the formation and build-up of a Cr oxide film (at the substrate surface and the surface of any remaining coating) during OCP4-6 has the beneficial effect of improving the overall corrosion resistance properties of the coated steel.

5.6.3.3 Equivalent circuit (EC) models

From the EIS data presented above, it was possible to build relevant equivalent circuits in order to obtain an improved understanding of the electrochemical corrosion behaviour of the AlCr(N) coatings at E_{OCP} and after each DC/OCP cycle (Figure 5.19). The equivalent circuits were constructed from three main electrical elements: a solution resistance element (Rs) arranged in series with a combination of charge-transfer element, R_{ct} (expressed as R1 or R2 in the ECs below) and constant phase element, CPE (expressed as CPE1 or CPE2), and related to the double layer capacitance C_{dl} of the passive film and/or the coating capacitance C_c, respectively.

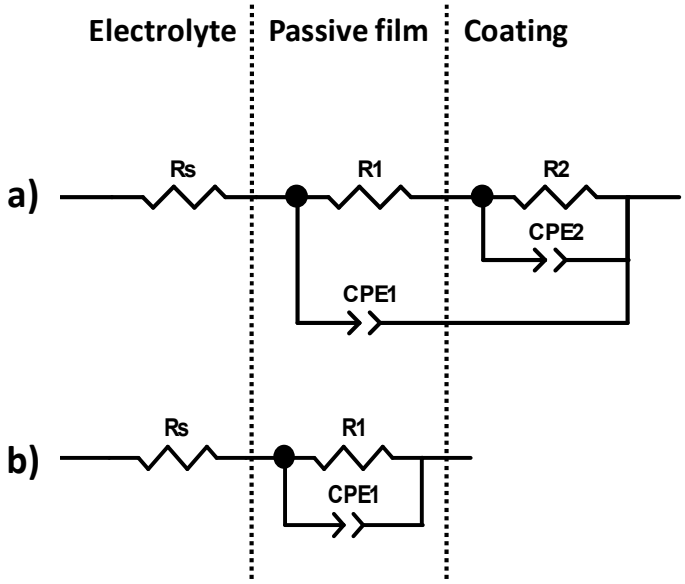

Figure 5.19: Equivalent circuits used to model a) EISi – EIS6 of Al-4Cr-12N, EISi of Al-13Cr-11N and Al-16Cr-18N and b) EIS1 –EIS6 of Al-13Cr-11N and Al-16Cr-18N

For Al-4Cr-12N, the equivalent circuit obtained from the measured EIS spectra is illustrated in Figure 5.19a. This equivalent circuit was used to model EIS data recorded at E_{OCP} (EISi) and after each DC/OCP cycle (EIS1-6). The proposed model consists of the solution resistance Rs in series with two time constants (R1 CPE1 and R2 CPE2) arranged in parallel and representing the charge transfer resistance of the passive film and the Al-4Cr-12N coating, respectively. For Al-13Cr-11N, the equivalent circuit illustrated in Figure 5.19a was used to model the initial EIS spectrum (EISi) recorded at E_{OCP}, with R1 CPE1 and R2 CPE2 corresponding to the charge transfer resistance of the passive film (formed during E_{OCP}) and the Al-13Cr-11N coating, respectively. To model the EIS spectra obtained after each DC/OCP cycle (EIS1-6), the equivalent circuit presented in Figure 5.19b – which comprises a single time constant (R1 CPE1), representing the charge transfer resistance of the passive film formed on the substrate surface – was used. The two equivalent circuits shown in Figure 5.19 were also used to model the EIS spectra of Al-16Cr-18N. The EC in Figure 5.19a was selected to model the EISi spectrum while the one in Figure 5.19b was used to model EIS1-6. Fitting every EIS spectrum recorded at E_{OCP} and after each successive DC/OCP cycle with the appropriate equivalent circuit provided a specific value for each phase element for all three AlCr(N) coatings as shown in Tables 5.3, 5.4 and 5.5. For ease of interpretation, values of R1, R2, CPE1 and CPE2 were plotted against the number of DC/OCP cycles as presented in Figures 5.20, 5.21 and 5.22 for Al-4Cr-12N, Al-13Cr-11N and Al-16Cr-18N, respectively. The charge transfer resistance and CPE values recorded can be used to better understand the complex corrosion behaviour of an electrically-conductive coating/substrate system.

For Al-4Cr-12N, it is clear from Figure 5.20a that the charge transfer resistance of the passive film (R1) increases from 0.9 to 2.2 $k\Omega\ cm^2$ after the first DC/OCP cycle which indicates an increase in the thickness of the passive film resulting in improved corrosion resistance. A slight decrease in charge transfer resistance of the coating (R2) is observed after the first

Table 5.3: Fitting results of EIS spectra obtained at E_{OCP} and after six consecutive DC/OCP cycles for Al-4Cr-12N

Cycle number	Rs (Ωcm^2)	CPE1 (µF/cm^2)	R1 (kΩ cm^2)	n	CPE2 (µF/cm^2)	R2 (kΩ cm^2)	n
E_{OCP}	36.1	3.6	0.9	0.97	154.9	11.7	0.44
1	20.7	32.6	2.2	0.91	238.1	10.8	0.55
2	21.1	41.2	2.1	0.91	187.1	14.8	0.52
3	21.5	52.3	1.9	0.90	252.4	11.8	0.43
4	21.7	66.9	8.4	0.90	182.1	23.9	0.63
5	21.9	80.8	8.9	0.90	168.1	23.6	0.63
6	22.2	105.4	9.3	0.89	202.2	21.1	0.70

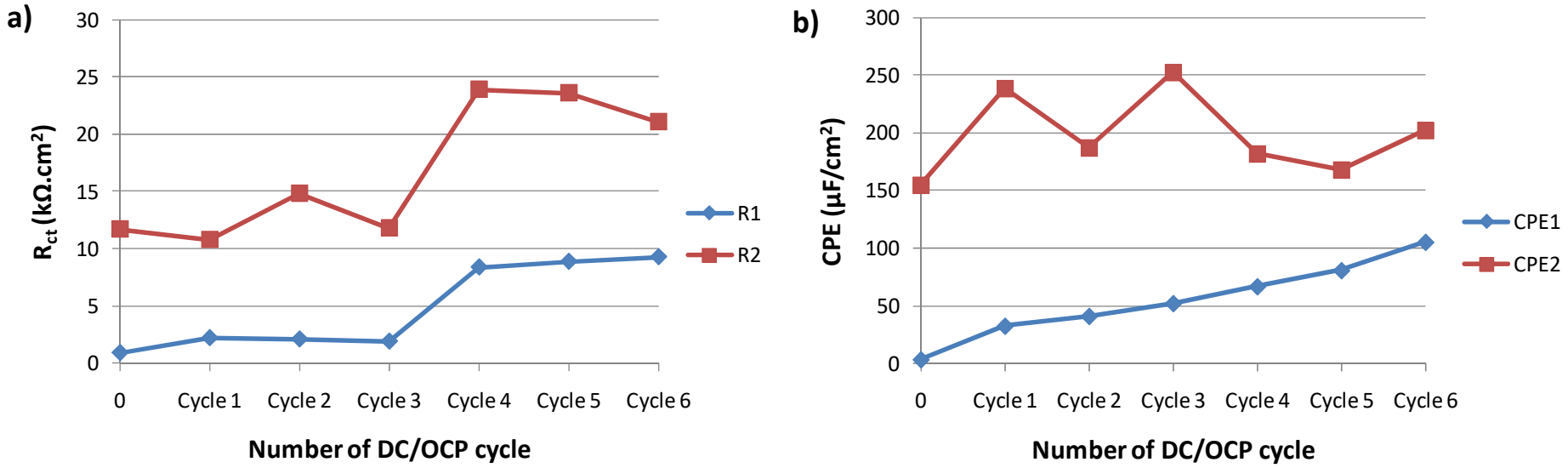

Figure 5.20: Evolution of a) charge transfer resistance R_{ct} and b) CPE of the passive film (R1 CPE1) and the Al-4Cr-12N coating (R2 CPE2) as a function of the number of DC/OCP cycles

Table 5.4: Fitting results of EIS spectra obtained at E_{OCP} and after six consecutive DC/OCP cycles for Al-13Cr-11N

Cycle number	R_s (Ωcm^2)	CPE_1 ($\mu F/cm^2$)	R_1 ($k\Omega\ cm^2$)	n	CPE_2 ($\mu F/cm^2$)	R_2 ($k\Omega\ cm^2$)	n
at E_{OCP}	20.3	56.1	1.7	0.91	63.9	146.9	0.65
1	20.6	5554.1	1.4	0.92			
2	20.9	9719.2	0.7	0.91			
3	21.6	12046	0.6	0.91			
4	22.3	12515	0.6	0.90			
5	22.2	5654.2	2.5	0.87			
6	22.4	12541	0.6	0.88			

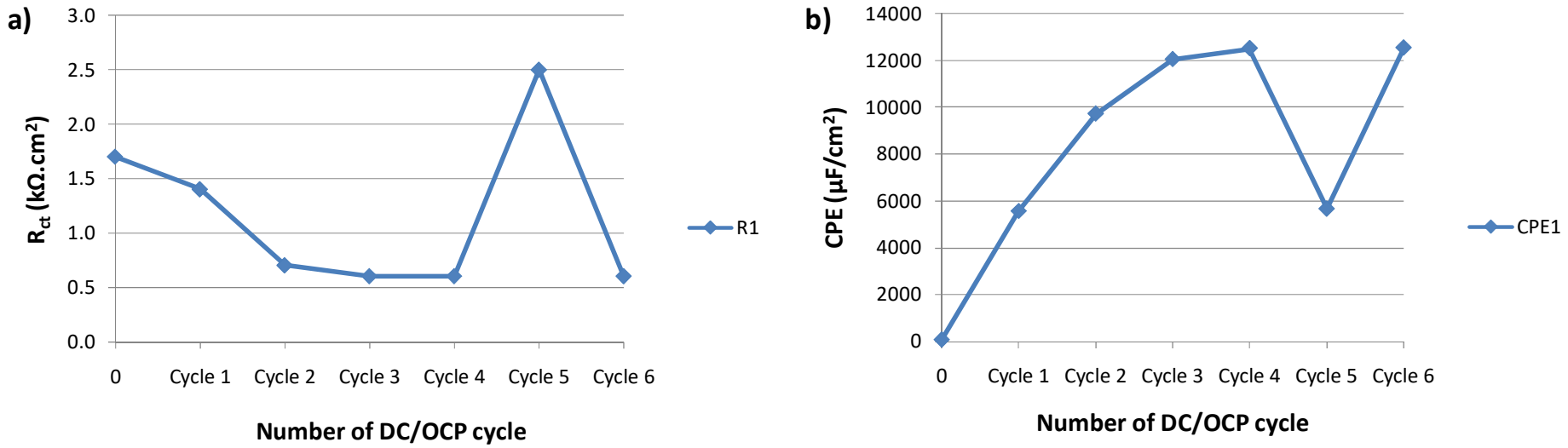

Figure 5.21: Evolution of a) charge transfer resistance R_{ct} and b) CPE of the passive film for Al-13Cr-11N coating as a function of the number of DC/OCP cycles

Table 5.5: Fitting results of EIS spectra obtained at E_{OCP} and after six consecutive DC/OCP cycles for Al-16Cr-18N

Cycle number	R_s (Ωcm^2)	CPE_1 ($\mu F/cm^2$)	R_1 ($k\Omega\ cm^2$)	n	CPE_2 ($\mu F/cm^2$)	R_2 ($k\Omega\ cm^2$)	n
at EOCP	21.4	55.6	31.7	0.85	96.0	188.3	0.96
1	20.5	11631	0.39	0.87			
2	21	15088	0.31	0.88			
3	25.5	17871	0.28	0.85			
4	30.2	9358.8	0.48	0.74			
5	33	6703.6	0.88	0.85			
6	33.7	6642.3	1.1	0.85			

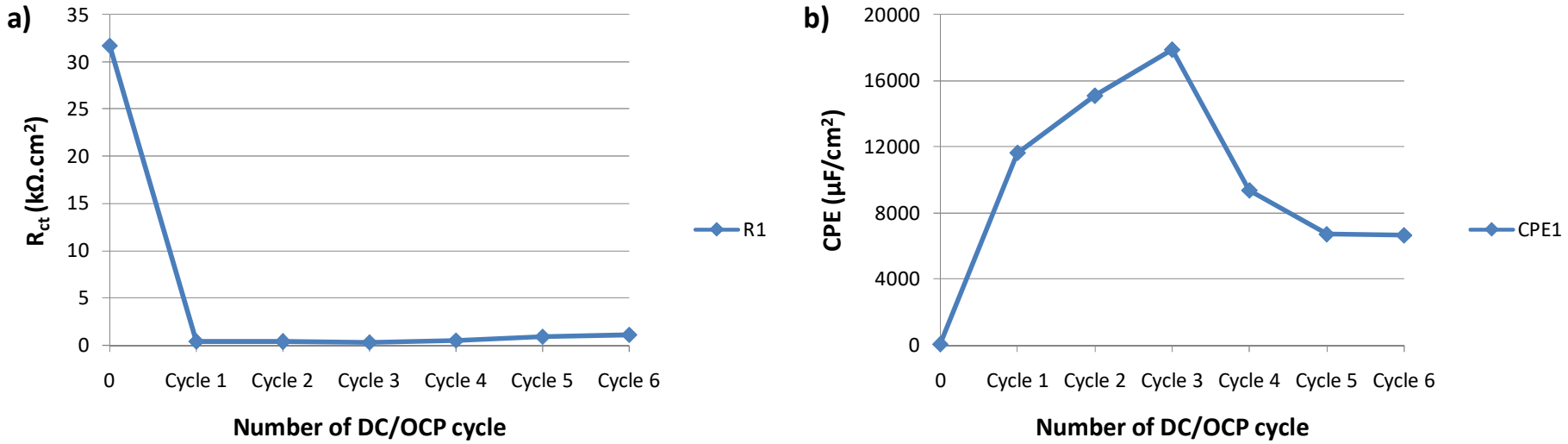

Figure 5.22: Evolution of a) charge transfer resistance R_{ct} and b) CPE of the passive film for Al-16Cr-18N coating as a function of the number of DC/OCP cycles

cycle due to partial exposure of the substrate to the electrolyte during DC1. This is confirmed by the reported increase in OCP1 values to beyond that of the initial coating OCP, as shown in Figure 5.15. While R1 remains stable for the next two cycles, indicating little variation in the thickness of the passive film (which partially dissolves and reforms during each DC/OCP cycle), R2 exhibits a noticeable increase after DC2/OCP2 which can be attributed to the formation of a chromium oxide (Cr_2O_3) passive film at the coating/substrate interface as a result of substrate exposure during DC1. This would have the benefit of increasing the overall corrosion resistance of the coating/substrate system. After the third DC/OCP cycle, a slight decrease in the charge transfer resistance (hence corrosion resistance) of the coating is observed, probably due to further opening of the coating pores during DC3, enabling the electrolyte to penetrate through the coating and exposing more substrate material. A significant increase in charge transfer resistance of both the passive film and the coating occurs after DC4/OCP4 with R1 and R2 rising from 1.9 to 8.4 kΩ cm^2 and from 11.8 to 23.9 kΩ cm^2, respectively. For R1, this noticeable increase in the corrosion resistance of the passive film can be explained by the dissolution of the previous passive film (formed during OCP3) and the partial dissolution of the coating during DC4, leading to the formation of a thicker passive film during OCP4. In the case of R2, the sharp increase in corrosion resistance is due to the combined effect of the formation and build-up of a chromium oxide passive film at the coating/substrate interface (after further substrate exposure in DC3) and the formation of an aluminium oxide passive film within the coating pores. Both factors would significantly contribute to an increase in the corrosion resistance of the coated system. For subsequent DC/OCP cycles, very little change in charge transfer resistance occurs for both passive film and coating - with the overall corrosion resistance of the system remaining high.

As shown above, the use of constant phase elements (CPEs) was required to obtained suitable EC models. CPEs are usually used in equivalent circuits to take into account the non-ideal behaviour of coatings which cannot be represented by pure resistors or capacitors alone, as they exhibit local variations in composition, structure or surface topography, any of which could influence the interactions at the coating/electrolyte interface. The parameter 'n' (shown in Tables 5.1, 5.2 and 5.3) is closely related to the impedance of a CPE and can take values in the range of -1 to +1. The CPE is said to be a capacitor when n approaches 1, a resistor for n close to 0 and an inductor for n values tending towards -1, while n closer to 0.5 suggests that diffusion processes involving the movement of ionic species (e.g. Al^{3+}, Cl^-) are taking place at the coating/electrolyte interface [162]. CPE values plotted as a function of the number of DC/OCP cycles are illustrated in Figure 5.20b. It can be seen that CPE1 gradually increases with increasing number of cycles which indicate the formation of a dense passive film at the surface of the coating. The observed increase in cycle 4 of the charge transfer resistance R1 (due to an increase in the thickness of the passive film) does not lead to a significant increase in its capacitance. CPE2 appears to fluctuate particularly during the first three cycles, mirroring the fluctuations observed in R2. Indeed in cycle 1, R2 decreases due to partial substrate exposure from opening of the coating pores, which in turn causes the coating capacitance (CPE2) to increase as the electrolyte is allowed to penetrate through the coating. The same effect is observed after the third DC/OCP cycle. After DC2/OCP2, the corrosion resistance of the coating (R2) increases with the formation of the chromium oxide passive film leading to a reduction in CPE2 as less electrolyte is able to infiltrate the coating. After the fourth cycle, CPE2 decreases significantly for the same reasons that R2 increases: formation of chromium oxide passive film at the coating substrate interface and build-up of the aluminium oxide passive film within the coating pores which in effect blocks the pores therefore preventing the electrolyte from penetrating through the coating and leading to a

reduction in coating capacitance. Negligible changes in coating capacitance were observed in cycle 5 with a slight increase noted in cycle 6 with decreasing R2. It is worth pointing out at this stage that the test was only carried out once on the AlCr(N) coatings and, as shown by Indeir [6] - who performed three test repeats on an uncoated Al substrate - significant variations in results can occur. Due to lack of time, it was not possible to carry out those repeats - which should be done in future, in order to be certain that the coating corrosion behaviour observed here is typical and repeatable.

For Al-13Cr-11N, the evolution of the charge transfer resistance and CPE was plotted only for R1 and CPE1 to describe the corrosion behaviour of the coated system. It is evident from Figure 5.21a that the charge transfer resistance of the passive film (R1) decreases with increasing number of DC/OCP cycles up to cycle 4. This noticeable decrease in corrosion resistance with increasing number of cycles is due to the dissolution of the passive film and coating during successive cathodic polarisation steps, leading to severe coating degradation - as confirmed by the EDX analysis in Figure 5.11, which revealed that the underlying 15/5 PH substrate has been exposed. The passive film which forms at the surface of the substrate during subsequent relaxation periods has a low corrosion resistance compared to that of the native oxide film. R1 appears to increase significantly after DC5/OCP5, possibly due to the formation of a thicker Cr-rich oxide film mainly at the surface of the substrate - but also at the surface of any remaining Al-13Cr-11N, which would have the effect of improving the overall corrosion resistance of the coating/substrate system. However, the charge transfer resistance of the passive film decreases sharply after cycle 6 – with measured R1 values similar to those recorded for cycles 2, 3 and 4 - which indicates that the thicker oxide film generated during OCP5 was completely removed during DC6 and replace with a thinner, less corrosion-resistant film. Looking at the CPE graph (Figure 5.21b), it is clear that in most cases, the CPE1 values appear to increase with increasing number of cycles (and decreasing

R1) which suggests an increase in capacitance as a result of significant coating degradation taking place.

For Al-16Cr-18N, the charge transfer resistance of the passive film, which is very high at E_{OCP}, decreases significantly after the first DC/OCP cycle - which indicates that removal of the native passive film and severe coating degradation has occurred during DC1, resulting in the subsequent formation of a thinner and less corrosion-resistant film during OCP1. R1 remains low until the end of the test, although a slight increase was noted during the remaining three cycles. The observed reduction in the charge transfer resistance (hence in the corrosion resistanc) is caused by the dissolution of the passive film (and coating) during successive DC steps and the formation of a thin oxide film during subsequent relaxation periods. The small improvement recorded in cyles 4, 5 and 6 is probably due to the slight increase in the thickness of the passive film generated at the substrate surface. As shown in Figure 5.22b, CPE1 appears to increase with increasing number of cycles and decreasing R1. This increase in capacitance occurs as a result of coating degradation which enables the electrolyte to infiltrate the coating. The CPE values decrease from cycle 4 onwards with increasing R1 as the small increase in the thickness of the passive film reduces the 'space' occupied by the electrolyte hence leading to the observed decrease in capacitance.

For all three AlCr(N) coatings, a close fit was achieved between the calculated data obtained from the equivalent circuit models and the experimental EIS spectra (at EISi and EIS1-6) with the goodness of fit given by chi-squared values in the range of 10^{-4} – 10^{-2}. The fitting results for EIS3 of Al-4Cr-12N, Al-13Cr-11N and Al-16Cr-18N are presented in Figures 5.23, 5.24 and 5.25, respectively.

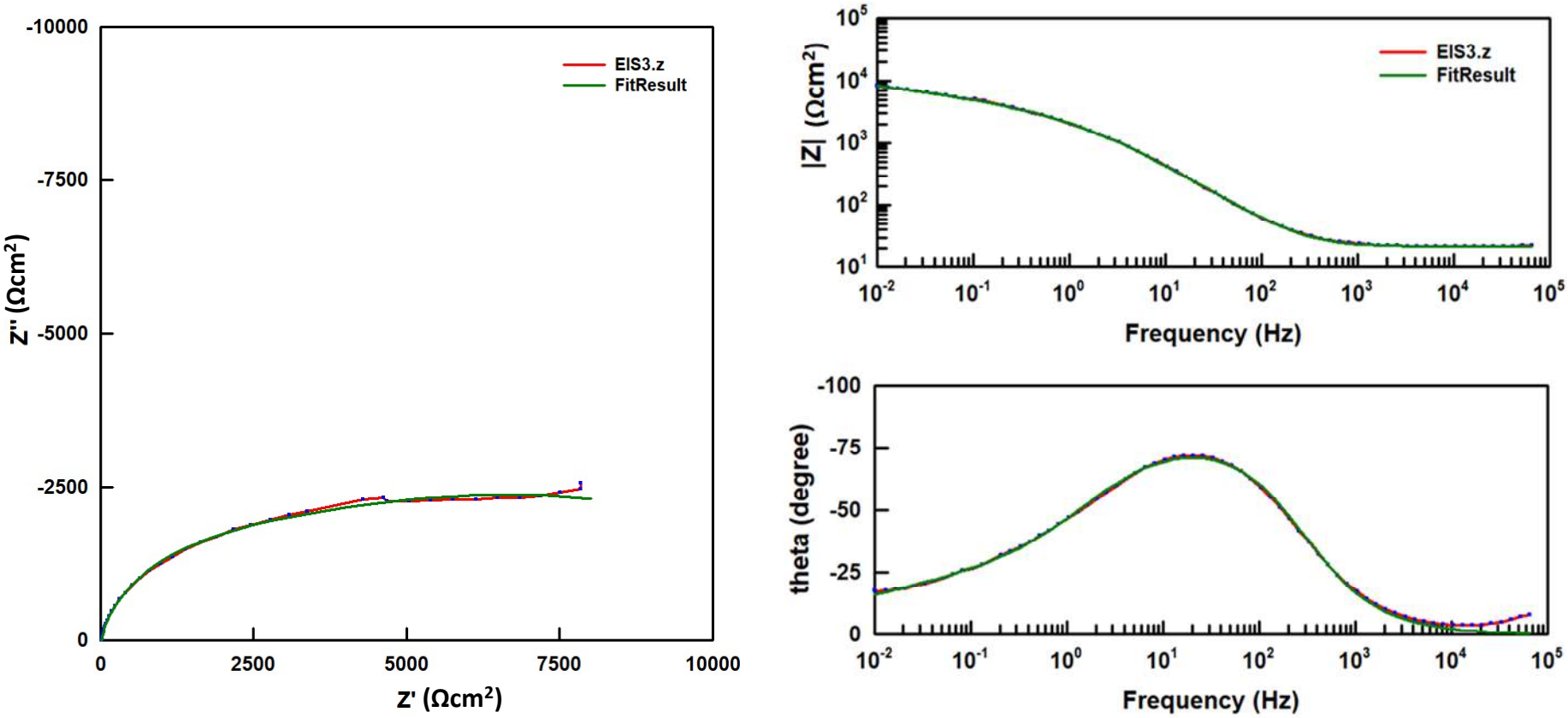

Figure 5.23: Fitting of the proposed equivalent circuit models to the experimental EIS3 data for Al-4Cr-12N

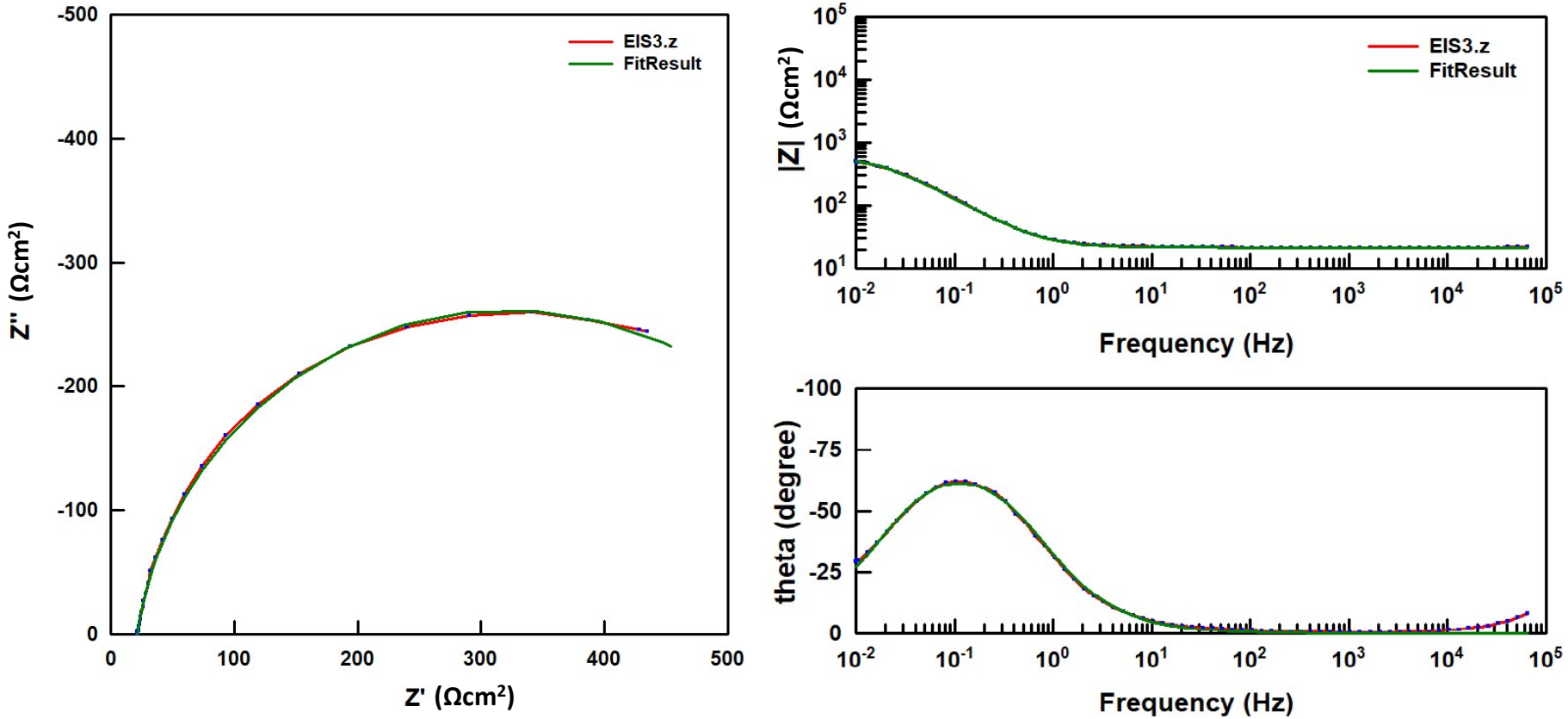

Figure 5.24: Fitting of the proposed equivalent circuit models to the experimental EIS3 data for Al-13Cr-11N

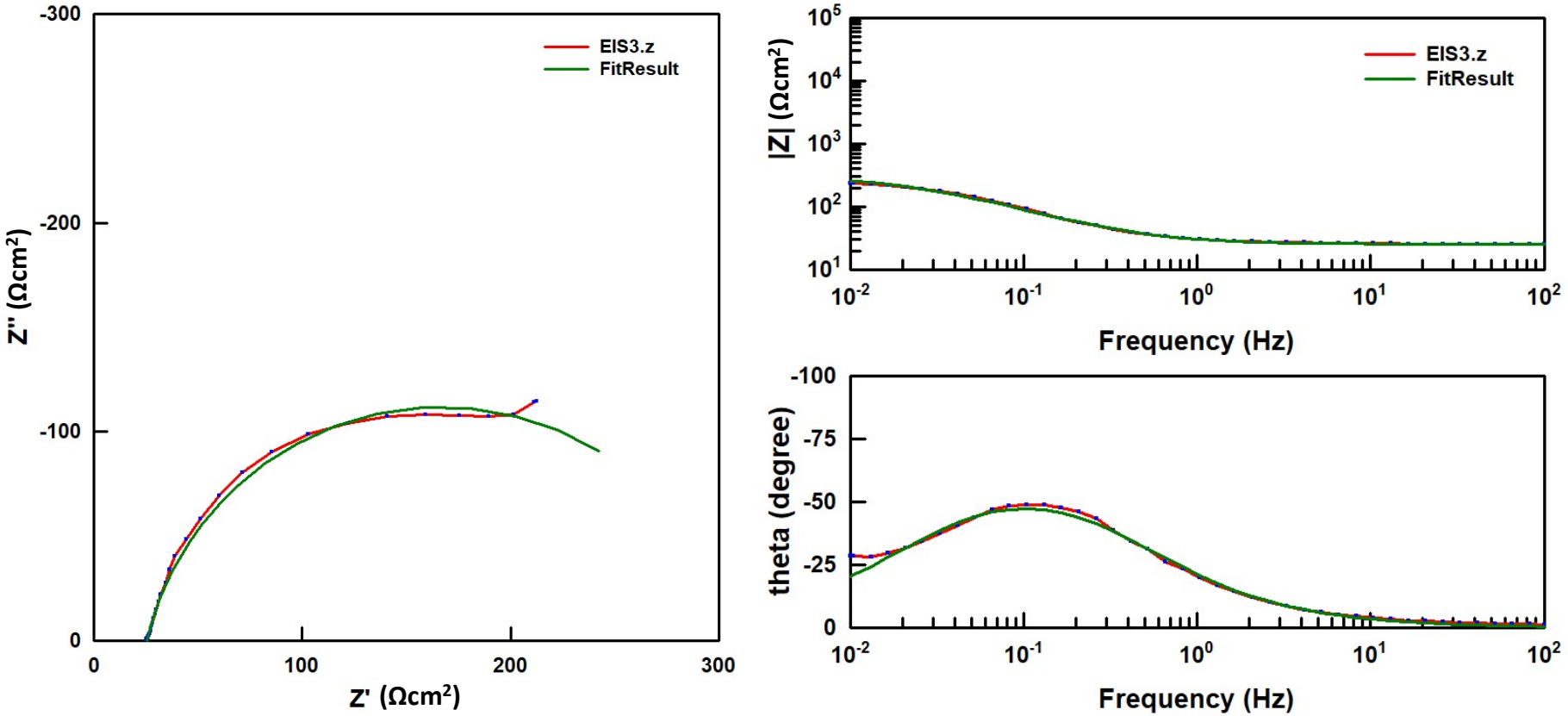

Figure 5.25: Fitting of the proposed equivalent circuit models to the experimental EIS3 data for Al-16Cr-18N

5.6.4 Evolution of solution pH during AC/DC/AC cyclic test of AlCr(N) coatings

The solution pH was monitored during the initial OCP and throughout the AC/DC/AC test in order to understand how the pH evolves through each stage of testing and what effect changes in solution alkalinity have on the corrosion behaviour of the AlCr(N) coatings under investigation. The results are presented in Figures 5.26, 5.27 and 5.28 for Al-4Cr-12N, Al-13Cr-11N and Al-16Cr-18N, respectively.

For Al-4Cr-12N, the solution pH is around 6 at the start of $E_{OCP,}$ decreasing slightly before quickly reaching a steady state value of 5.8 where it remains until the first cathodic polarisation (DC1) step is initiated. When -1.5V potential (vs. SCE) is applied on the sample during DC1 a noticeable increase in the alkalinity of the solution is observed. This is due to a decrease in hydrogen ion (H^+) concentration of the electrolyte (hydrogen ion decay) as a result of adsorbed hydrogen (H_{ads}) formation (from H^+ ion reduction reaction) at the cathode/electrolyte interface with either subsequent migration into the coating (absorbed hydrogen; H_{abs}) or generation of H_2 gas, as described in Chapter 3. DC1 is followed by a three-hour relaxation period (OCP1) during which the solution pH steadily decreases, reaching weak alkaline values prior to the start of DC2 and more neutral values prior to starting subsequent DC cycles (DC3-DC6). This observed decrease in the solution pH with values tending towards neutral, occurs due to the cathodic reduction reaction of water, taking place simultaneously with anodic coating dissolution (as described in equation 3.20), coupled with the acidification of the solution as a result of pitting corrosion (as illustrated by equation 3.34). The solution pH increases during all subsequent DC steps (DC2-DC6) although the final pH values are lower than the ones recorded at the end of DC1. During OCP2-OCP6, the solution alkalinity after relaxation to OCP progressively decreases - although some fluctuations in pH values are observed in the early stages of the relaxation step, particularly

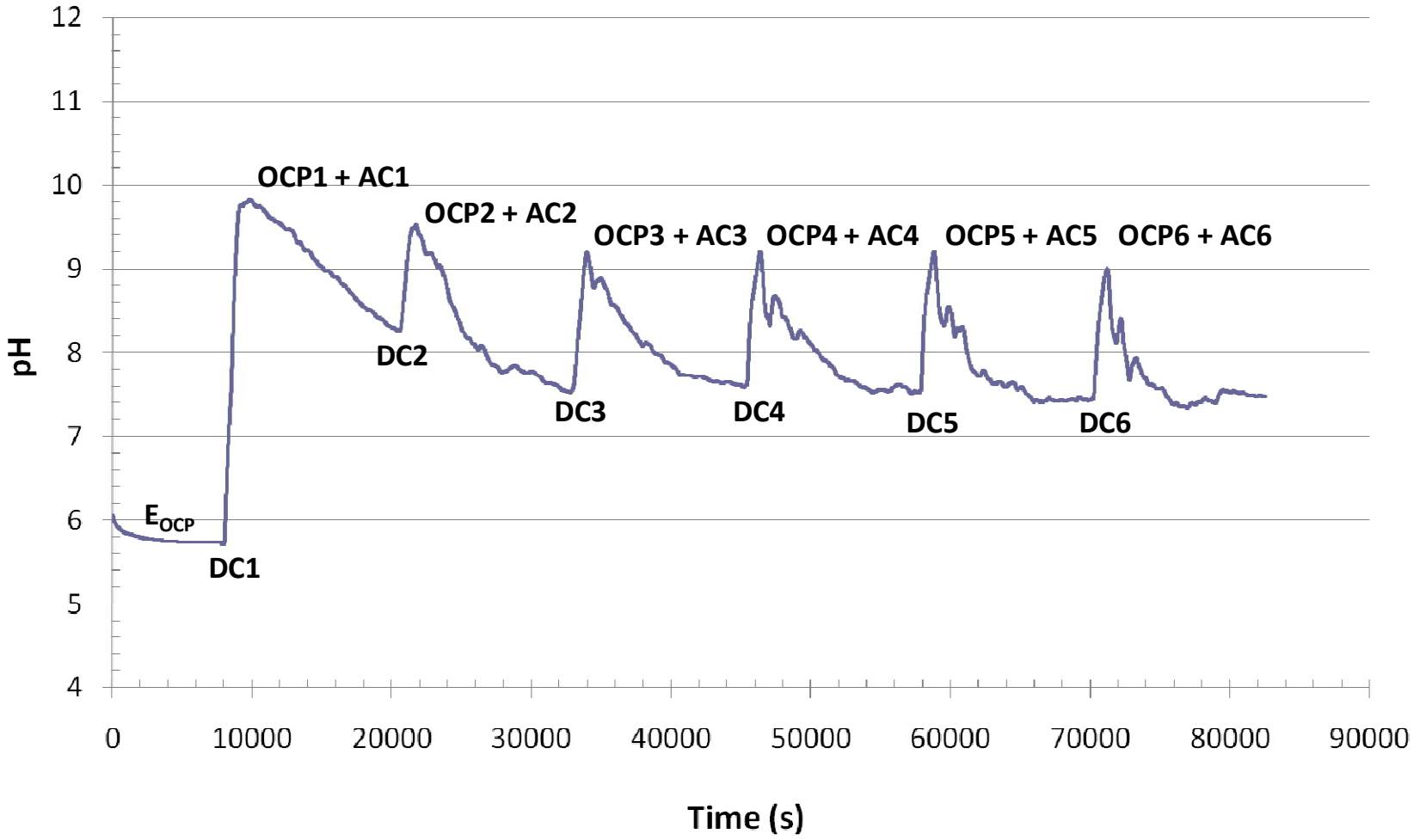

Figure 5.26: Evolution of the solution pH during six DC/OCP cycles for Al-4Cr-12N

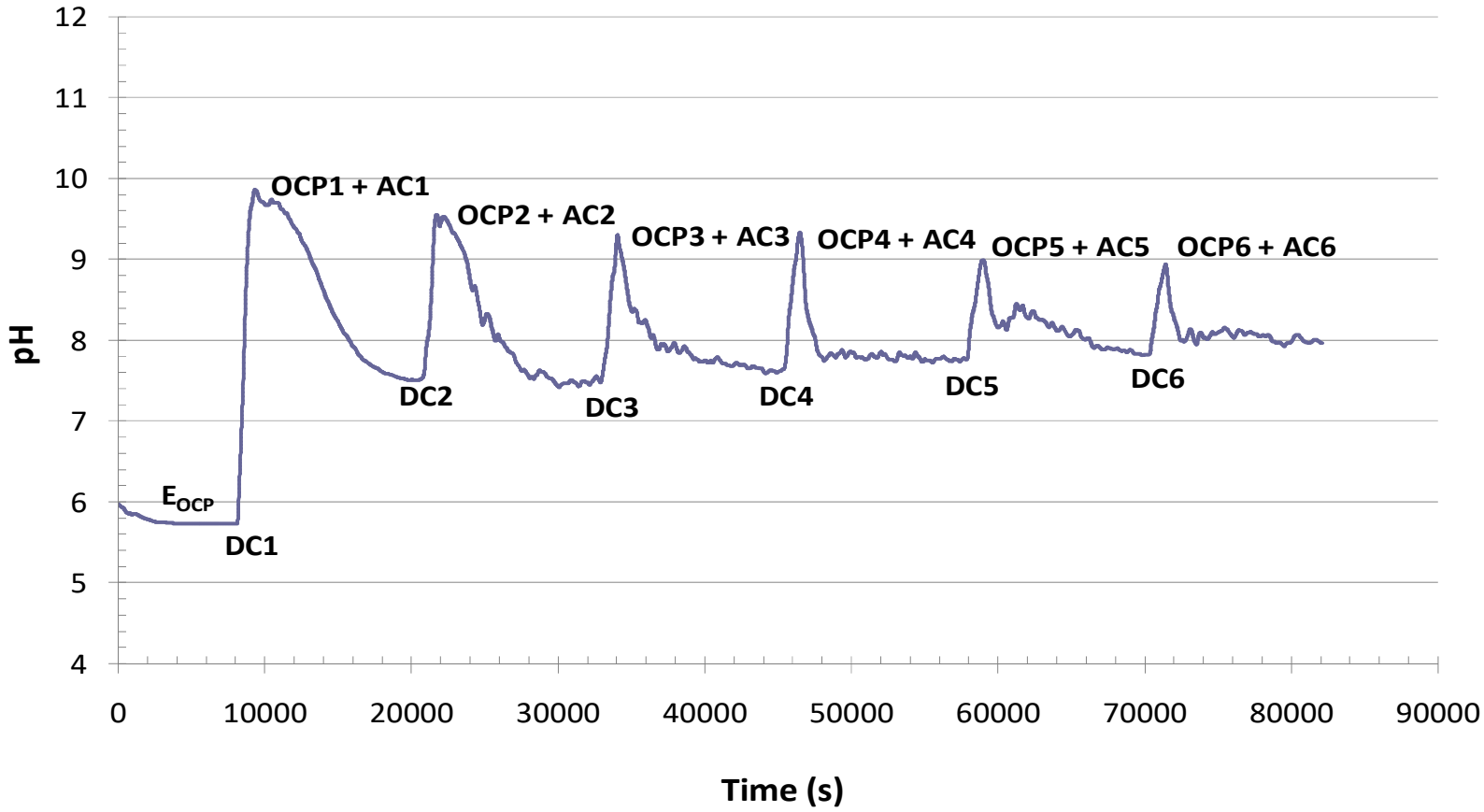

Figure 5.27: Evolution of the solution pH during six DC/OCP cycles for Al-13Cr-11N

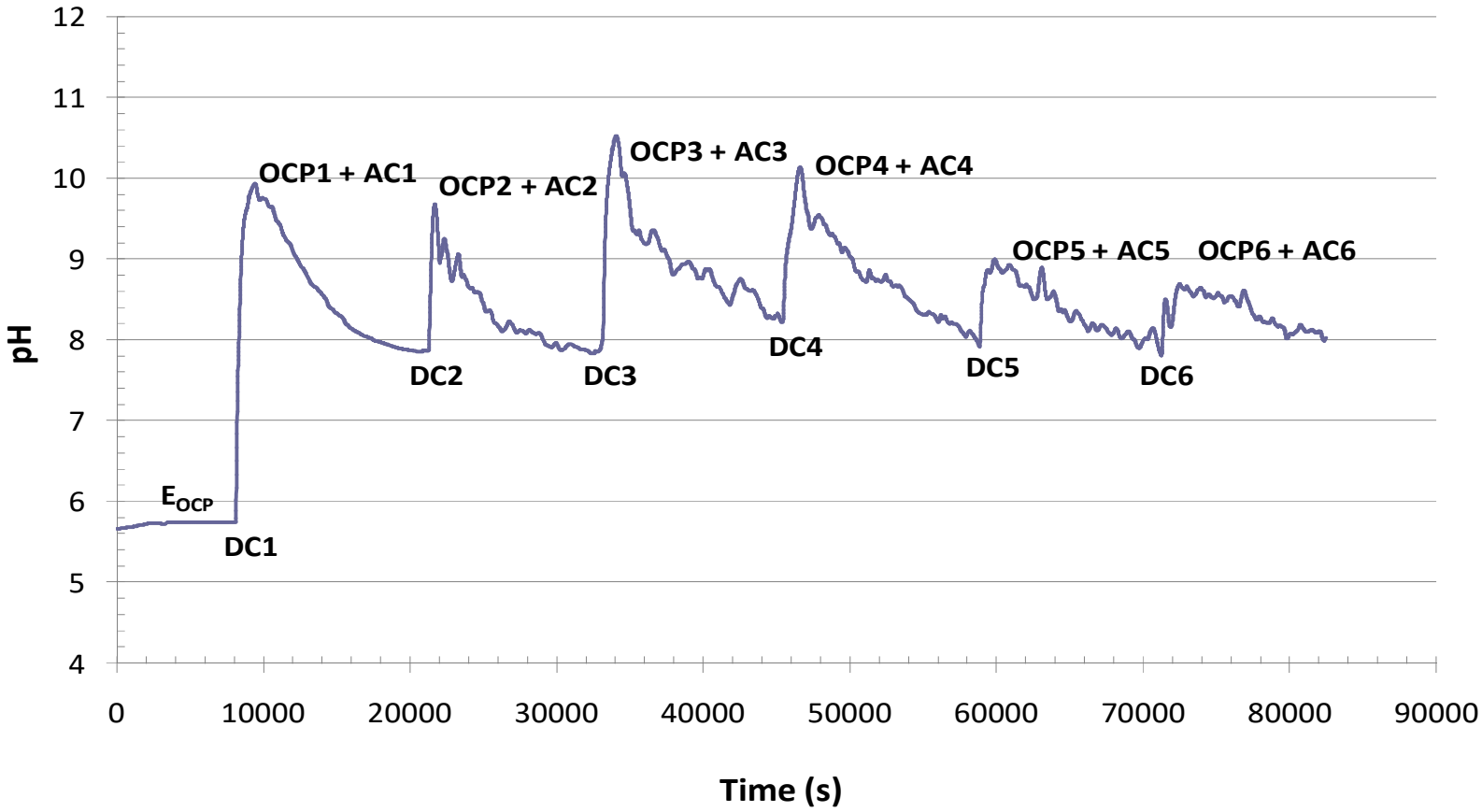

Figure 5.28: Evolution of the solution pH during six DC/OCP cycles for Al-16Cr-18N

for OCP3-OCP6 – which can be attributed to pitting corrosion of the passive film, leading to acidification of the electrolyte. For Al-4Cr-12N, the highest pH values were recorded during the first DC/OCP cycle, progressively decreasing with increasing number of cycles - which suggests a reduction in the rate of coating dissolution with each cycle due to the formation of a stable passive film.

For Al-13Cr-11N, the initial solution pH is measured to be 6.0 at the start of E_{OCP} decreasing to around 5.7 where it remains until DC cathodic polarisation is initiated. The pH trend in DC1 appears to be very similar to that observed for Al-4Cr-12N, displaying a noticeable increase in the alkalinity of the solution due to hydrogen ion (H^+) decay from the reduction of H^+ ions to form H_{ads} at the coating surface. The relaxation step (OCP1), which begins once DC cathodic polarisation is terminated, is characterised by a marked decrease in solution pH, with values approaching neutral (pH = 7.5) towards the end of this stage. During subsequent cathodic polarisation steps, the solution pH increases to around 9.3 for DC2 – DC4, with recorded values of just below 9 for DC5 and DC6. The profile of the pH curve appears to change during each relaxation step. While for OCP1 and OCP2 a gradual decrease in pH is observed throughout the three-hour period, for OCP3-OCP6, a sharp decrease in solution alkalinity is noted soon after the end of the DC step with the pH subsequently becoming fairly stable until the end of the relaxation stage. This significant decrease in solution pH indicates a reduction in the dissolution rate of the coating, probably because a large proportion of it was already removed during previous DC cycles. Noticeable fluctuations in pH are also observed during OCP2 – OCP6, which suggests that pitting corrosion of the coating is taking place.

For Al-16Cr-18N, the solution pH remains stable throughout E_{OCP}, with values close to 5.8 recorded at the end of this stage. As observed for the other two AlCr(N) coatings, DC1 brings a significant increase in solution pH, with the pH approaching 10 just before the applied

potential of -1.5V is removed. As mentioned above, this substantial increase is due to hydrogen ion decay in the electrolyte, caused by the reduction of H^+ ions into H_{ads}, which either migrate into the coating (becoming H_{abs}) or form H_2 gas which subsequently evolved out of the solution. OCP1 is characterised by a steady decrease in solution pH, down to around 8 before the start of DC2. The solution alkalinity appears to increase further during DC3 and DC4 which suggests an increase in the rate of coating dissolution as a result of hydroxide ion (OH^-) attack of the passive film and coating. However, for DC5 and DC6 only a small increase in solution pH is observed, probably due to the fact that most of the coating has been removed during the previous cycles. Significant fluctuations in pH were recorded during OCP2 – OCP6, possibly as a result of pitting corrosion of the coating.

The evolution of solution pH is examined in more detail in the following sections by looking at how the alkalinity of the solution changes during each individual DC and OCP step.

5.6.4.1 Evolution of the solution pH during DC cathodic polarisation

The solution pH was monitored throughout each DC cathodic polarisation step for Al-4Cr-12N, Al-13Cr-11N and Al-16Cr-18N, as illustrated in Figure 5.29. From the results it is clear that the evolution of the solution pH occurs in three main stages. The first stage (I) is characterised by very small or negligible changes in solution pH, followed by more rapid changes in stage II when a fast increase in the alkalinity of the solution is observed before reaching a steady state in stage III.

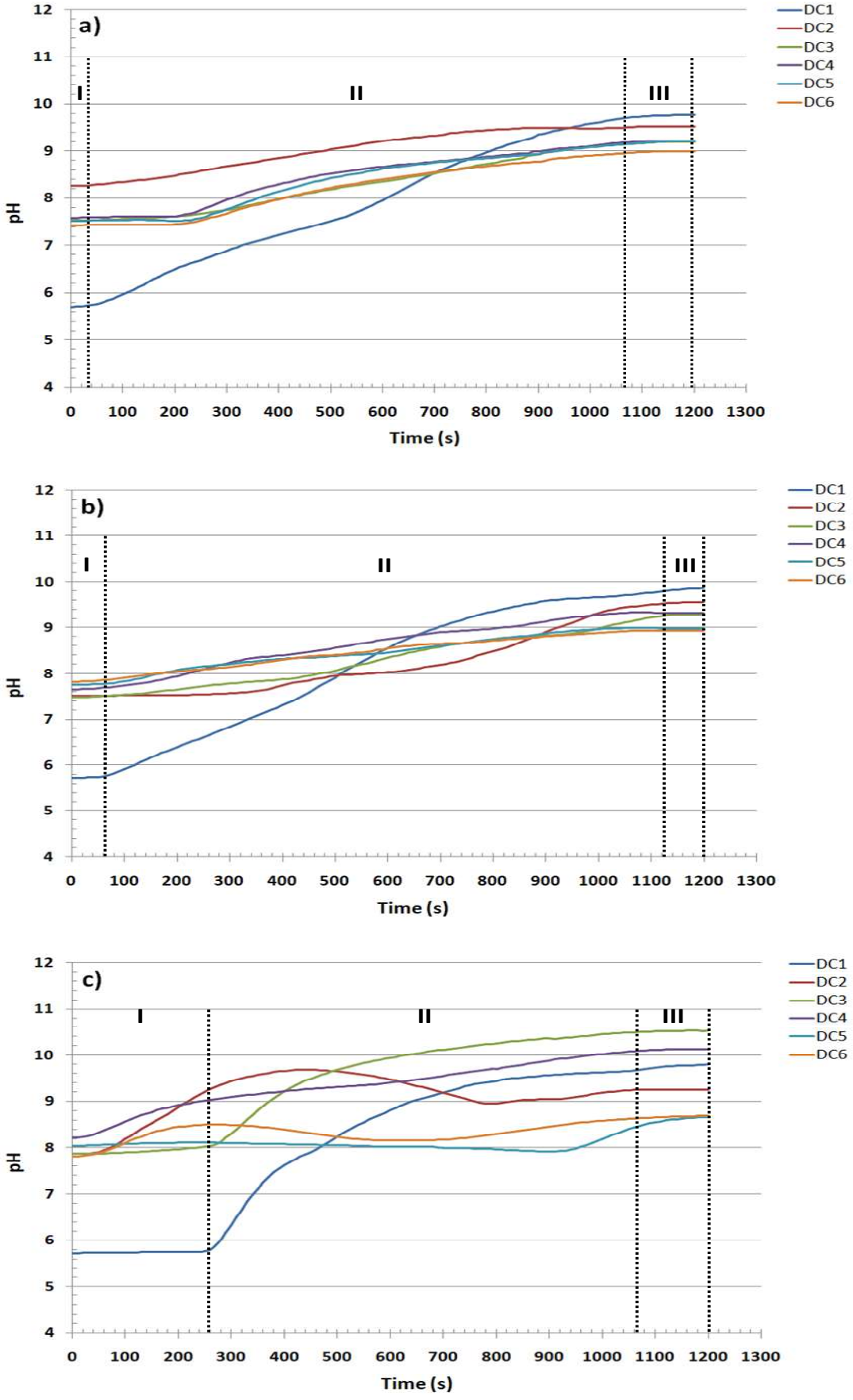

Figure 5.29: Evolution of the solution pH during each DC cathodic polarisation step for a) Al-4Cr-12N, b) Al-13Cr-11N and c) Al-16Cr-18N

For Al-4Cr-12N, the solution pH during DC1 appears to exhibit a narrow zone of stability in stage I, with the pH remaining constant for about 40s before increasing. This region of stability, referred to by Indeir [6] as the time lag, is related to the rate of hydrogen permeation through the passive film. The shorter the time lag, the higher the hydrogen permeation rate through the passive film due to the high permeability of the film. This therefore means that the native oxide film formed at the surface of Al-4Cr-12N during E_{OCP} is porous, which enabled the fast absorption of hydrogen atoms, as described in Figure 3.11a. The EIS data presented in Figure 5.20 confirmed the porous nature of the passive film, which exhibits a low charge transfer resistance (R1) and capacitance (CPE1) at E_{OCP}. A significant increase in the alkalinity of the solution is observed in stage II, with pH values rising from around 5.8 to 9.8 by the end of this stage. This can be attributed to the dissolution not only of the porous native oxide film but also of the underlying porous coating by hydroxide ions (OH^-) attack leading to the formation of an aluminium hydroxide ($Al(OH)_3$) film at the coating/passive film interface and a gel-like layer of aluminate ions ($Al(OH)_4^-$) at the passive film/electrolyte interface. The solution pH reaches a steady state in stage III, caused by a slowdown in the dissolution rate of the coating as a result of the presence of this viscous, gel-like aluminate ion layer, which hinders further OH^- ion attack of the coating. For DC2, the duration of the time lag in stage I appears to be very similar to that observed for DC1, despite the formation of a dense passive film during OCP1 (as revealed by EIS analysis in Figure 5.20). In the case of DC2 however, the initial pH values are much higher (around 8.2 compared to 5.8 for DC1) indicating a reduction in the hydrogen ion concentration of the electrolyte. Therefore the short time lag observed for DC2 is associated with the decrease in hydrogen ion concentration as a result of an increase in the solution alkalinity. The solution pH gradually increases in stage II as OH^- ion attack causes dissolution of the passive film, generating aluminate ions. The pH subsequently stabilises in stage III as the aluminate-rich layer acts as

a barrier against further OH^- ion attack of the passive film. In the case of DC3-DC6, stage I is characterised by a more defined plateau region showing negligible changes in pH for about 200s - which is five times longer than the time lag recorded for DC1 and DC2. The longer time lag is due to two main reasons: i) an increase in the H^+ ion concentration of the electrolyte (and hence H_{ads}) as the initial pH values are closer to neutral compared to those measured in DC2 and ii) a decrease in the hydrogen permeation rate through the dense passive films formed. EIS analysis (Figure 5.20) indeed confirmed that these passive films which formed during subsequent relaxation periods (OCP2 – OCP5) are dense and thick. As mentioned above, the initial pH values for DC3-DC6 are much closer to neutral (pH: 7.4 - 7.6) compared to those recorded for DC2 (pH around 8.2) indicating a higher concentration of H_{ads} at the passive film/electrolyte interface in the former. However, the low permeability of the passive films means that H_{ads} would tend to combine at the surface forming hydrogen gas as described in Figure 3.11b. The solution pH progressively increases in stage II, due to the formation of aluminate ions as a result of passive film dissolution. Compared to DC1, the slope of the pH curves for DC2-6 is not as steep because probably in these cases only the oxide film is being dissolved. In stage III, the pH values reach a steady state as the presence of a gel layer of aluminate ions impedes the movement of OH^- ions through the passive film, preventing further attack and dissolution of the film.

The three main stages are also observed in the evolution of the solution pH during DC cathodic polarisation for Al-13Cr-11N (Figure 5.29b). A time lag of 60s was recorded in DC1 stage I, which is slightly longer than the 40s time lag observed for Al-4Cr-12N. As both coatings exhibit similar initial pH values (around 5.7), this small increase in the time lag is probably caused by the formation of a dense Cr-rich passive film on the coating surface during E_{OCP}. This improvement in coating structure as a result of increasing Cr content leads to a decrease in the rate of hydrogen permeation through the oxide film, as confirmed by the

EIS data presented in Figure 5.21 - which showed that the charge transfer resistance of both passive film and coating is high prior to the start of the AC/DC/AC cyclic test. Lasting just over 1000s, stage II sees a significant increase in the solution pH from 5.8 to around 9.8, which can be attributed to the dissolution of the native passive film and the underlying coating from OH^- ion attack, resulting in the formation of aluminium hydroxide covered by a top gel-like layer of aluminate ions. The driving force behind coating dissolution is the greater difference in potential between the coating material and the substrate - as revealed in Figure 5.14. The pH becomes stable in stage III as the gel-like layer of aluminate ions at the coating/electrolyte interface slows down the migration of OH^- ions into the coating, preventing further dissolution. For DC2-DC6, the solution pH is slightly alkaline at the start of stage I with pH values between 7.4 and 7.8 indicating a lower concentration of hydrogen ions in solution compared to DC1; a shorter time lag is therefore anticipated. The results however show a variation in the time lag which appears to last around 140s for DC2 and DC3 decreasing to 60s for DC4 – DC6. This indicates that, during the initial relaxation periods (OCP1 and OCP2), a dense passive film formed - probably consisting of Cr-rich (in areas where the substrate has become exposed during previous DC steps) and Al-rich (from the dissolution of the Al-13Cr-11N coating) oxide layers, leading to a reduction in the hydrogen permeability rate (hence the observed increase in the duration of the time lag). A shorter time lag was recorded during the remaining DC steps because once most of the coating has dissolved during the initial DC steps (particularly during DC1 and DC2), a thin, and more permeable passive film (mainly Cr_2O_3) is generated on the substrate surface. The profiles of the pH graphs look very similar during stage II for DC3 – DC6, only displaying a slight increase in pH which can be attributed to the dissolution of the thin passive film (as most of the coating has been removed), that subsequently reforms during each successive relaxation

step. The highest pH values were recorded at the end of DC1, progressively decreasing with increasing number of DC/OCP cycles.

For Al-16Cr-18N, the time lag during DC1 was the longest recorded (lasting 260s) which indicates a decrease in the hydrogen permeability rate as a result of the formation of a dense and thick passive film on the coating surface during the initial OCP. Stage II displays a noticeable increase in solution pH, occurring as OH^- ion attack causes the dissolution of both passive film and coating - and the subsequent formation of an aluminium hydroxide film (and an aluminate ion gel layer) at the solid/electrolyte interface. As mentioned before, aluminate ion enrichment of the surface hinders further coating dissolution which explains why the pH stabilises towards the end of the DC step. DC2 displays a much shorter time lag (due to a reduction in H^+ ions concentration of the electrolyte with increasing pH) followed by a rapid increase in the alkalinity of the solution as a result of rapid coating dissolution taking place. DC3 exhibits a time lag similar in duration to that of DC1 despite the higher initial pH values (around 7.8), which suggests the formation during OCP2 of a dense passive film with a low H^+ ion permeability. The substrate material was most likely exposed during DC2, therefore the passive film is probably a Cr-rich oxide at the substrate surface - as well as on the surface of any remaining coating (owing the high Cr content of the coating). Stage II is characterised by a significant increase in the solution pH, with pH values of around 10.6 recorded, which suggests that further coating dissolution has occurred. A similar trend is also observed during DC4; therefore the first four DC/OCP cycles involved the dissolution of the passive film and coating during each DC step, followed by the formation of a Cr-rich passive film in subsequent relaxation periods. However, for the remaining two cycles (DC5 and DC6) there was no obvious increase in the alkalinity of the solution, indicating that the majority of the coating has been removed during previous cycles - leaving only the dissolution of the thin passive films, generated during OCP4 and OCP5.

5.6.4.2 Evolution of the solution pH during the relaxation time (OCP1-OCP6)

The solution pH was also monitored throughout each relaxation period (OCP1-OCP6) following DC cathodic polarisation for Al-4Cr-12N, Al-13Cr-11N and Al-16Cr-18N, as illustrated in Figure 5.30. The evolution of solution pH during the 3-hour relaxation period can be divided into two main stages. The first stage (stage I) is characterised by a gradual decrease in the solution pH, followed in stage II by minimal changes in pH as a steady state is reached.

For Al-4Cr-12N, it is evident that the solution pH recorded during the initial stage of each relaxation step appears to decrease with increasing number of DC/OCP cycles. At the end of the cathodic polarisation step, removal of the imposed -1.5V potential causes agitation of the viscous aluminate-rich gel layer, exposing the underlying coating to further OH^- attack. Coating dissolution ensues, leading to the formation of aluminate ions - as described in more details in section 3.1.5.1. In the case of Al-4Cr-12N, the pH during OCP1 is initially very high (around 9.8), increasing slightly for about 1000s before gradually decreasing until the end of the relaxation period. The high pH values recorded at the start of OCP1 are due to the formation of aluminate ions as a result of coating dissolution during DC1. The negligible increase in pH subsequently observed indicates a slow-down in the rate of coating dissolution - due to the reduction in concentration of OH^- ions in solution, as a great proportion of them were consumed during DC1 (Figure 5.30a). The gradual decrease in pH occurs as a result of the cathodic reduction of water (equation 3.20) taking place simultaneously with anodic coating dissolution. The two stages can be clearly seen for OCP2-OCP6. Stage I is characterised by a gradual decrease in solution pH with noticeable fluctuations in pH values observed particularly during OCP4-OCP6. These fluctuations in pH are due to pitting corrosion of the passive film which is not completely removed during previous DC cycles (DC2-DC5). As described in section 3.1.5.2, pitting corrosion results in the formation of the

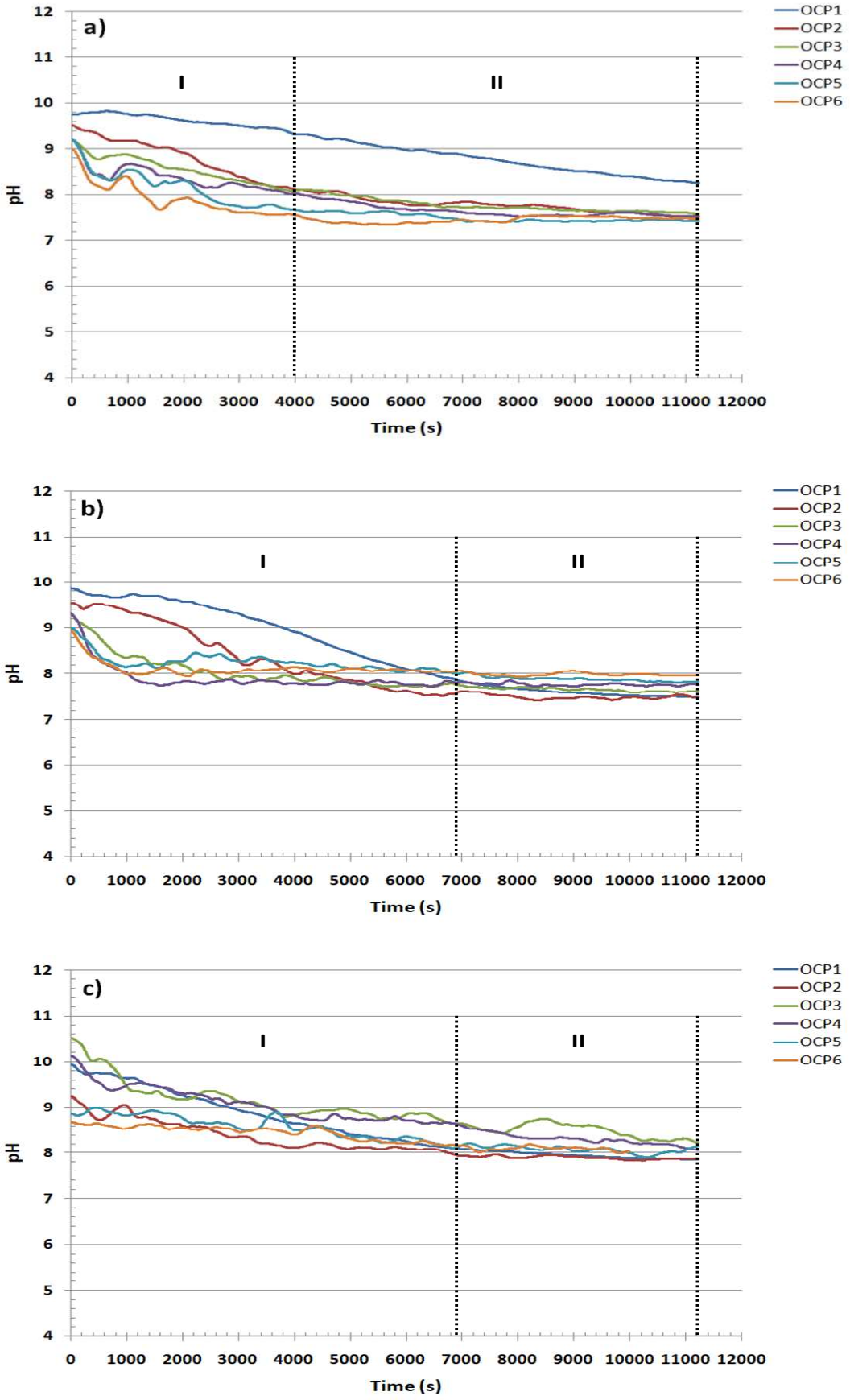

Figure 5.30: Evolution of the solution pH during each relaxation step for a) Al-4Cr-12N, b) Al-13Cr-11N and c) Al-16Cr-18N

complex $AlCl_4^-$ inside the pits - and acidification of the electrolyte, due to the generation of H^+ ions. The observed decrease in solution pH, which is also caused by the reduction reaction of water (generating H^+ ions), continues until a steady stage is reached (stage II).

For Al-13Cr-11N, a similar trend in the evolution of the solution pH during successive relaxation periods can be seen, generally involving a steady decrease in pH in stage I followed by negligible changes in the alkalinity of the electrolyte in stage II. For OCP1 and OCP2 the decrease in pH is however more gradual - probably as coating dissolution resulting in aluminate ion formation help maintain a higher pH value. For OCP3 – OCP6, the decrease in pH occurs more rapidly over a short duration as most of the coating was removed during previous cycles. Fluctuations in pH are also observed throughout stage I particularly during OCP3 – OCP6 due to pitting corrosion of the coating, which contributes to a further decrease in pH.

In the case of Al-16Cr-18N, the two stages are not completely distinct because minor variations in pH are seen for OCP1 – OCP6 throughout the three hours of relaxation, which is likely to be associated with pitting corrosion of any remaining coating. This causes acidification of the electrolyte as a result of increased H^+ ion concentration.

5.7 Summary

The mechanical, structural and corrosion properties of selected AlCr(N) coatings, containing varying amounts of chromium and nitrogen, were investigated in this Chapter. The main findings are summarised below:

- With the highest Cr and N content of all the AlCr(N) under investigation, Al-16Cr-18N exhibited the highest measured hardness and elastic modulus confirming that increasing the alloying element content results in a significant improvement in the

mechanical properties of Al-rich coatings. This is due to changes in the coating structure which becomes dense and compact as the proportion of alloying elements increases. Micro-abrasion wear data corroborate the results of the mechanical tests, revealing that the wear rate decreases with increasing alloying element content, with the lowest wear rate recorded for Al-16Cr-18N.

- The initial open circuit potential values show that the potentials of the three AlCr(N) coatings investigated are electronegative with respect to that of the 15/5 PH steel substrate, indicating that the coatings would provide sacrificial protection to the substrate. Despite having the lowest Cr content, Al-4Cr-12N is expected to dissolve more slowly and in a more controllable way to protect the substrate as its OCP is closest to that of the substrate.
- The EIS data measured after each DC/OCP cycle reveal that the three AlCr(N) coatings display different corrosion behaviours. Al-4Cr-12N exhibits a significant improvement in corrosion resistance properties as a result of forming, during successive relaxation periods, a dense and thick passive film which acts to protect the underlying coated system from corrosion. Moreover, the build-up of an Al-rich oxide within the coating pores reduces the coating porosity - thereby enhancing its barrier corrosion properties. It is clear that, with increasing Cr content, a highly stable passive film with enhanced corrosion resistance properties formed on the surfaces of both Al-13Cr-11N and Al-16Cr-18N. However, the results show that once the native passive film is removed during the initial stages of the AC/DC/AC cyclic test, a significant decrease in corrosion performance is observed due to the formation of a thinner, less corrosion-resistant film. Analysis of the corroded areas post-testing confirmed that for both coatings, extensive coating degradation has occurred, exposing the substrate material.

- The pH data provided detailed information regarding the nature of the passive films formed - and the rate at which the corrosion processes were taking place during the AC/DC/AC cyclic test. The results show that, for Al-4Cr-12N, coating dissolution is faster during the first cycle but slows down during the remaining cycles due to the gradual formation and build-up of a stable passive film. In contrast, for Al-13Cr-11N and Al-16Cr-18N, coating dissolution occurs during most of the DC/OCP cycles and the passive films formed during successive relaxation periods are thin (therefore quickly removed at the start of each DC step) and offer very little protection against corrosion of the underlying coating.
- From the results it is clear that the addition of both chromium and nitrogen has a significant effect on the properties of the coatings produced. While Al-4Cr-12N exhibits superior corrosion resistance properties in alkaline media, increasing the Cr and N content has the benefit of significantly enhancing the mechanical and tribological properties of the Al-rich coatings. These properties could be combined to produce graded coatings which satisfy the requirements for use as replacement to electroplated cadmium in many industries. In the aerospace sector for example, such coatings could be applied onto slat knuckle bearings found on the wings of aeroplanes and exposed to highly corrosive environments (e.g. alkaline aircraft de-icer fluid). In this case the coating may be designed to consist of:
    - A Cr adhesive layer in contact with the steel substrate
    - A middle AlCr(N) layer comprising a relatively high Cr and N content (e.g. Al-16Cr-18N) to provide good mechanical and tribological properties
    - A top Al-rich layer (e.g. Al-4Cr-12N) which offers not only excellent barrier corrosion protection by forming a highly stable passive film but also provides galvanic protection if placed in contact with other Al components.

Chapter 6

Conclusions and Recommendations for Future Work

6.1 Conclusions

The development and evaluation of aluminium-based PVD coatings as potential replacements for toxic cadmium were investigated in this study. After the initial coating deposition trials by electron-beam PVD, metallic Al-rich coatings were produced in an industrial-size magnetron sputter coating rig which provided a more controllable and repeatable process. The coatings were subsequently subjected to the improved AC/DC/AC cyclic corrosion test in order to assess their corrosion resistance properties in an alkaline environment. This accelerated laboratory test (which was conventionally used for evaluating the corrosion behaviour of organic coatings) was recently modified to include a pH monitoring system, so as to provide a more accurate assessment of the corrosion performance of electrically-conductive coatings. AlCr(N) coatings with varying chromium and nitrogen content deposited on stainless steel substrates were investigated in this study to determine their corrosion properties as well as their mechanical and structural characteristics. As the newly modified AC/DC/AC cyclic test was only recently used to successfully investigate different types of electrically–conductive metallic coatings, this work also provided the opportunity to evaluate the potential of this corrosion technique to discriminate between similar type of coatings but with slightly different compositions. The main findings of the research are summarised as follows:

- With increasing Cr and N content, the coating structure becomes denser and more compact resulting in significant improvements in the structural, mechanical (i.e. hardness in the range of 2 – 3.9 GPa and elastic modulus ranging from 89 to 114 GPa) and tribological properties of the Al-rich coatings
- The alloying element content also affects the nature of the passive film which forms on the coating surface. For Al-4Cr-12N with the lowest Cr content, the native passive film appears to be porous prior to the start of the test. However removal of this porous film during the first cycle enabled the formation and build-up in subsequent DC/OCP cycles of a thick and stable passive film (within the coating pores and at the surface) which acts as a barrier, protecting the underlying coated system from corrosion. The higher Cr content of Al-13Cr-11N and Al-16Cr-18N enabled in each case, the formation of a native passive film possessing good corrosion resistance properties. However once this passive film is removed, subsequent films which formed on the coating surface are thin and porous, offering very little protection to the coated system. The AlCr(N) coating with the lowest Cr content is the most corrosion-resistant of the three deposits under investigation.
- Monitoring the solution pH throughout the duration of the test provides useful information regarding the rate at which corrosion reactions were taking place which is hugely dependent on the characteristics of the passive film/coating system.
- The AC/DC/AC cyclic test was successfully used to discriminate between similar coatings with slightly different compositions.

These promising results could be used as a basis for further coating development to enable the deposition of multilayer graded AlCr(N) coatings with each individual layer tailored to meet specific properties depending on the intended application, thereby providing a range of coatings which could be successfully used to replace cadmium. To further enhance the

corrosion-resistance properties of the Al-rich coating, a post-coating treatment might be required to enable the formation on the outer coating layer of a thick and stable passive film in a controllable manner.

6.2 Further work

Six DC/OCP cycles were carried out in each case, bringing the total test duration per sample to just under 24 hours. The number of cycles was arbitrarily chosen; therefore, a review of the test results is required in order to determine whether or not this number of cycles is adequate for obtaining reliable information regarding the corrosion properties of a particular coating. It might be necessary to increase or decrease the number of cycles depending on the outcome of the review.

A wider range of AlCr(N) coatings with varying chromium content should be investigated so as to get a better understanding of the effect of both Cr and N on the nature of the passive film formed at the surface during testing - with the aim of finding the optimum coating which possesses good mechanical and structural characteristics as well as excellent corrosion resistance properties.

Further work is also required investigating the corrosion behaviour of AlCr(N) coatings if the protective film gets damaged, which may occur in service or as a coated part is being fitted prior to use (e.g. coated aerospace bearing fitted into a frame). This could be assessed by introducing some controlled damage (i.e. scribe marks) and repeating the cyclic test.

As the metallic AlCr(N) coatings were primarily developed as potential candidate to replace cadmium, it is essential that the corrosion performance of cadmium is evaluated using the

AC/DC/AC cyclic test so that the results can be directly compared to those of the Al-rich coatings.

The tribological properties of the AlCr(N) coatings could be further investigated by carrying out a wider range of wear testing (e.g. reciprocating sliding wear).

Further development work is clearly required in order to optimise each individual monolayer AlCr(N) coating and subsequently build, based on this work, graded multilayer coatings with optimum mechanical, tribological and corrosion properties which can be commercially used to replace cadmium in many applications. Although the initial results look promising, several stages of development work are still necessary in order to bring the Al-rich coatings to commercialisation as illustrated in Figure 6.1.

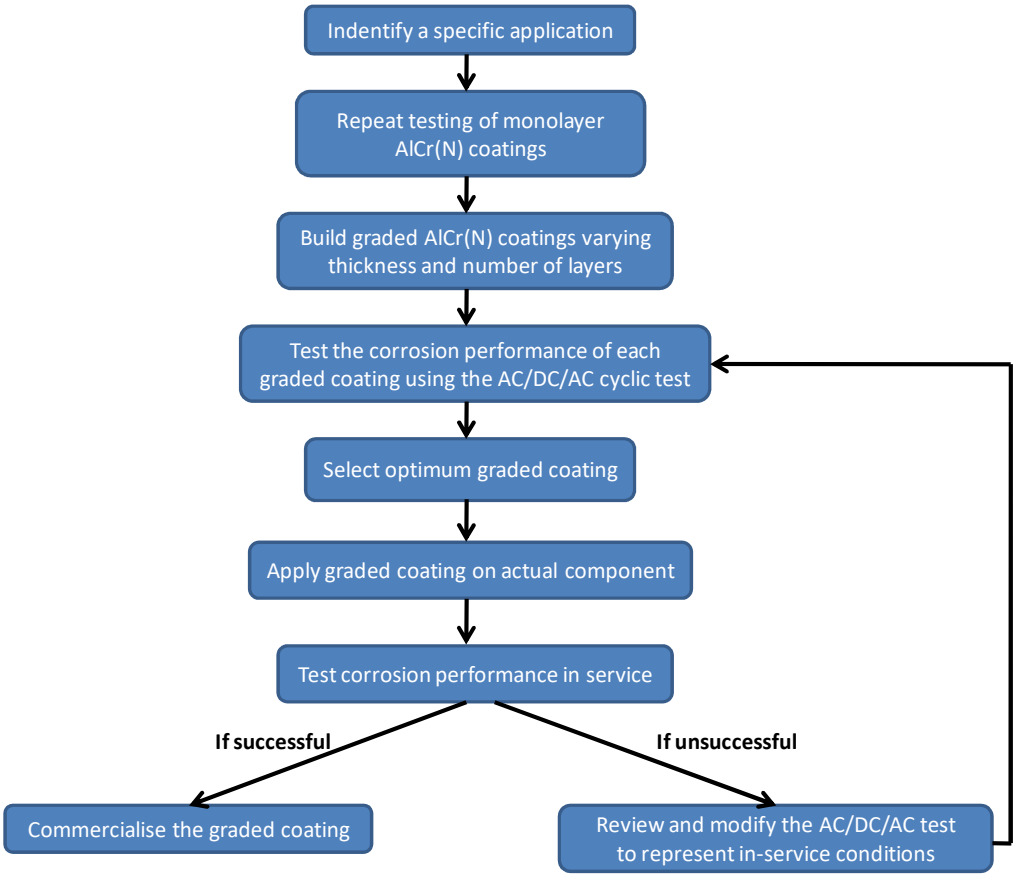

Figure 6.1: Flow chart outlining the stages of development work required to commercialise the AlCr(N) coatings

References

1. Groshart, E., *Finishing in the green.* Metal Finishing, 1997. **95**(4): p. 70-72.

2. ISSF, *The salt spray test and its use in ranking stainless steels in A technical guide to the salt spray test and its interpretation with stainless steel*. May 2008.

3. Macdonald, D.D., *Reflections on the history of electrochemical impedance spectroscopy.* Electrochimica Acta, 2006. **51**(8): p. 1376-1388.

4. Amirudin, A. and Thieny, D., *Application of electrochemical impedance spectroscopy to study the degradation of polymer-coated metals.* Progress in Organic Coatings, 1995. **26**(1): p. 1-28.

5. Kendig, M., Jeanjaquet, S., Brown, R. and Thomas, S., *Rapid electrochemical assessment of paint*. Journal of coatings technology, 1996. **68**(39): p. 840-863.

6. Indeir, F., *Development of an advanced DC-polarisation/AC-impedance cyclic test to evaluate the corrosion of electrically-conductive coating/substrate systems*, PhD Thesis, *Department of Materials Science and Engineering*. The University of Sheffield, March 2017. p. 241.

7. International Cadmium Association, *Available from: https://www.cadmium.org*, accessed June 2015.

8. Flott, L.W., *Quality control.* Metal Finishing, 1996. **94**(3): p. 55-58.

9. Dolati, A., Afshar, A. and Ghasemi, H., *A kinetic study on the electrodeposition of cadmium with the presence of organic agents in sulfate solutions.* Materials Chemistry and Physics, 2005. **94**(1): p. 23-28.

10. El-Halim, A.M.A. and Sobahi, M.I., *Effect of bath constituents and some plating variables on the electrodeposition of cadmium from acidic chloride baths.* Surface Technology, 1983. **19**(1): p. 45-57.

11. Abd El Halim, A.M., Abd El Wahaab, S.M., Abd El Rehim, S.S. and Abd El Meguid, E.A., *Electroplating of bright cadmium from an optimized acetate bath under the influence of superimposed alternating current.* Journal of Applied Electrochemistry, 1987. **17**(1): p. 49-56.

12. Morrow, H., *Cadmium electroplating.* Metal Finishing, 2007. **105**(10): p. 168-172.

13. Sankara Narayanan, T.S.N., *Influence of benzyl alcohols on the electrodeposition of cadmium.* Metal Finishing, 2001. **99**(9): p. 41-44.

14. British Standards, *Metallic and other inorganic coatings - electroplated coating of cadmium with supplementary treatments on iron or steel*. 2082:2008.

15. Mainier, F.B., Monteiro, L.P.C., Fernandes, L.H. and Oliveira, M.A.M., *Restriction on the use of cadmium coatings in industries*. 2013, ARPN journal of science and technology. p. 176-180.

16. Legg, K., *Cadmium replacement alternatives for the joint strike fighter*. December 2000, Rowan Technology Group, Libertyville, IL, USA, Report No. 3105JSF3.

17. Bielawski, M., *Development of unbalanced magnetron sputtered Al–Mo coatings for cadmium replacement.* Surface and Coatings Technology, 2004. **179**(1): p. 10-17.

18. Ganesan, P., Kumaraguru, S.P. and Popov, B.N., *Development of Zn–Ni–Cd coatings by pulse electrodeposition process.* Surface and Coatings Technology, 2006. **201**(6): p. 3658-3669.

19. Bernard, A., *Cadmium & its adverse effects on human health.* Indian J Med Res, 2008. **128**(4): p. 557-64.

20. MOD, *Cadmium coating elimination*. 2007, MOD Sustainable Development and Environment Manual, JSP 418, Volume 2, Leaflet 7-1.

21. Legg, K., *Overview of chromium and cadmium alternative technologies*. Surface Modifications Technologies XV, ASM International, Materials Park,2002.

22. Deeken, B. and Donaldson, K., *AlumiPlate®: An Alternative to Cadmium Plating for high strength steels in aircraft landing gear applications*. AeroMat 2005, Orlando, Florida, USA.

23. Holmes, V.L. and Jang, E., *The qualification of IVD Aluminium to replace cadmium at the Sacramento Air Logistics Center*. Aerospace Hazardous Materials Management Conference proceedings, 1995.

24. Holmes, V.L., *IVD aluminium coating and application of the process at Boeing - St. Louis*. Boeing A&M environmental technotes, August 2002.

25. Fennessey, H., *Technical alternatives to cadmium electroplating*. National Defense Center for Environmental Excellence, September 1994.

26. Jackson, R.P. and Pollard, T.C., *The evaluation of aluminium ion vapour deposition as a replacement for cadmium electroplating at U.S. army depots*. Anniston army depot, Report No.: REF-JTN-816005, CETHA-TS-CR-91054, April 1992.

27. Legg, K., *Evaluation of cadmium replacement alternatives for aircraft*. Rowan Technology Group, www.rowantechnology.com, 2002.

28. L-36, *Galvanic potential chart, available from: http://l-36.com/corrosion.php*, accessed December 2015.

29. Pushpavanam, M., Natarajan, S.R., Balakrishnan, K. and Sharma, L.R., *Corrosion behaviour of electrodeposited zinc-nickel alloys.* Journal of Applied Electrochemistry, 1991. **21**(7): p. 642-645.

30. Pagotto Jr, S.O., de Alvarenga Freire, C.M. and Ballester, M., *Zn–Ni alloy deposits obtained by continuous and pulsed electrodeposition processes.* Surface and Coatings Technology, 1999. **122**(1): p. 10-13.

31. Chouchane, S., Levesque, A., Douglade, J., Rehamnia, R. and Chopart, J. –P., *Microstructural analysis of low Ni content Zn alloy electrodeposited under applied magnetic field.* Surface and Coatings Technology, 2007. **201**(14): p. 6212-6216.

32. Maciej, A., Nawrat, G., Simka, W. and Piotrowski, J., *Formation of compositionally modulated Zn–Ni alloy coatings on steel.* Materials Chemistry and Physics, 2012. **132**(2–3): p. 1095-1102.

33. Sriraman, K.R., Brahimi, S., Szpunar, J.A., Osborne, J.H. and Yue, S., *Characterization of corrosion resistance of electrodeposited Zn–Ni Zn and Cd coatings.* Electrochimica Acta, 2013. **105**: p. 314-323.

34. Mosavat, S.H., Shariat, M.H. and Bahrololoom, M.E., *Study of corrosion performance of electrodeposited nanocrystalline Zn–Ni alloy coatings.* Corrosion Science, 2012. **59**: p. 81-87.

35. Mason, R., Neidbalson, M. and Klingenberg, M., *Update on alternatives for cadmium coatings on military electrical connectors.* Metal Finishing, 2010. **108**(3): p. 12-20.

36. Ganesan, P., Kumaraguru, S.P. and Popov, B.N., *Development of compositionally modulated multilayer Zn–Ni deposits as replacement for cadmium.* Surface and Coatings Technology, 2007. **201**(18): p. 7896-7904.

37. Rahsepar, M. and Bahrololoom, M.E., *Corrosion study of Ni/Zn compositionally modulated multilayer coatings using electrochemical impedance spectroscopy.* Corrosion Science, 2009. **51**(11): p. 2537-2543.

38. Yogesha, S. and Hegde, A., *Development of Composition Modulated Multilayer Alloy Coatings and their Corrosion Behavior*. Journal of metals, materials and minerals, 2011, **21**(1): p. 83-92.

39. NDCEE, *Alloy plating to replace cadmium on high strength steels, final report*. USA National Defence Center for Environmental Excellence, Task No. 000-02, Subtask 7, 2003.

40. Dubent, S., Mertens, M.L.A.D. and Saurat, M., *Electrodeposition, characterization and corrosion behaviour of tin–20 wt.% zinc coatings electroplated from a non-cyanide alkaline bath.* Materials Chemistry and Physics, 2010. **120**(2–3): p. 371-380.

41. Scully, J.C., *The fundamentals of corrosion*. Internationals series on materials science and technology, volume 17, 2nd edition, 1975.

42. Figueroa, D. and Robinson, M.J., *The effects of sacrificial coatings on hydrogen embrittlement and re-embrittlement of ultra high strength steels.* Corrosion Science, 2008. **50**(4): p. 1066-1079.

43. El hajjami, A., Gigandet, M.P., De Petris-Wery, M., Catonne, J.C., Duprat, J.J., Thiery, L., Raulin, F., Starck, B. and Remy, P., *Hydrogen permeation inhibition by zinc–nickel alloy plating on steel XC68.* Applied Surface Science, 2008. **255**(5, Part 1): p. 1654-1660.

44. Hillier, E.M.K. and Robinson, M.J., *Hydrogen embrittlement of high strength steel electroplated with zinc–cobalt alloys.* Corrosion Science, 2004. **46**(3): p. 715-727.

45. Devanathan, M.A.V. and Stachurski, Z., *The Adsorption and Diffusion of Electrolytic Hydrogen in Palladium.* Proceedings of the Royal Society of London. Series A. Mathematical and Physical Sciences, 1962. **270**(1340): p. 90.

46. Figueroa, D. and Robinson, M.J., *Hydrogen transport and embrittlement in 300 M and AerMet100 ultra high strength steels.* Corrosion Science, 2010. **52**(5): p. 1593-1602.

47. Akiyama, E., Wang, M., Li, S., Zhang, Z., Kimura, Y., Uno, N. and Tsuzaki, K., *Studies of Evaluation of Hydrogen Embrittlement Property of High-Strength Steels with Consideration of the Effect of Atmospheric Corrosion.* Metallurgical and Materials Transactions A, 2013. **44**(3): p. 1290-1300.

48. Hardie, D., Charles, E.A. and Lopez, A.H., *Hydrogen embrittlement of high strength pipeline steels.* Corrosion Science, 2006. **48**(12): p. 4378-4385.

49. Tsay, L.W., Lu, H.L. and Chen, C., *The effect of grain size and aging on hydrogen embrittlement of a maraging steel.* Corrosion Science, 2008. **50**(9): p. 2506-2511.

50. Mirkova, L., Maurin, G., Krastev, I. and Tsvetkova, C., *Hydrogen evolution and permeation into steel during zinc electroplating; effect of organic additives.* Journal of Applied Electrochemistry, 2001. **31**(6): p. 647-654.

51. Casanova, T., Soto, F., Eyraud, M. and Crousier, J., *Hydrogen absorption during zinc plating on steel.* Corrosion Science, 1997. **39**(3): p. 529-537.

52. Paatsch, W. and Hodoroaba, V.-D., *Coating technology of high strength steels without hydrogen embrittlement*. Federal Institute of Materials Research & Testing (BAM), Berlin, Germany, April 2002.

53. Harris, T.M., *Hydrogen diffusion and trapping in electrodeposited nickel*. PhD Thesis, Massachusetts Institute of Technology, 1989.

54. Tran, L.M., Schriever, M.P. and Jones, J.H., *Low hydrogen embrittlement zinc/nickel plating for high strength steels*. Patent, Publication No.: US 2008/0131721 A1, June 2008.

55. Gaydos, S., *Evaluation of Dipsol IZ-C17 LHE zinc-nickel plating*. HCAT/JCAT Meeting, Boeing St. Louis, available from: asetsdefence.org, January 2007.

56. Ross, A., Aylor, D. and Perez, A., *Cadmium replacement alternatives for corrosion and hydrogen embrittlement protection of high strength steels*. Department of Defense Corrosion Conference, http://db.materialoptions.com/asetsdefense/sedb, 2009.

57. Durairajan, A., Slavkov, D.S. and Popov, B.N., *Development of corrosion and hydrogen permeation resistant Zn-Ni-X (X = P, Cd) ternary alloy coatings*. Bulletin of the chemist and technologists of Macedonia, 2001, **20**: p. 3-17.

58. Kumaraguru, S.P., Veeraraghavan, B., Haran, B.S. and Popov, B.N., *Studies On Electrodeposited Zn-Ni-X (X = Cu, SiO_2) Ternary Alloys As a Replacement For Cadmium Coatings*. Conference paper, 202nd Meeting of the Electrochemical Society, October 2002.

59. Veeraraghavan, B., Kim, H., Haran, B. and Popov, B.N., *Comparison of Mechanical, Corrosion, and Hydrogen Permeation Properties of Electroless Ni-Zn-P Alloys with Electrolytic Zn-Ni and Cd Coatings.* Corrosion, NACE International, 2003. **59**(11): p. 1003-1011.

60. Valentini, R., Colombo, C., De Sanctis, M. and Lovicu, G., *Hydrogen re-embrittlement of aerospace grade high strength steels*. 2012, Frattura ed Integritan Strutturale. 2012, **21**: p. 30-36.

61. Vance, C.J. and Nguyen, T., *Electroplating aluminium alloys from organic solvents baths and articles coated therewith*. US patent, Publication No.: US 4721656 A, January 1988.

62. Beck, E. and Kovaleski, K., *Aluminium manganese molten salt plating*. Department of Defence (DoD), Final Report, ESTCP project WP 9903, June 2006.

63. Jankowski, E.J., *Aluminium-manganese plating from a molten salt bath*. Aircraft and Crew Systems Technology Directorate, Naval Air Development Center, Report No.: NADC-83127-60, August 1983.

64. O'Meara, M., Alemany, A., Maase, M., Vagt, U. and Malkowsky, I., *Deposition of aluminium using ionic liquids*. 2009. **107** (7-8): p. 38-39.

65. Caporali, S., Fossati, A., Lavacchi, A., Perissi, I., Tolstogouzov, A. and Bardi, U., *Aluminium electroplated from ionic liquids as protective coating against steel corrosion.* Corrosion Science, 2008. **50**(2): p. 534-539.

66. Bakkar, A. and Neubert, V., *Electrodeposition and corrosion characterisation of micro- and nano-crystalline aluminium from AlCl3/1-ethyl-3-methylimidazolium chloride ionic liquid.* Electrochimica Acta, 2013. **103**: p. 211-218.

67. Suneesh, P.V., Satheesh Babu, T.G. and Ramachandran, T., *Electrodeposition of aluminium and aluminium-copper alloys from a room temperature ionic liquid electrolyte containing aluminium chloride and triethylamine hydrochloride.* International Journal of Minerals, Metallurgy, and Materials, 2013. **20**(9): p. 909-916.

68. Barchi, L., Bardi, U., Caporali, S., Fantini, M., Alessandro Scrivani, Andrea Scrivani, *Electroplated bright aluminium coatings for anticorrosion and decorative purposes.* Progress in Organic Coatings, 2010. **68**(1–2): p. 120-125.

69. Agüero, A., del Hoyo, J.C., García de Blas, J., García, M., Gutiérrez, M., Madueño, L. and Ulargui, S., *Aluminum slurry coatings to replace cadmium for aeronautic applications.* Surface and Coatings Technology, 2012. **213**: p. 229-238.

70. Fasuba, O.A., Yerokhin, A., Matthews, A. and Leyland, A., *Corrosion behaviour and galvanic coupling with steel of Al-based coating alternatives to electroplated cadmium.* Materials Chemistry and Physics, 2013. **141**(1): p. 128-137.

71. Villafuerte, J. and Jodoin, B., *Recent trends in cold spray technology: potential applications for repair of military hardware*. Research and Technology Organisation, Report No.: RTO-MP-AVT-163, 2009.

72. Ghelichi, R. and Guagliano, M., *Coating by the Cold Spray Process: A State of the Art*. Frattura ed integrità strutturale, 2009, **8**: p. 30-44.

73. Berman, E.S. and Brooman, E.W., *Evaluation of APCVD aluminum coatings as an environmentally accepTable alternative to electroplated cadmium coatings.* Metal Finishing, 2009. **107**(2): p. 35-43.

74. Gu, S., Maeng, S., Suh, Y., Levy, R.A., Deavenport, D.L., Gomez, F.J., Newberg, S.S., Brooman, E.W., Berman, E.S., Kleek, J.J., Beatty, J.H., Schwartz, A.S. and Gaydos, S.P., *Investigation of Atmospheric Pressure CVD-Produced Aluminum Coatings for the Protection of Steel from Corrosion.* Chemical Vapor Deposition, 2010. **16**(7-9): p. 231-238.

75. Wass, L., *Summary of joint cadmium alternatives team efforts*. HCAT/JCAT conference, New Orleans, 23-25 January 2007.

76. Green, M.L., Levy, R., Nuzzo, R. and Coleman, E., *Aluminum films prepared by metal-organic low pressure chemical vapor deposition.* Thin Solid Films, 1984. **114**(4): p. 367-377.

77. Bowden, C. and Matthews, A., *A study of the corrosion properties of PVD Zn-Ni coatings.* Surface and Coatings Technology, 1995. **76**: p. 508-515.

78. Enders, B., Krauß, S. and Wolf, G.K., *Corrosion properties of aluminum based alloys deposited by ion beam assisted deposition.* Surface and Coatings Technology, 1994. **65**(1): p. 203-207.

79. Monaghan, D.P., Teer, D.G., Logan, P.A., Laing, K.C., Bates, R.I. and Arnell R.D., *An improved method for the deposition of corrosion-resistant aluminium coatings for aerospace applications.* Surface and Coatings Technology, 1993. **60**(1): p. 592-596.

80. Shedden, B.A., Samandi, M. and Window, B., *Stoichiometry of unbalanced magnetron sputtered Al–Mg alloy coatings.* Surface and Coatings Technology, 1997. **97**(1): p. 557-563.

81. Bates, R.I. and Arnell, R.D., *Microstructure of novel corrosion-resistant coatings for steel components by unbalanced magnetron sputtering.* Surface and Coatings Technology, 1997. **89**(3): p. 204-212.

82. Abu-Zeid, O.A. and Bates, R.I., *Friction and corrosion resistance of sputter deposited supersaturated metastable aluminium—molybdenum alloys.* Surface and Coatings Technology, 1996. **86**: p. 526-529.

83. Creus, J., Berziou, C., Cohendoz, S., Perez, A., Rébéré, C., Reffass, M., Touzain, S., Allely, C., Gachon, Y., Héau, C., Sanchette, F. and Billard, A., *Reactivity classification in saline solution of magnetron sputtered or EBPVD pure metallic, nitride and Al-based alloy coatings.* Corrosion Science, 2012. **57**: p. 162-173.

84. S. Touzain, Creus, J., Perez, A., Sanchette, F., Billard, A., *Corrosion Behavior of Al Based Multilayer Sacrificial Coatings*. Corrosion 2012, NACE international, NACE-2012-1568.

85. Perez, A., Sanchette, F., Billard, A., Rébéré, C., Berziou, C., Touzain, S., Creus, J., *Comparison of the intrinsic properties of EBPVD Al–Ti and Al–Mg coatings.* Materials Chemistry and Physics, 2012. **132**(1): p. 154-161.

86. Reffass, M., Berziou, C., Rébéré, C., Billard, A., Creus, J., *Corrosion behaviour of magnetron-sputtered Al_{1-x} –Mn_x coatings in neutral saline solution*. Corrosion Science, 2010. **52**: p. 3615-3623.

87. Senkov, O.N. and Miracle, D.B., *A topological model for metallic glass formation.* Journal of Non-Crystalline Solids, 2003. **317**(1): p. 34-39.

88. Inoue, A., *Bulk amorphous and nanocrystalline alloys with high functional properties.* Materials Science and Engineering: A, 2001. **304-306**: p. 1-10.

89. Leyland, A. and Matthews, A., *Design criteria for wear-resistant nanostructured and glassy-metal coatings.* Surface and Coatings Technology, 2004. **177-178**: p. 317-324.

90. Tsotsos, C., Kanakis, K., Davison, A., Baker, M., Matthews, A., Leyland, A., *Mechanical and tribological properties of CrTiCu(B,N) glassy-metal coatings deposited by reactive magnetron sputtering.* Surface and Coatings Technology, 2006. **200**(14): p. 4601-4611.

91. Sanchette, F., Tran Huu, L. and Frantz, C., *Deposition of metastable aluminium-chromium alloys by r.f. magnetron sputtering from mixed-powder targets.* Surface and Coatings Technology, 1993. **57**(2): p. 179-182.

92. Sanchette, F., Billard, A. and Frantz, C., *Mechanically reinforced and corrosion-resistant sputtered amorphous aluminium alloy coatings.* Surface and Coatings Technology, 1998. **98**(1): p. 1162-1168.

93. Sanchette, F. and Billard, A., *Main features of magnetron sputtered aluminium–transition metal alloy coatings.* Surface and Coatings Technology, 2001. **142**(Supplement C): p. 218-224.

94. Creus, J., Billard, A. and Sanchette, F., *Corrosion behaviour of amorphous Al–Cr and Al–Cr–(N) coatings deposited by dc magnetron sputtering on mild steel substrate.* Thin Solid Films, 2004. **466**(1): p. 1-9.

95. Sanchette, F., Ducros, C., Billard, A., Rébéré, C., Berziou, C., Reffass, M. and Creus, J., *Nanostructured aluminium based coatings deposited by electron-beam evaporative PVD.* Thin Solid Films, 2009. **518**(5): p. 1575-1580.

96. McCafferty, E., *Introduction to Corrosion Science*. 2010. Springer.

97. Di Benedetti, M., Loreto, G., Matta, F. and Nanni, A., *Acoustic Emission Monitoring of Reinforced Concrete under Accelerated Corrosion.* Journal of Materials in Civil Engineering, 2013. **25**(8): p. 1022-1029.

98. Akid, R., *Handbook of Advanced Materials: Enabling New Designs*. 2004. John Wiley & Sons, Inc.

99. Sato, N., *Green Corrosion Chemistry and Engineering: Opportunities and Challenges*. 2012: Wiley-VCH Verlag GmbH & Co. KGaA.

100. Huang, H., *The Eh-pH diagram and its Advances*. Metals, 2016. **6**(23): p. 1-30.

101. Ahmad, Z., *Principles of Corrosion Engineering and Corrosion Control*. 2006. Elsevier.

102. Ramirez, C. and Lei, K.S., *Evaluation of the Reliability and Corrosivity of VOC-free, No-clean Fluxes using Standard, Modified and Electrochemical Methods.* Soldering & Surface Mount Technology, 1996. **8**(1): p. 6-9.

103. Zhang, J., Klasky, M. and Letellier, B.C., *The aluminum chemistry and corrosion in alkaline solutions.* Journal of Nuclear Materials, 2009. **384**(2): p. 175-189.

104. Boukerche, I., Djerad, S., Benmansour, L., Tifouti, L. and Saleh, K., *Degradability of aluminum in acidic and alkaline solutions.* Corrosion Science, 2014. **78**: p. 343-352.

105. Su-Il, P. and Moon, S.-M., *Corrosion mechanism of pure aluminium in aqueous alkaline solution.* Journal of Solid State Electrochemistry, 2000. **4**(5): p. 267-272.

106. Moon, S.-M. and Su-Il, P., *Growth mechanism of anodic oxide films on pure aluminium in aqueous acidic and alkaline solutions.* Journal of Solid State Electrochemistry, 1998. **2**(3): p. 156-161.

107. Adhikari, S. and Hebert, K.R., *Factors controlling the time evolution of the corrosion potential of aluminum in alkaline solutions.* Corrosion Science, 2008. **50**(5): p. 1414-1421.

108. Natishana, P.M. and O'Gradyb, W.E., *Chloride Ion Interactions with Oxide-Covered Aluminum Leading to Pitting Corrosion: A Review*. Journal of The Electrochemical Society, 2014. **161**(9): p. C421-C432.

109. Mansouri, K., Ibrik, K., Bensalah, N. and Abdel-Wahab, A., *Anodic dissolution of pure aluminium during electrocoagulation process: influence of supporting electrolyte, initial pH and current density*. Industrial engineering chemical research, 2011. **50**: p.13362-13372.

110. Szklarska-Smialowska, Z., *Pitting corrosion of aluminum.* Corrosion Science, 1999. **41**(9): p. 1743-1767.

111. Kazempour-Liacy, H., Mehdizadeh, M., Akbari-Garakani, M. And Abouali, S., *Corrosion and fatigue failure analysis of a forced draft fan blade.* Engineering Failure Analysis, 2011. **18**(4): p. 1193-1202.

112. Srinivasa Rao, K. and Prasad Rao, K., *Pitting corrosion of heat-treaTable aluminium alloys and welds: a review*. Transactions of the Indian Institute of Metals, 2004. **57**(6): p593-610.

113. Baldwin, K.R. and Smith, C.J.E., *Accelerated corrosion tests for aerospace materials: current limitations and future trends.* Aircraft Engineering and Aerospace Technology, 1999. **71**(3): p. 239-244.

114. Singleton, R., *Accelerated Corrosion Testing.* Metal Finishing, 2012. **110**(9): p. 12-19.

115. ASTM, *B117-16: Standard Practice for Operating Salt Spray (Fog) Apparatus*. April 2016, ASTM International: West Conshohocken, USA.

116. Q-Lab. *Q-Fog Cyclic Corrosion Testers, www.q-lab.com*, accessed May 2017.

117. EGGA, *Salt spray testing - why it should not be used to compare different types of coatings*. June 2013, European General Galvanizers Associations (EGGA), https://www.egga.com/wp-content/uploads/2016/09/Salt-Spray-Testing-Information-Sheet.pdf, accessed on May 2017.

118. Simpson, C.H., Ray, C.J. and Skerry, B.S., *Accelerated Corrosion Testing of Industrial Maintenance Paints Using a Cyclic Corrosion Weathering Method*. May 1991: Journal of Protective Coatings and Linings. May 1991. p. 28-36.

119. Cesiulis, H., Tsyntsaru, N., Ramanavicius, A., Ragoisha, G., *The Study of Thin Films by Electrochemical Impedance Spectroscopy*, in *Nanostructures and Thin Films for Multifunctional Applications: Technology, Properties and Devices*, I. Tiginyanu, P. Topala, and V. Ursaki, Editors. 2016, Springer International Publishing: p. 3-42.

120. Loveday, D., Peterson, P. and Rodgers, B., *Evaluation of Organic Coatings with EIS. Part 1: Fundamentals of EIS*. Gamry Instruments, August 2004. p. 46-52.

121. Metrohm Autolab B.V., *Electrochemical Impedance Spectroscopy (EIS). Part 1 - Basic principles,* Autolab Application Note EIS01, AN-EIS-001, *https://www.metrohm.com/en-gb/applications*, accessed June 2017.

122. Metrohm Autolab B.V., *Electrochemical Impedance Spectroscopy (EIS). Part 3- Data Analysis,* Autolab Application Note EIS03, AN-EIS-003, *https://www.metrohm.com/en-gb/applications*, accessed June 2017.

123. Gamry, I., *EIS of Organic Coatings and Paints.* Available from: *https://www.gamry.com/application-notes/EIS/eis-of-organic-coatings-and-paints/*, accessed on June 2017.

124. Loveday, D., Peterson, P., and Rodgers, B., *Evaluation of Organic Coatings with EIS. Part 2: Application of EIS to Coatings*. Gamry Instruments, October 2004: p. 88-93.

125. Gamry, I., *Basics of Electrochemical Impedance Spectroscopy.* Available from:*https://www.gamry.com/application-notes/EIS/basics-of-electrochemical-impedance-spectroscopy/*, accessed June 2017.

126. Loveday, D., Peterson, P. and Rodgers, B., *Evaluation of Organic Coatings with EIS. Part 3: Protocols for Testing Coatings with EIS*. Gamry Instruments, February 2005. p. 22 - 27.

127. Gamry, I. *Rapid Electrochemical Assessment of Paint Rev. 1.0*. Application Note, Gamry Instruments, August 2014.

128. Ludwig, E., Hollaender, J. and Hillebrand, S., *Assessing protective layers on metal packaging material by electrochemical impedance spectroscopy*. 5th International Tinplate Conference Proceedings, 1992, London.

129. Hollaender, J., *Rapid assessment of food/package interactions by electrochemical impedance spectroscopy (EIS).* Food Additives & Contaminants, 1997. **14**(6-7): p. 617-626.

130. Rodríguez, M.T., Gracenea, J.J., Garcia, S.J., Saura, J.J. and Suay, J.J., *Testing the influence of the plasticizers addition on the anticorrosive properties of an epoxy primer by means of electrochemical techniques.* Progress in Organic Coatings, 2004. **50**(2): p. 123-131.

131. García, S.J. and Suay, J., *Anticorrosive properties of an epoxy-Meldrum acid cured system catalyzed by erbium III trifluromethanesulfonate.* Progress in Organic Coatings, 2006. **57**(4): p. 319-331.

132. Allahar, K.N., Bierwagen, G.P. and Gelling, V.J., *Understanding ac–dc–ac accelerated test results.* Corrosion Science, 2010. **52**(4): p. 1106-1114.

133. Yan, L., Ramamurthy, S., Noël, J. J., Shoesmith, D. W., *Hydrogen absorption into alpha titanium in acidic solutions.* Electrochimica Acta, 2006. **52**(3): p. 1169-1181.

134. Pérez-Ceballos, A.M., Calderón-Gutierrez, J.A. and Rosa-Mattos, O., *Effect of an electrolyte flow on electrochemical hydrogen permeation*. DYNA, 2014. **81**(187): p. 152-157.

135. Indeir, F., Yerokhin, A., Matthews, A. and Leyland, A., *A Comparative Study of the Corrosion Behaviour of PVD Al-based Coatings on Mild Steel by EIS and (AC)DC/AC Electrochemical Evaluation Techniques*. 2014, Society of Vacuum Coaters, 57th Annual Technical Conference Proceedings. http://dx.doi.org/10.14332/svc14.proc.1888.

136. Indeir, F., Matthews, A. and Leyland, A., *Development of (AC)DC/AC Cyclic Electrochemical Corrosion Evaluation Protocols for Accelerated Testing of PVD Metallic Coatings*. 2015: Society of Vacuum Coaters, 58th Annual Technical Conference Proceedings. http://dx.doi.org/10.14332/svc15.proc.1964.

137. San Marchi, C., *Technical reference on hydrogen compatibility of materials*. 2008, Sandia National Laboratories, http://www.ca.sandia.gov/matlsTechRef/, code 1810, accessed Nov 2014.

138. Reichelt, K. and Jiang, X., *The preparation of thin films by physical vapour deposition methods.* Thin Solid Films, 1990. **191**(1): p. 91-126.

139. Oerlikon Leybold Vacuum, *Turbovac T 1600, T 1601, TW 1600 - Turbomolecular pump with integrated frequency converter*. 2009: Incorporation declaration & operating instructions, 17200039_002_A1, 2009.

140. Mattox, D., *Handbook of physical vapour deposition (PVD) processing*. 2nd Edition, 1998. William Andrew, Elsevier.

141. Direct Vacuum, *Magnetron sputtering technology*. www.DirectVacuum.com, accessed August 2014.

142. Kelly, P.J. and Arnell, R.D., *Magnetron sputtering: a review of recent developments and applications.* Vacuum, 2000. **56**(3): p. 159-172.

143. Goodhew, P.J., Humphreys, J. and Beanland, R., *Electron microscopy and analysis, third edition*. 2000: CRC Press, ISBN: 9780748409686, 2000, chapter 5, 122-137.

144. *ZEISS EVO® MA 25* Scanning Electron Microscope, http://www.labwrench.com/?equipment.search/searchTerm/EVO%20MA25/, accessed February 2018.

145. Møller, P. and Nielsen, L.P., *Advanced surface technology, volumes 1 & 2*. Møller & Nielsen, ISBN: 9788792765239, 2013, chapter 35, 965-997, chapter 36, 1060-1061.

146. Speakman, S.A., *Basics of X-ray powder diffraction*. MIT Centre for Materials, Science and Engineering, http://prism.mit.edu/xray, XRD literature, accessed December 2014.

147. Blue Scientific, *Bruker D2 Phaser*. http://www.blue-scientific.com/nordic-products/bruker-xrd/bruker-d2-phaser/, accessed February 2018.

148. Westbrook, J.H., Conrad, H., *The science of hardness testing and its research applications*. American Society for Metals, 1973, p. 453-455.

149. Malzbender, J., den Toonder, J. M. J., Balkenende, A. R. and de With, G., *Measuring mechanical properties of coatings: a methodology applied to nano-particle-filled sol–gel coatings on glass.* Materials Science and Engineering: R: Reports, 2002. **36**(2): p. 47-103.

150. Ilze, M. and Janis, M., *Effect of substrate hardness and film structure on indentation depth criteria for film hardness testing.* Journal of Physics D: Applied Physics, 2008. **41**(7): p. 074010.

151. Franco Jr., A.R., Pintaúde, G., Sinatora, A., Pinedo, C.E. and Tschiptschin, A.P., *The use of a Vickers indenter in depth sensing indentation for measuring elastic modulus and Vickers hardness*. Materials Research, 2004, **7** (3): p. 483-491.

152. Tiwari, A., *Nanomechanical analysis of hybrid silicones and hybrid epoxy coatings – a brief review*. Advances in chemical engineering and science, 2012, 2, 34-44.

153. British Standard, *Metallic materials — Instrumented indentation test for hardness and materials parameters — Part 1: Test method*. British Standard, BS EN ISO 14577-1:2002.

154. Gee, M.G., Gant, A., Hutchings, I., Bethke, R., Schiffman, K., Van Acker, K., Poulat, S., Gachon, Y., von Stebut, J., *Progress towards standardisation of ball cratering.* Wear, 2003. **255**(1): p. 1-13.

155. Lakel, S., Almi, K. and Berriche, Y., *Micro-scale abrasive wear testing of Cr-Nx coatings*. Romanian Reports in Physics, 2007. **59**(1): p. 113-120.

156. Mercado-Solis, R.D., Mata-Maldonado, J.G., Quinones-Salinas, M.A., Rodriguez-de-Anda, E., Servin-Castaneda, R., *Micro-scale abrasive wear testing of CrN duplex PVD coating on pre-nitrided tool steel*. Materials Research, 2017. **20**(4): p. 1092-1102.

157. British Standard, *Fine ceramics (advanced ceramics, advanced technical ceramics) – Determination of the abrasion resistance of coatings by a micro-scale abrasion test*. BS ISO 26424:2008.*abrasion test*. British Standards, BS ISO 26424:2008.

158. ASTM, *Standard practice for exposure of metals and alloys by alternate immersion in neutral 3.5% sodium chloride solution*. ASTM International, ASTM G44 - 99(2013).

159. Sanchette, F., Tran Huu, L., Billard, A. and Frantz, C., *Structure—properties relationship of metastable Al-Cr and Al-Ti alloys deposited by r.f. magnetron sputtering: role of nitrogen.* Surface and Coatings Technology, 1995. **74-75**: p. 903-909.

160. Lawal, J., Kiryukhantsev-Korneev, P., Matthews, A. and Leyland, A., *Mechanical properties and abrasive wear behaviour of Al-based PVD amorphous/nanostructured coatings.* Surface and Coatings Technology, 2017. **310**: p. 59-69.

161. Walsh, F. C., Ponce de León, C., Kerr, C., Court, S. and Barker, B. D., *Electrochemical characterisation of the porosity and corrosion resistance of electrochemically deposited metal coatings.* Surface and Coatings Technology, 2008. **202**(21): p. 5092-5102.

162. Gudić, S., Smoljko, I. and Kliškić, M., *Electrochemical behaviour of aluminium alloys containing indium and tin in NaCl solution.* Materials Chemistry and Physics, 2010. **121**(3): p. 561-566.